# Switchable and Tunable Ferroelectric Devices for Adaptive and Reconfigurable RF Circuits

by

Victor Chia Lee

A dissertation submitted in partial fulfillment
of the requirements for the degree of
Doctor of Philosophy
(Electrical Engineering)
in the University of Michigan
2014

Doctoral Committee:

Professor Amir Mortazawi, Chair
Associate Professor Jerome P. Lynch
Professor Jamie D. Phillips
Professor Kamal Sarabandi

To my father, James Jenn-Huei Lee, mother Heidi Chen-Ton Chao Lee,
and sister, Grace Ruth Lee.

# ACKNOWLEDGEMENTS

I would like to take this opportunity to acknowledge and thank those that have made my Ph.D. studies and the work presented in this dissertation possible. First, I would like to thank my research advisor, Professor Amir Mortazawi, for his support, guidance, and encouragement as well as for teaching me how to be an independent researcher. Second, I would like to thank my dissertation committee members. In particular, I would like to thank Professor Phillips for sharing his expertise on material deposition and material characterization as well as for allowing me to use his research group's pulsed laser deposition (PLD) system to deposit barium strontium titanate (BST) thin films and metrology tools to measure the film thicknesses. In addition, I would like to thank Professor Kamal Sarabandi for his assistance and support with the MAST project and his interest in the success of my research. Furthermore, I would like to thank Professor Lynch for providing his perspective and insight on the work presented here.

I must also thank the former and current research group members of Professor Mortazawi. I especially want to thank Dr. Xinen (Alfred) Zhu, Dr. Jia-Shiang (Josh) Fu, Dr. Seyit Ahmet Sis, and Seungku Lee for their collaboration and discussion on BST thin film device research as well as co-authoring many conference and journal publications with me. I also want to thank Meng-Hung Chen, Dr. Morteza Nick, Dr. Danial Ehyaie, Dr. Waleed Alomar, Xiaoyu Wang, Elham Mohammadi, and Noyan Akbar for their help and support with classes and research. I would also like to thank my colleagues and fellow

graduate students in the Radiation Laboratory (RadLab), Lurie Nanofabrication Facility (LNF), (Jamie) Phillips Research Group (in particular, Adrian Bayraktaroglu), Electrical Engineering and Computer Science (EECS) Department, and Nanotechnology and Integrated Microsystems Student Association (NIMSA). This work would also not be possible without the RadLab staff, LNF staff (in particular, Dennis Schweiger), EECS staff, Army Research Laboratory (ARL) researchers, and University of California - Santa Barbara (UCSB) researchers. In addition, I need to thank my countless friends who have helped me through the good times and bad that have simply been invaluable to me.

Lastly and most importantly, I would like to thank my parents, my sister, and all of my relatives for their love and support during the many years I have been studying at the University of Michigan.

Victor Lee

January 2014

# TABLE OF CONTENTS

# LIST OF TABLES

# LIST OF FIGURES

# LIST OF APPENDICES

# ABSTRACT

As wireless communication systems have become more prevalent, their role has broadened from simply a means of connecting individuals to one another to a means of connecting individuals to the vast information and social network of the Internet. The resulting exponential increase in the utilization of wireless communication systems, the fundamental limitation of the finite wireless spectrum, and the use of conventional wireless communication systems that are designed to operate at fixed predetermined carrier frequencies pose a significant challenge. One method to address this problem is to use adaptive and reconfigurable wireless communication systems that can change their frequency and mode of operation based on the unused/available wireless spectrum in their environment as well as their surrounding environmental conditions. Unfortunately, currently available RF and microwave circuit components cannot meet the frequency agility specifications, performance requirements, and cost constraints necessary for the widespread commercialization of such systems.

This thesis explores how the multifunctional properties of ferroelectrics such as barium strontium titanate (BST) can be used to design switchable and tunable RF circuits for use in adaptive and reconfigurable wireless communication systems. In particular, the electric field dependent permittivity, electrostriction, and electric field induced piezoelectricity of BST are utilized for the design of electroacoustic resonators and filters. The main contribution of this thesis is the demonstration of several different intrinsically switchable,

tunable, and reconfigurable resonator and filter designs. First, BST film bulk acoustic wave resonators (FBARs), which exhibit electric resonances that are controlled by an applied dc bias voltage, are designed, fabricated, and characterized. In addition, reconfigurable dual-frequency resonators that utilize intrinsically switchable and tunable BST FBARs are demonstrated for the first time. Second, intrinsically switchable and tunable ferroelectric FBAR filters with insertion losses as low as 4.1 dB at 1.6 GHz are presented. Furthermore, dual-band BST FBAR filters that exhibit two different pass band responses in the low GHz range are demonstrated for the first time. Third, intrinsically switchable and tunable lateral (contour) mode resonators with frequencies as high as 1.67 GHz are demonstrated for the first time. Last of all, an RF magnetron sputtering system dedicated to BST thin film deposition is designed, assembled, and configured for continuing the improvements in ferroelectric thin film performance, developing novel ferroelectric based circuits, and designing larger and more complex circuits and systems.

# CHAPTER 1
# Introduction

## 1.1. Motivation

Wireless communication systems are constantly evolving to increase network capacity, achieve higher data bandwidth, extend communication range, improve quality of service, and/or lower costs. However, there are many challenges that need to be addressed before such improvements can be realized. First, newer systems must utilize the crowded wireless spectrum more efficiently [1]. This is because the number of wireless devices in use is growing at a phenomenal rate and the number of different communication standards in use by consumer electronics has been increasing [2, 3]. For example, a typical smartphone often contains RF frontends for Wi-Fi, Bluetooth, GPS, 2G, 3G, 4G, radio frequency identification (RFID), Global System for Mobile Communications (GSM), CDMA2000, etc. and future devices will include even more with the development of newer communication standards (e.g. WiMAX, 5G). Second, the complexity, power consumption, and size of the hardware must decrease while the reliability and lifetime need to increase [4]. These improvements are necessary for applications such as wireless sensor networks [5, 6] and wireless appliances where a large number of wireless devices are deployed and scattered throughout unknown, unsafe, or remote regions, making it cost inhibitive to rely on redundancy or replacement for maintaining operation. Therefore, the

transceiver must be able to adjust to constantly changing environmental conditions (e.g. temperature, moisture, noise floor, antenna loading effects, etc.) in order to maintain a communication link and sustain a long lifetime to maximum return on interest. Lastly, the system must provide a secure communication link to prevent wireless systems from being hacked and sensitive information from being intercepted. In order to address these issues, a new class of radio designs that are adaptive and reconfigurable is required.

The next generation of wireless communication systems is expected to be a form of cognitive radio with the ability to intelligently adapt and reconfigure themselves based on their circumstances. In other words, the transceivers must reconfigure themselves based on the user's demands and opportunistically exploit available communication channels in their environment while maintaining connectivity, quality of service, and a long battery life. This requires the ability to rapidly switch modulation scheme and carrier frequency to accommodate bandwidth requirements, minimize power consumption, and minimize propagation losses. These design requirements are very challenging and will become more so as the number of supported communication standards increases. An example of the complexity of an RF front end is illustrated in Figure. 1.1, which shows the block diagram of a global cellular phone and the many different RF components that are required just for the GSM bands [1]. There has been recent progress in achieving the next generation radio. For example, recently, the Intel Corporation announced the XMM™ 7160 [7], Broadcom Corporation their BCM21892 [8], and Qualcomm Incorporated their WTR1625L & RF360 [9], which are their respective 2G/3G/4G integrated modems for cellular phones. Integration and performance enhancements of integrated circuits (ICs) are steadily improving as a result of device scaling. However, passive radiating and frequency selective

components such as antennas and bandpass filters do not benefit from the rapid advances described by Moore's law for active devices and often contribute to a large portion of the transceiver's size and cost. In order to further reduce the complexity and cost of components such as resonators and filters, many new design approaches and materials are being explored. However, it is still unclear which of these technologies will be able to maintain high signal-to-noise (SNR) ratio, reject interference, and reduce power consumption for cognitive radios.

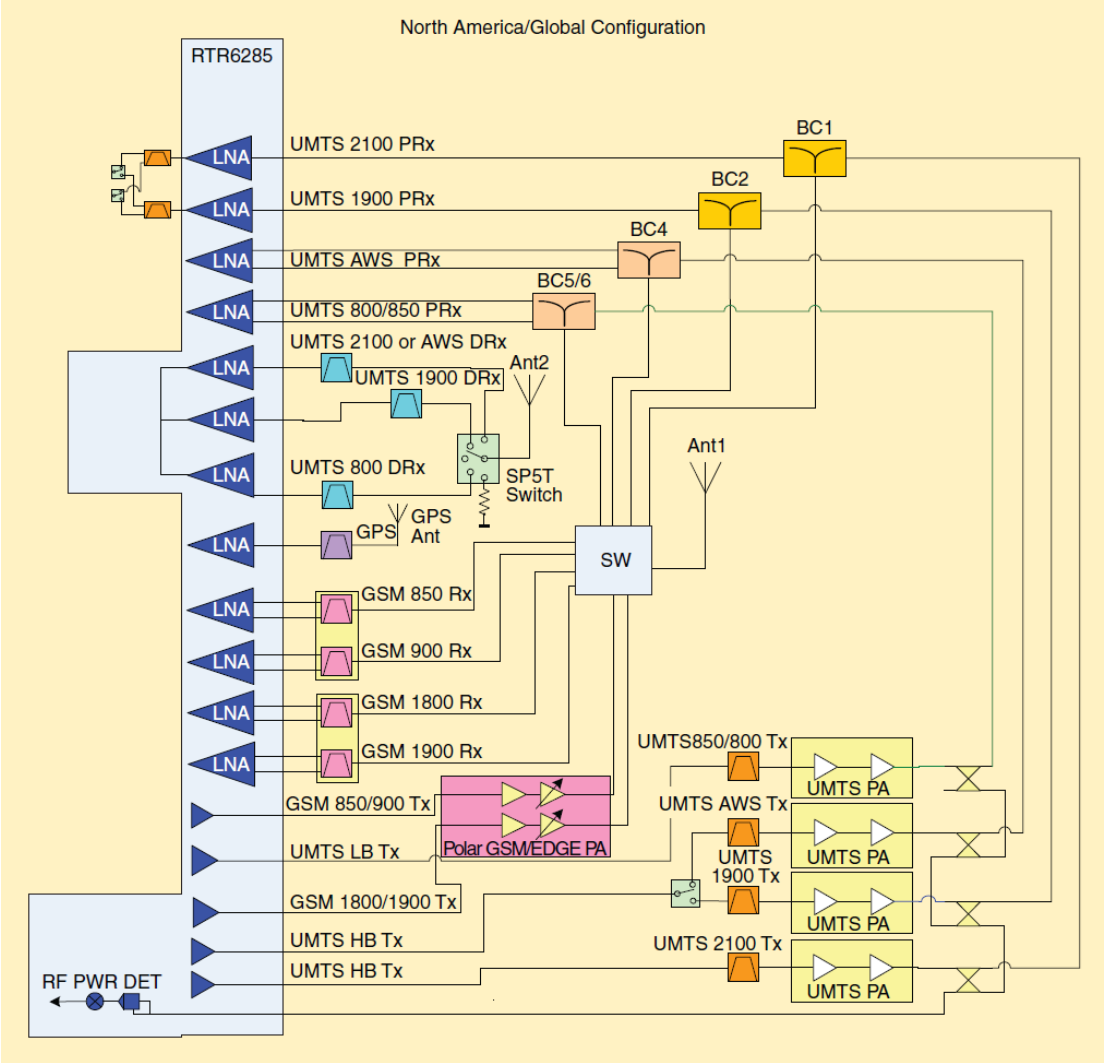

Figure 1.1: Block diagram of the RF frontend for a modern cellular phone. Reproduced from [1].

### 1.1.1. Overview of Resonator and Filter Technologies

There is substantial ongoing effort in improving almost every aspect of the many different components that make up an RF front end. Resonators and filters, which serve as the frequency determining components for RF front ends, have one of the most profound impact on the performance, size, and cost of wireless communication systems [3]. For example, very low loss resonators and filters can drastically reduce the power consumption while increasing sensitivity of the RF front end. Higher performance filters that are used in duplexers, triplexers, and multiplexers can also increase the data bandwidth and spectrum utilization achieved by the wireless communication system by reducing the minimum separation between communication bands. The use of frequency agile resonators and filters can drastically reduce the size, complexity, and cost of RF front ends.

Various techniques have been developed to realize frequency agile resonators and filters. However, mobile devices and sensors are severely size and weight constrained, limiting resonator and filters designs to electroacoustic and RF microelectromechanical system (MEMS) based technology. Fortunately, devices based on these two technologies are generally voltage-controlled, minimizing the required control components and adding to their robustness. Example of such devices include electrostatic resonators, which utilize a dc bias voltage to excite a capacitively transduced resonator. They possess excellent quality factors at ultra high frequency (UHF) [10-12]. However such resonators also have high motional impedances, which complicate their integration with standard 50 Ω systems. Another voltage controlled resonator design, which uses a MEMS switch in series with a traditional piezoelectric resonator, has also been demonstrated and have shown quality

factors of 2000 and turn-on voltages as low as 5 V [13-16]. However the signal loss and limited lifetime of the external switches are undesirable.

Many tunable and reconfigurable filters have also been demonstrated, such as in [11], where a two-filter self-switching electrostatic micromechanical filter bank with center frequencies of 9.40 and 9.55 MHz has been demonstrated. In [12], digitally-tunable mechanically-coupled MEMS filters that are able to selectively excite particular vibration modes are reported. In [16], SP2T lead zirconate titanate (PZT) MEMS switches are used to select between two mechanically coupled contour mode PZT-on-SOI filters with center frequencies of 197 and 294 MHz. Similar work is demonstrated in [13, 15, 17] using aluminum nitride (AlN). However, these approaches have not been able to simultaneously provide low insertion loss, high rejection, a 50 Ω port impedance, and very compact form factor.

The research presented in this thesis is intended to address the challenges of designing cognitive/intelligent radios using the ferroelectric thin film technology and in particular, the multifunctional properties of barium strontium titanate (BST, $Ba_{(x)}Sr_{(1-x)}TiO_3$) for resonator and filter design. Figure 1.2 shows the system diagram of what a reconfigurable RF front end that utilizes the multifunctional properties of ferroelectric thin film would look like. In the envisioned RF front end, the filter banks are implemented using intrinsically switchable ferroelectric FBAR filters that switch between different frequencies by simply controlling the applied dc voltage and without the need of solid state or MEMS based switches. The amplifiers are implemented using ferroelectric impedance tuner that consists of ferroelectric varactors/tunable capacitors so that a minimal number of amplifiers can be used over a wide frequency range. The local oscillator is implemented

with intrinsically switchable and tunable ferroelectric FBARs to minimize the required number of voltage controlled oscillators (VCOs).

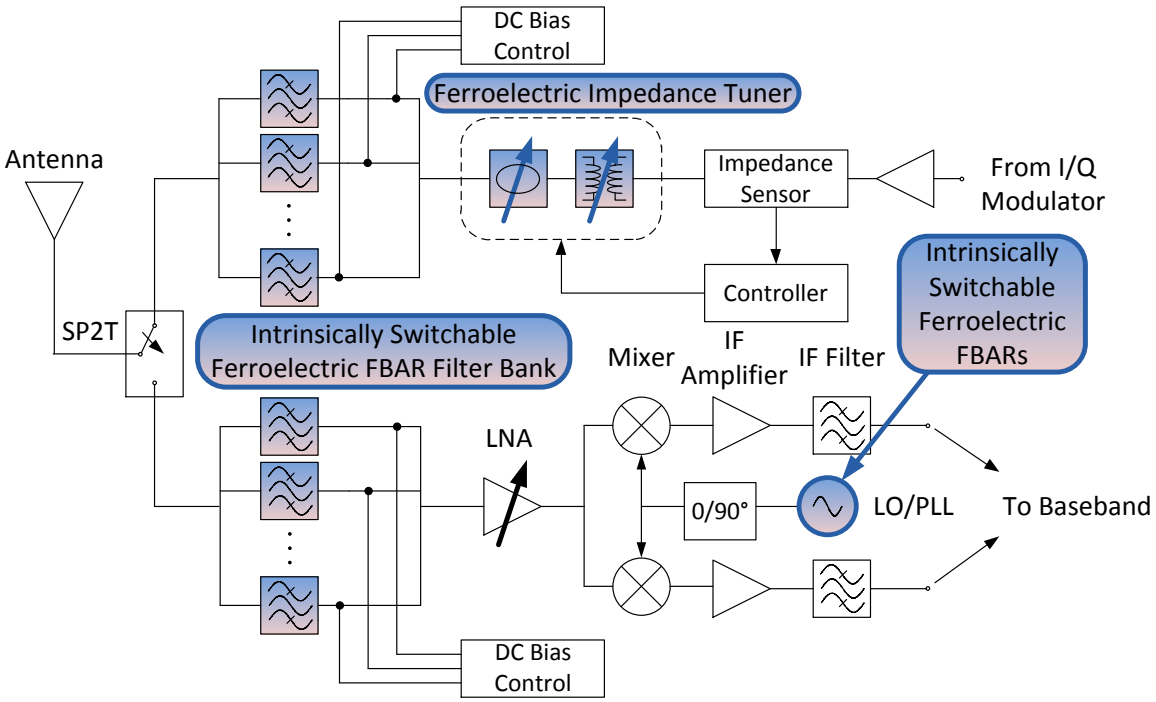


Figure 1.2: System diagram of a reconfigurable RF front end that utilizes the multifunctional properties of ferroelectric thin film technology.

## 1.1.2. Properties of Ferroelectric Thin Films

Ferroelectric materials are a class of ceramic dielectrics and a subgroup of piezoelectric and pyroelectric materials, as shown in Figure 1.3. Piezoelectrics and pyroelectrics exhibit electric field induced strain and temperature dependent spontaneous polarization [18]. These properties can be described by (1.1) and (1.2), which relate the temperature ($T$) dependent strain ($u$) of a material to the electrostriction coefficient ($Q$), spontaneous polarization ($P_s$), dielectric susceptibility ($\chi$), and electric field ($E$) [19-21]

$$u(T) = Q(T)P(T)^2 \tag{1.1}$$

$$P(T) = P_s(T) + \chi(T)E \tag{1.2}$$

$$u(T) = Q(T)P_s(\mathrm{T})^2 + Q(T)P_s(T)^2\chi(T)E + Q(T)\chi(T)^2E^2 \tag{1.3}$$

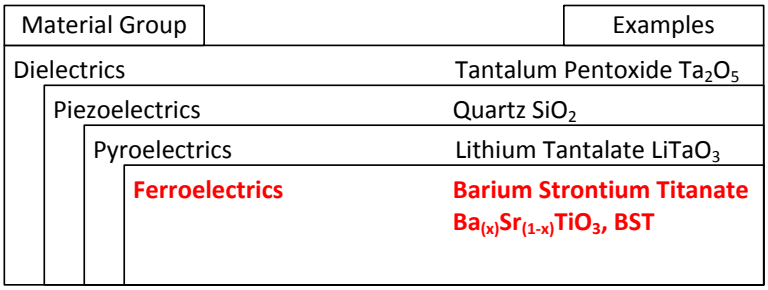


Figure 1.3: Illustration showing the relationship between different classes of dielectric materials [22].

In addition to these properties, ferroelectrics also exhibit a spontaneous polarization that can be reversed by an externally applied electric field. However, this only occurs when such materials are below their Curie temperature. When their temperature rises above the Curie temperature, they transition from the ferroelectric phase to the paraelectric phase and no longer exhibit spontaneous polarization [21]. For example, when the temperature of barium titanate rises above 116°C and its unit cell, shown in Figure 1.4, changes from a tetragonal to a cubic crystalline structure, the polarization-electric field curve does not display hysteresis. Strontium titanate (STO) is a material in the same class as barium titanate (BTO). However, for nearly all temperatures, it is in the paraelectric phase and therefore its polarization does not show hysteresis [21]. For ferroelectric solid solutions of barium strontium titanate ($Ba_{(x)}Sr_{(1-x)}TiO_3$, BST), the Curie temperature of the material depends on the ratio of barium to strontium, as shown in Figure 1.5. From this point on, BST based ferroelectrics will be the main focus since they are the family of ferroelectric that are used in the work presented here. The relative permittivity and electric polarization of BST thin films are shown in the top of Figure 1.6 as a function of temperature.

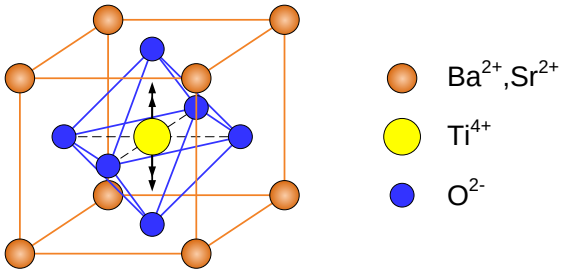


Figure 1.4: Unit cell of BST [18].

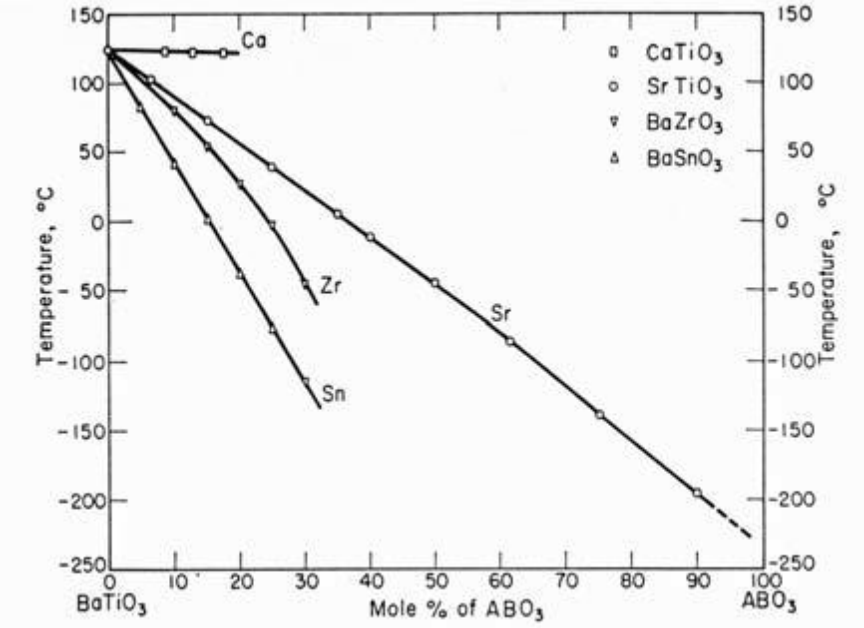


Figure 1.5: Dependence of Curie temperature of various ferroelectric as a function of chemical composition. (Reproduced from [18]).

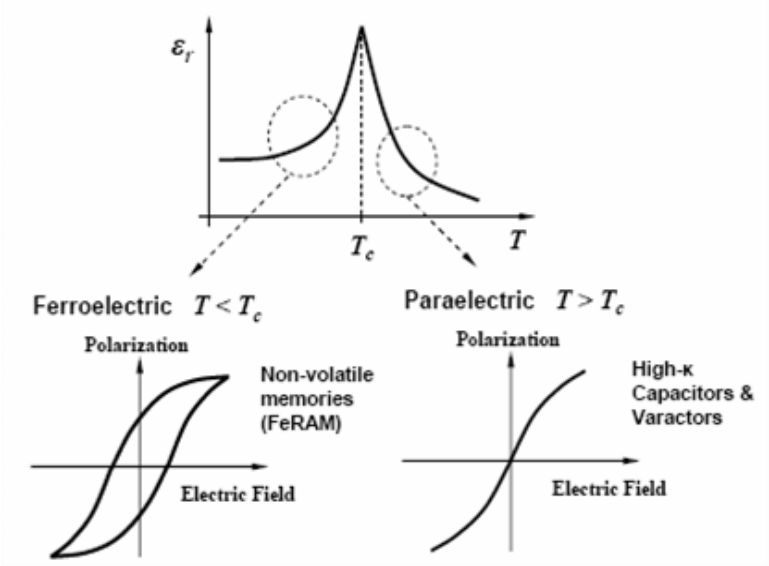

Figure 1.6: Diagram showing the relation temperature and permittivity of ferroelectric materials (Reproduced from [18]).

In thin film form, BST has properties that differ from that of its bulk form. Thin film BST in general has a much lower permittivity with a significantly decreased temperature dependence, making it quite ideal for use in commercial RF/microwave applications. BST thin films also require much lower control voltages for tuning the electric permittivity and reversing the spontaneous polarization since the required voltage is inversely proportional to the separation of the electrodes for metal-insulator-metal structures. BST thin films are commonly deposited using RF sputtering, pulsed laser deposition (PLD), metal-organic vapor phase epitaxy (MOCVD), sol-gel, and atomic layer deposition (ALD). Each of the deposition techniques have their own advantages and disadvantages such as initial capital cost, deposition rate, scalability, etc. and to a certain degree, can influence the characteristics of the material. One disadvantage of the thin film deposition process is the traditionally high temperature growth conditions necessary to obtain high quality film, which can limit the type of devices that can be integrated onto the substrate, substrate material, and the bottom electrode material. However, material deposition is still a very

active area of research due to the material's exceptionally valuable properties that can be used for a variety of applications, as discussed in the next section. Therefore, continued research and development in the deposition process as well as improvements in film quality can be expected.

### 1.1.3. Ferroelectric Devices

Many of the multifunctional properties of ferroelectric materials used for device design are presented by the Heckmann diagram shown in Figure 1.7, which shows the broader relationship between the thermal, mechanical, and electrical properties of these materials. Thermal-based detectors and sensor arrays for infrared (IR) imaging commonly employ pyroelectricity and measure the change in spontaneous polarization due to the increase in temperature from absorbed IR radiation [23]. Non-volatile memories can be realized by using ferroelectricity (electric field reversible spontaneous polarization) to create ferroelectric random access memory (FeRAM), which use ferroelectric capacitors or ferroelectric field effect transistors (FeFETs) [23]. Similarly, ferroresistivity can be employed to create ferroresistive random access memory (FRRAM) and ferroelectric tunnel junctions (FTJ) [23]. Sensors, transducers, and actuators can also be designed using piezoelectricity through a variety of methods [21, 23, 24]. Compact and light weight super capacitors, as well as high density dynamic random access memory (DRAM) can be realized by the very high permittivity of ferroelectrics. Last but not least, RF and microwave circuits that utilize the various properties of ferroelectrics, especially BST, can be designed.

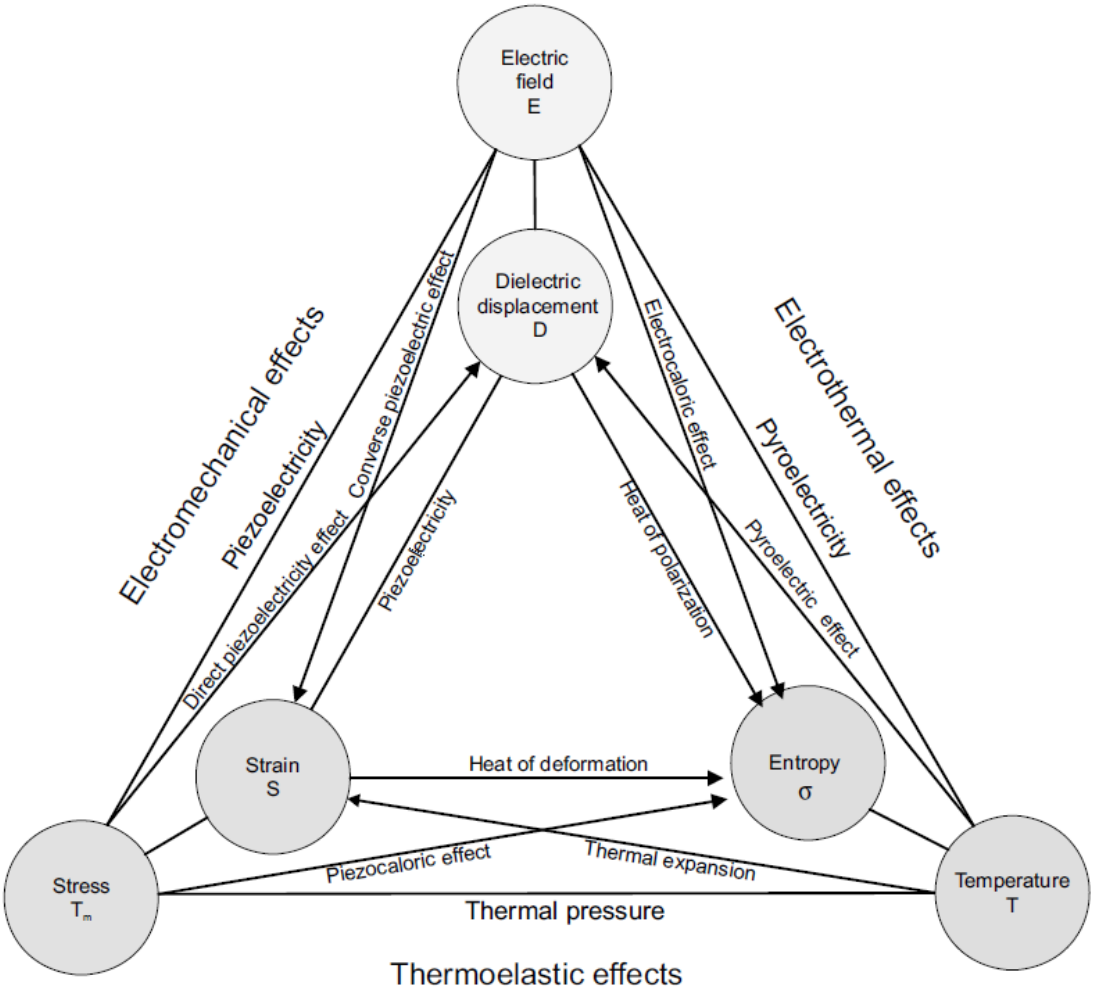


Figure 1.7: The Heckmann diagram, which shows the thermal, mechanical, and electrical relationships of a material (Reproduced from [22]).

The dielectric properties of ferroelectrics have a variety of uses for RF and microwave applications. In their bulk form, their high electric permittivity has been used in dielectric resonators and filters, lens antennas, and dielectric substrates [21, 23]. In their thin film form, the electric field dependent permittivity and low loss tangent of thin film ferroelectrics make them ideal materials for voltage tunable capacitors (varactors) [18]. In the absence of an external electric field, the capacitance of BST varactors are at their maximum. With the introduction of an electric field from the application of a dc bias voltage, their permittivity decreases through the relation given in (1.4), where $C_{max}$ is the

maximum capacitance of the capacitor, which typically occurs at 0 V bias and $V_2$ is the value of the voltage (V) at which the value of the capacitor is half of $C_{max}$. An example of a tuning curve of a BST capacitor is shown in Figure 1.8.

$$C(V) = \frac{C_{\max}}{2\cosh\left(\frac{2}{3}\sinh^{-1}\left(\frac{2V}{V_2}\right)\right) - 1} \tag{1.4}$$

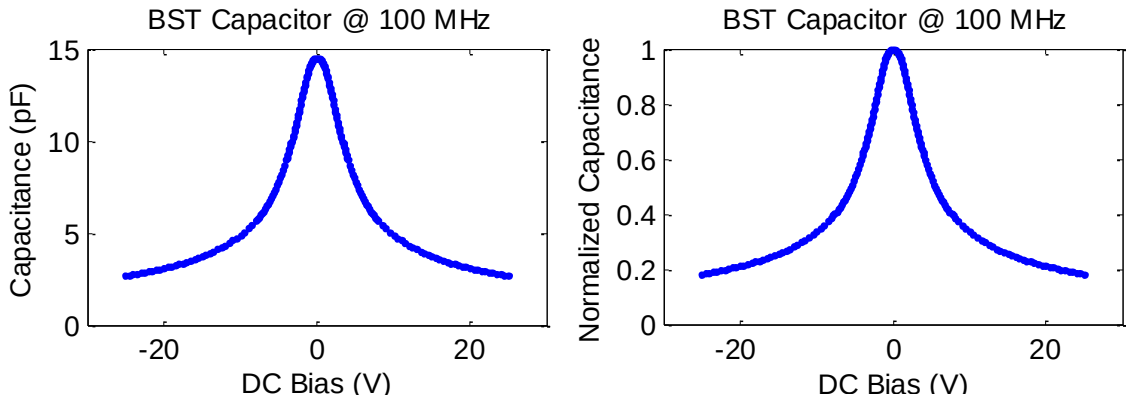


Figure 1.8: Tuning curve and normalized tuning curve of a BST MIM capacitor measured at 100 MHz. The dc bias is swept from -25 to 25 V.

Compared to semiconductor diode varactors, BST varactors have a higher RF power handling capacity and do not have a conducting state. Furthermore, compared to MEMS based varactors, BST varactors are smaller, have a faster response time, do not suffer from mechanical fatigue, and have excellent power handling capabilities. Other advantageous properties are listed below:

1) Good long-term stability at operational temperatures and voltages

2) Low loss tangent/high quality factors

3) Negligible dispersion in high quality films

4) Completely passive and do not suffer from junction noise (unlike Schottky and varactor diodes)

5) No quiescent current and therefore no static power consumption and

6) Small footprint.

BST thin film based varactors have been employed in phase shifters, tunable filters, voltage controlled oscillators, frequency modulators, parametric amplifiers, tunable power divider, and many other applications [18, 21, 23].

While the dielectric properties of BST have been well characterized and utilized for RF and microwave applications, it is only recently that the electrostriction and electric field induced piezoelectricity of BST thin films have been utilized for the design of electromechanical resonator [19, 25]. Without any applied dc bias, the BST thin film metal-ferroelectric-meta (MFM) devices behave as simple capacitors. However, with the application of a dc bias, which creates a large electric field within the BST thin film, acoustic waves can be excited within the materials and for a properly designed resonator, a series and parallel resonance are observed. The voltage/electric field dependent properties of BST resonators can be used for the design of intrinsically tunable and switchable oscillator and filter designs. The ability of BST thin films to be used for varactors as well as tunable and switchable resonators and filters provides the opportunity to create an entirely adaptive and reconfigurable RF front end, such as the one shown in Figure 1.1, using BST thin film technology. The focus of this thesis is to utilize BST thin film technology to design RF and microwave electroacoustic frequency selective devices.

This concludes the discussion on the motivation behind realizing adaptive and reconfigurable wireless communication system and how ferroelectric thin film technology

can play a critical role in addressing the multiple challenges that engineers face in attaining cognitive radios. The background on adaptive resonators and filters, ferroelectric thin film technology, and ferroelectric BST thin film devices provided in this chapter serves as the foundation and starting point for the topics that will be discussed in this thesis.

## 1.2. Thesis Organization

The remainder of this thesis is organized in the following manner:

Chapter 2 will focus on the design, performance, and modeling of BST based intrinsically switchable, tunable, and reconfigurable resonators. First, the acoustic wave transmission line model, which is a method for determining the behavior of acoustic waves in multilayered structures, will be utilized for designing BST-based bulk acoustic wave resonators. Then, the fabrication process of BST bulk acoustic wave resonators will be described. Subsequently, the dc voltage dependent, RF power dependent, and switching performance of BST FBARs as well as their reliability will be discussed. Furthermore, their dc voltage and RF power dependent frequency response will be modeled using the Modified Butterworth-Van Dyke (MBVD) model. Next, the design and performance of reconfigurable BST FBARs are presented. Intrinsically switchable BST FBARs of different resonance frequencies are electrically connected in series. Individual FBARs can be switched on independently by controlling the dc bias voltage across each device. This is the first demonstration of reconfigurable resonators that utilize BST thin film technology.

Chapter 3 will focus on the design and performance of electrically coupled BST FBAR filters and reconfigurable BST FBAR filters. Intrinsically switchable BST FBARs are arranged in a ladder configuration to create electrically coupled FBAR filters that show a

band pass response when the FBARs are switched on with the application of a dc bias. By using the MBVD and acoustic wave transmission line model to represent the resonators that make up the filter, the proper filter design can be obtained. Without dc bias, the filter is off and the device isolates the two ports. The design and performance of reconfigurable BST FBAR filters is also presented. Intrinsically switchable BST FBAR filters of different frequencies are connected in parallel with one another. Each filter consists of an electrically coupled 1.5 stage ladder filter placed in between series connected BST MFM varactors. This is the first demonstration of a reconfigurable filter that utilizes intrinsically switchable BST FBAR filters and BST varactors to switch on/off individual filter elements.

Chapter 4 will focus on the design, performance, and modeling of intrinsically switchable contour mode bulk acoustic wave resonators using the ferroelectric material barium titanate ($BaTiO_3$ or BTO). The non-zero effective $d_{31}$ exhibited by BTO and its electric field induced piezoelectricity is utilized to create intrinsically switchable resonators that have their resonance frequency mainly determined by their lateral dimensions. The design and measurement results of BTO ring-shaped contour mode resonators are discussed. In addition, the design, measurement, and modeling results of interdigitated contour mode resonators are presented. This is the first demonstration of intrinsically switchable ferroelectric contour mode resonator.

Chapter 5 will focus on the design, assembly, and operation of an RF magnetron sputtering system for BST thin film deposition. Each component of the system is described and its function relative to the overall system is discussed. The standard operating procedure for the system included and the optimal deposition conditions are also included.

Chapter 6 will summarize the topics that have been are discussed in each of the chapters, relate each research topic discussed in this thesis to the challenge of achieving adaptive and reconfigurable wireless communication systems, and introduce possible future research directions. It will also summarize the contribution of the work that is presented here in the area of adaptive and reconfigurable RF/microwave circuits and possible new applications.

# CHAPTER 2

# Design, Performance, and Modeling of Switchable, Tunable, and Reconfigurable BST FBARs

## 2.1. Introduction

High performance, compact, and low cost resonators are essential components for modern wireless communication systems. State-of-the-art resonators that are currently being used for mobile applications are generally a type of electroacoustic resonator [26]. Electroacoustic resonators behave similarly to electromagnetic metallic and dielectric resonators in that the resonant structure imposes boundary conditions that can only be satisfied by waves with particular frequencies. However, electroacoustic resonators have several advantages that have allowed them to become commercially successful. First, the propagation velocity of acoustic waves in solids, which is in the range of several thousands of meters per second, results in design features that are on the order of several microns for devices operating in the hundreds of MHz to GHz frequency range. The small features allow the devices to have a small footprint while also being matched to standard 50 Ω components. Second, high quality materials commonly used in the semiconductor industry such as silicon have very low acoustic loss at RF and microwave frequencies [27]. This increases the achievable quality factor of a resonator, an important figure of merit for

frequency selective circuits, and reduces the overall power consumption of the circuits they are used in. Third, they can be mass produced using standard CMOS and MEMS based fabrication technology. All of these factors have led to the maturation and widespread use of electroacoustic devices for many applications such as oscillator, filter, and sensors [27].

Electroacoustic resonators are generally categorized as either surface acoustic wave (SAW) or bulk acoustic wave (BAW) devices. Both types of resonators have a series and a parallel resonance frequency. The series resonance frequency is determined by the dimensions of the device relative to the structure's effective acoustic wave velocity. The parallel resonance frequency is higher than the series resonance frequency by a value that is proportional to the effective electromechanical coupling coefficient of the resonating structure [26]. The difference between the two types of electroacoustic resonators is the types of acoustic waves that are generated, confined, and converted into electrical resonances, and the type of waves that are generated is determined by the physical structure of the resonator [27].

SAW resonators consist of a piezoelectric substrate or thin film (e.g. quartz, lithium niobate, lead zirconate titanate (PZT), and aluminum nitride) that is covered by interdigitated metal electrodes [27]. The piezoelectric material allows the RF signals applied to the interdigitated electrodes to produce laterally propagating surface acoustic waves and also allows the propagating surface acoustic waves to exhibit an electrical resonance. The patterning of the electrodes dictates the resonance frequency, quality factor, impedance level, and other electrical parameters of the device [27].

BAW resonators consist of a piezoelectric slab with metal electrodes on the top and/or bottom surface. RF signals applied to the electrodes produce acoustic waves that propagate

within the bulk of the slab and the propagating bulk acoustic waves can in turn generate an electrical response. The acoustic waves are confined within the resonator due to the acoustic impedance mismatch between the resonator body and its surrounding environment. The two methods of confining the bulk acoustic waves divide BAW resonators into two different categories. The first type of BAW resonator is the solidly mounted resonator (SMR). It utilizes an acoustic Bragg reflector, which consists of alternating quarter-wavelengths of high and low acoustic impedance materials, to contain the acoustic waves of a particular set of frequencies [27]. The second type is the film bulk acoustic wave resonator (FBAR). It utilizes MEMS processing techniques to remove the material surrounding the resonator body and relies on the large acoustic impedance mismatch between the resonator body and the surrounding air/vacuum to contain acoustic waves of a particular set of frequencies [26]. Both FBARs and SMRs have resonance frequencies that are determined by the thickness of the thin films that make up the device.

While both types of BAW resonators have been very commercially successful in the telecommunications industry and have been spreading into other markets, each have their own advantages. SMRs are very mechanically robust and the film stress within the transducing layer and electrodes are minimal [27]. Furthermore, SMRs have better heat dissipation capabilities, which can allow for higher power handling [27]. FBARs on the other hand can achieve higher effective electromechanical coupling coefficients and quality factors since the Bragg reflector can serve as an additional source of energy loss [28]. Also, it is easier to design and fabricate FBARs of widely varying frequency on a single substrate since there is no need to consider the operating frequency range of a Bragg reflector. Based on the motivation behind this work, the fabrication processes/equipment

available for use, and performance goals, the FBAR structure was chosen for demonstrating the capabilities of BST thin film technology.

FBARs can be designed with a variety of configurations. For example, they can be configured as either one- or two-port devices. One-port devices, which have the configuration shown in Figure 2.1(a), are generally used in VCO design and can be easily characterized by plotting the measured input impedance on the Smith Chart [27]. Two-port devices, which have the configuration in Figure 2.1(b), are generally used in filter design and can be measured more accurately since network analyzers can achieve higher sensitivity when measuring transmission coefficients than reflection coefficients [26]. Furthermore, in contrast to the common bottom electrode, transduction layer, and top electrode configuration, FBARs can be designed with a layer of very high quality and low acoustic loss material, such as silicon, beneath the bottom electrode to create a composite structure for enhancing certain performance aspect of the device [26, 27, 29]. Figure 2.2(a) shows the cross section of a traditional, non-composite FBAR and Figure 2.2(b) shows a composite FBAR. In this chapter, the design, performance, and modeling of non-composite one-port FBARs using a BST thin film transduction layer is the main focus.

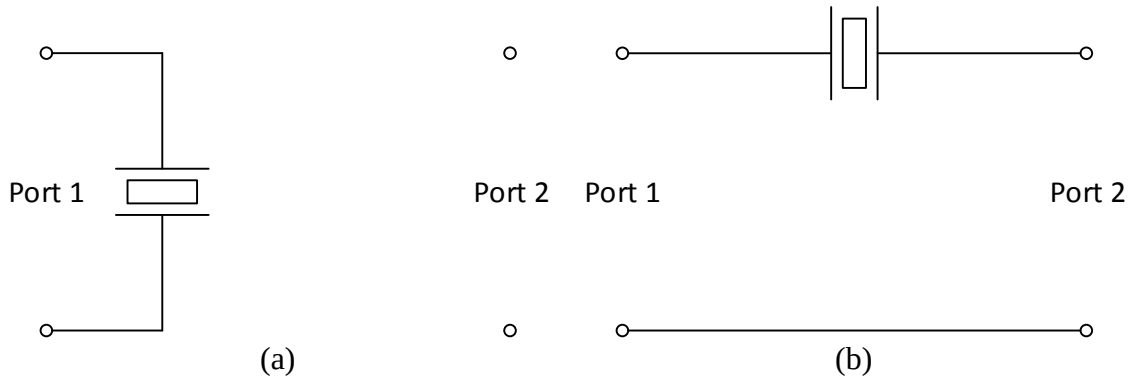

Figure 2.1: Configuration of (a) one- and (b) two-port BST FBARs shown in schematic form.

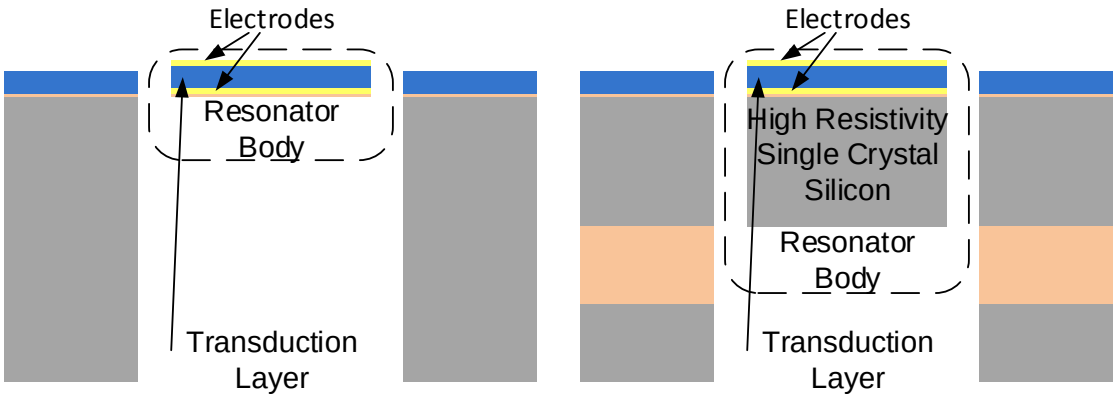

Figure 2.2: Cross section of a (a) traditional, non-composite and (b) composite BST FBAR.

## 2.2. BST FBARs

BST FBARs are acoustically resonant membranes that consist of a BST thin film sandwiched between a pair of top and bottom electrodes, as shown in Figure 2.3. The properties of BST provide a couple advantages for designing bulk acoustic wave resonators. First, BST has a high relative permittivity in the several hundred, which allows for the design of much smaller resonators than compared to those based on traditional piezoelectric materials. Second, BST exhibits electrostriction and electric field induced piezoelectricity, which allows for the design of intrinsically switchable and tunable bulk acoustic wave resonators. This is illustrated by the measured input impedance of a BST FBAR when it is in the off state, which occurs with a 0 V dc bias, and when it is in the on state with a 5 to 25 V dc bias, as shown in Figure 2.4.

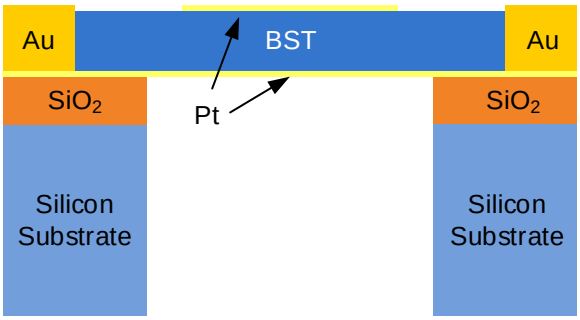


Figure 2.3: Cross section of a BST FBAR.

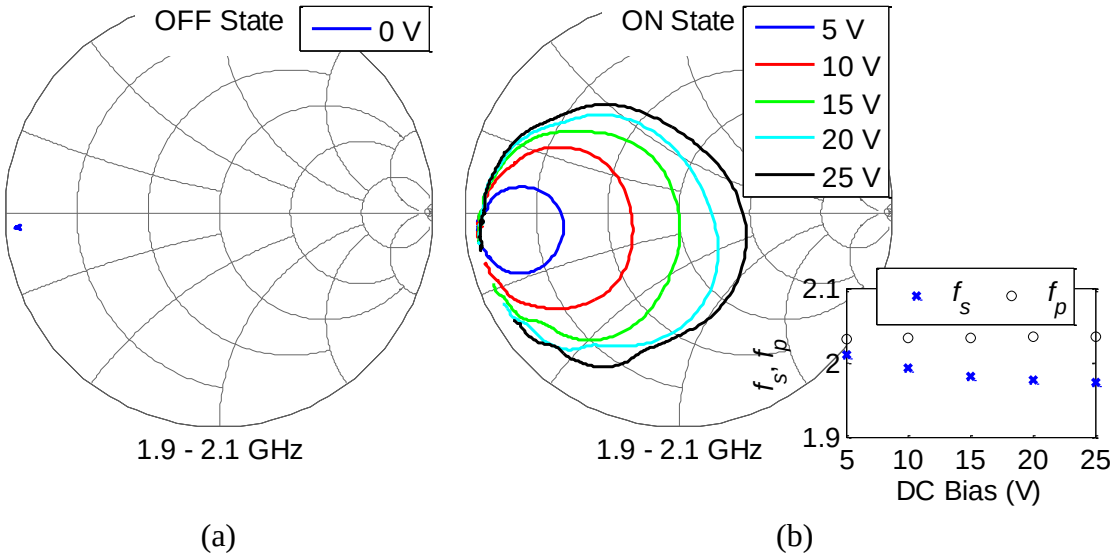


(a) (b)

Figure 2.4: Measured response of a $Ba_{0.5}Sr_{0.5}TiO_3$ FBAR at various bias voltages.

The unique ability of BST FBARs to switch on and off with the application of a dc bias voltage and have their resonances be tuned by controlling the bias voltage level is due to BST's strong electrostrictive properties. In order to understand the mechanism behind this behavior, piezoelectricity and electric field induced piezoelectricity are discussed with respect to their role in realizing electroacoustic resonators. Traditional bulk acoustic wave resonators that utilize piezoelectric materials to excite an acoustic wave within the bulk of the structure in response to an applied RF signal always exhibit an electrical resonance. This is because the coupling between the strain and electric field within the piezoelectric material is always present regardless of the external electric field, as shown in the left of

Figure 2.5. Thus, the acoustically resonant cavity can always be excited and result in a resonance behavior. In contrast, recently demonstrated ferroelectric BST based bulk acoustic wave resonators do not exhibit a piezoelectric response in their natural unbiased state and cannot excite acoustic waves within the ferroelectric layer. Therefore, under normal circumstances, BST resonators do not exhibit an electrical resonance. However, when a dc bias voltage is applied across the ferroelectric thin film, the electric field displaces the center titanium ion in the perovskite crystal lattice, polarizing the material to exhibit electric field induced piezoelectricity (see Figure 1.4), and applied RF signals are able to excite acoustic waves within the bulk of the resonator, as illustrated in the right of Figure 2.5.

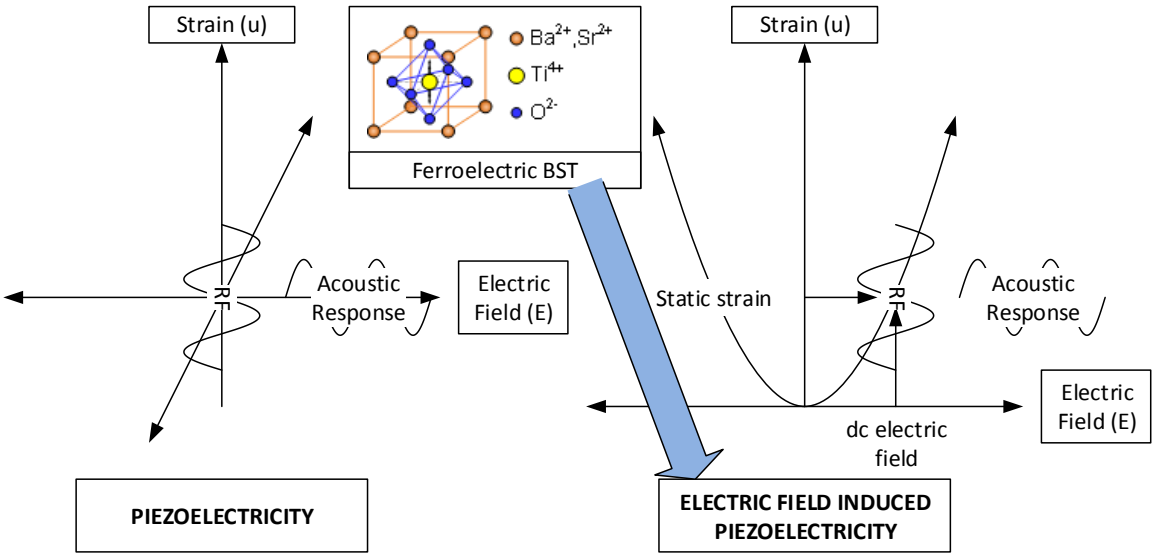


Figure 2.5: Illustration showing the electric field induced piezoelectricity of BST as a result of its strong electrostrictive response.

The resulting coupling between the electrical and acoustic waves gives rise to an electrical resonance. Another consequence of utilizing electrostrictive BST is that as the dc electric field strength increases, the piezoelectric effect grows stronger and causes the

electromechanical coupling coefficient, the ratio of electrical to mechanical energy densities, of the BST thin film to increase, as shown in Figure 2.6. Furthermore, due to BST's dc electric field dependent permittivity and polarization as well as its nonlinear electrostrictive effects, the resonance frequencies of BST FBARs can be tuned by controlling the dc bias level [30, 31]. Lastly, by removing the dc bias, the titanium ion to returns to the center of the BST unit cell (given that the material is in its paraelectric state), eliminating any electrical resonance that once existed. In order to design a BST FBAR, we need to consider the properties of the device at a particular bias voltage and determine the behavior of the excited acoustic waves that propagate within the resonator. This can be done by using transmission line theory as discussed in the next section.

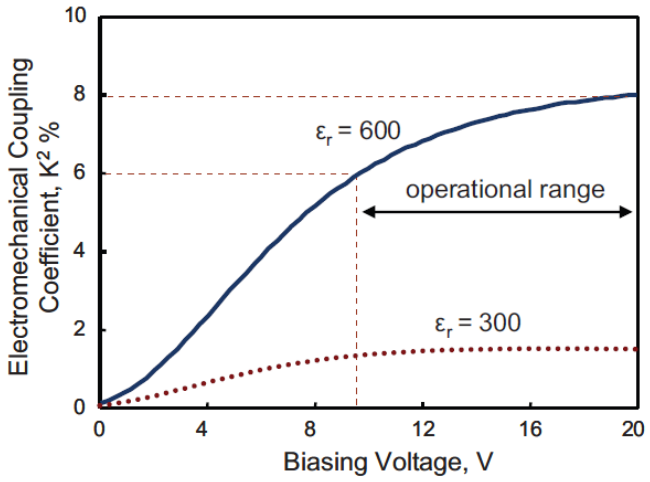


(b)

Figure 2.6: Dependence of the electromechanical coupling coefficient, which is related to the effective piezoelectric coefficient, as a function of dc bias voltage. Reproduced from [32].

## 2.2.1. Design and Simulation

### 2.2.1.1. Analytical Design

BST FBARs are electroacoustic devices that utilize electrostriction to switch on and off their electrical resonances and tune their resonance frequencies. The phenomenon of electrostriction is quite complex and involves many material parameters that are difficult to characterize. However, it is possible to design of BST FBARs without directly considering electrostriction by separately considering the electrical and acoustic properties of the device and utilizing the electromechanical coupling coefficient of BST thin films. The method discussed in this section can be used for the initial design of a BST FBAR and subsequently an iterative design process can be used to more accurately predict the behavior of the fabricated and characterized devices.

The overall frequency response of a BST FBAR can be determined using the acoustic transmission line model shown in Figure 2.7 [33]. With this design technique, the acoustic properties of each material, such as stiffness constant ($E$), mass density ($\rho$), acoustic quality factor ($Q_A$), and acoustic wavelength ($\lambda_A$) are used to calculate the acoustic wave velocity ($v_A$), acoustic impedance ($Z_A$), acoustic propagation constant ($\beta$), and acoustic propagation coefficient ($\gamma_A$) for each layer:

$$v_A = \sqrt{\frac{E}{\rho}} \tag{2.1}$$

$$Z_A = \sqrt{E \cdot \rho} \tag{2.2}$$

$$\beta = \frac{2\pi}{\lambda_A} \tag{2.3}$$

$$\gamma_A = \frac{\beta}{2 \cdot Q_A} + j\beta \tag{2.4}$$

Then, the input impedance of the FBAR is determined by modeling each layer as an acoustic transmission line of thickness $t$ that is terminated with a load $Z_A$ by using (2.5).

$$Z_{in} = Z_A \frac{Z_L + Z_A \tanh(\gamma_A t)}{Z_A + Z_L \tanh(\gamma_A t)} \tag{2.5}$$

Subsequently, the acoustic impedances (normalized by the acoustic impedance of BST) seen by the top and bottom of the BST layer ($z_t$, $z_b$), the electrical capacitance ($C$) due to the overlapping top and bottom electrodes, and the electromechanical coupling coefficient ($K^2$) of the BST are used in (2.6) to calculate the overall input impedance of the resonator ($Z_R$), where $\phi$ is half of the acoustic phase delay for the BST layer. The thickness of each layer and the overlap area of the top and bottom electrodes are chosen to obtain the desired frequency response from the FBAR.

$$Z_R = \frac{1}{j\omega C}\left[1 - K^2 \frac{\tan\phi}{\phi} \frac{(z_t + z_b)\cos^2\phi + j\sin 2\phi}{(z_t + z_b)\cos 2\phi + j(z_t z_b + 1)\sin 2\phi}\right] \tag{2.6}$$

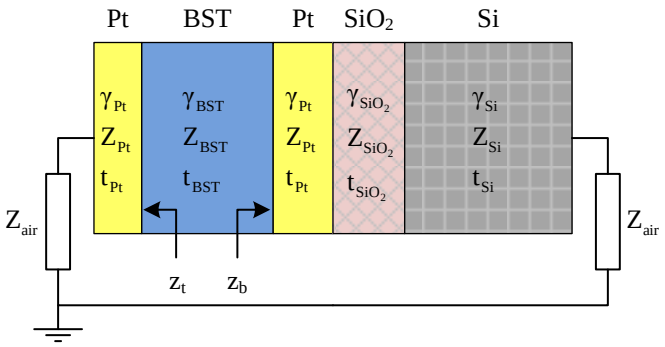


Figure 2.7: Acoustic wave transmission line model for designing FBARs and FBAR filters.

#### 2.2.1.2. Multiphysics Simulation

The analytically derived design parameters for obtaining the desired frequency response can be verified by performing multiphysics based simulations. Here, COMSOL Multiphysics (COMSOL) is used to perform 2D simulations in order to demonstrate what is physically taking place within the FBAR structure.

The 2D cross section of a BST FBAR is drawn in COMSOL and the properties of platinum and BST used in the simulation are initially obtained through the COMSOL material library and then modified to represent the materials grown in our fabrication facility. The simplest simulation to perform is to solve for the eigenfrequencies of the structure. Once the eigenfrequencies are known, the total displacement of the resonator body can be obtained. An FBAR consisting of platinum bottom and top electrodes that are 100 nm thick and a BST layer that is 400 nm thick has been simulated. Figure 2.8(a) shows the eigenmode of the FBAR at its eigenfrequency of 2.6 GHz where the different colors indicate the total displacement of the resonator body and Figure 2.8(b) shows the exaggerated deformation of the resonator. We see that the displacement is the largest at the top and bottom boundary of the structure, which is where the strain of the material must be zero due to the boundary conditions. This is the desired fundamental resonance mode for FBARs. COMSOL can also be used to simulate the frequency response of the BST FBAR. However, due to the relatively simple and well understood nature of the FBARs in addition to the sufficient accuracy afforded by the acoustic wave transmission line, it is not discussed here but will be discussed in Chapter 4 for a different type of resonator structure.

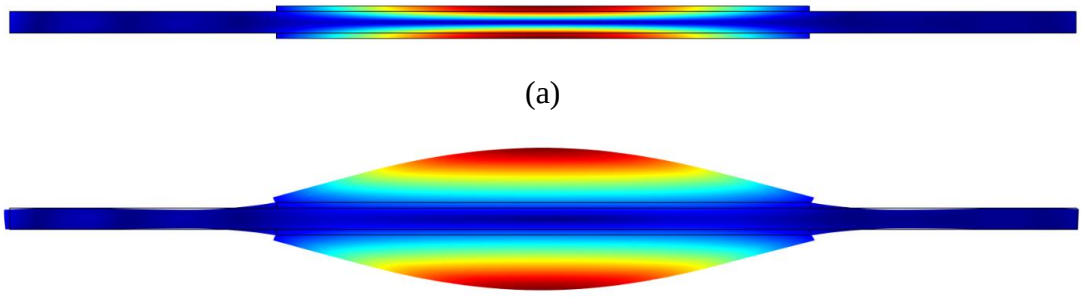

(a)

(b)

Figure 2.8: COMSOL Multiphysics simulation results showing the desired resonance mode of a BST FBAR. (a) The total displacement of the FBAR at different regions is shown by the color. (b) The deformation of the FBAR is shown.

### 2.2.2. Device Fabrication and Measurement Setup

After using the acoustic wave transmission line model to obtain a preliminary design and COMSOL multiphysics to verify that the desired resonance mode is obtained, BST FBARs are fabricated in the Lurie Nanofabrication Facility (LNF) located within the Electrical Engineering and Computer Science building at the University of Michigan using the procedure illustrated in Figure 2.9. BST FBARs are fabricated on high resistivity silicon substrates that are 525 μm thick and have a resistivity of 3 kΩ·cm [Figure 2.9(a)]. Fabrication begins by growing a 100 nm $SiO_2$ thermal oxide on the wafer [Figure 2.9(b)]. Next, a 100 nm platinum bottom electrode and a 3 nm titanium adhesion layer is deposited by electron beam evaporation and patterned by standard photolithography and liftoff procedures [Figure 2.9(c)]. A BST thin film is then deposited by pulsed laser deposition (PLD) using an excimer laser ($\lambda$ = 248 nm, pulse width = 25 ns, repetition rate = 5 Hz) and the deposition parameters listed in Table 2.1 [Figure 2.9(d), Figure 2.10]. (Here, the thermal oxide between the silicon wafer and platinum bottom electrode prevents the formation of platinum silicide, which would otherwise occur under these growth conditions

[34].) A 100 nm platinum top electrode is deposited using the same procedure as the bottom electrode [Figure 2.9(e)]. The entire wafer is then annealed in an oxygen environment at 500 °C [not shown]. The BST and SiO2 are selectively etched by using diluted hydrofluoric acid for creating vias [Figure 2.9(f)]. A 500 nm gold contact layer with a 50 nm titanium adhesion layer is deposited for the coplanar waveguides (CPWs) through electron beam evaporation [Figure 2.9(g)]. Finally, the devices are released using deep reactive ion etching (DRIE) to etch away the bulk silicon, creating a membrane [Figure 2.9(h)]. A microphotograph of a fabricated device is shown in Figure 2.11.

Table 2.1: PLD Deposition Parameters

| | |
|---|---|
| Target Material | $Ba_{0.5}Sr_{0.5}TiO_3$ |
| Laser Repetition Rate | 10 Hz |
| Laser Power* | 1.12 W |
| Substrate Temperature | 650 ºC |
| Chamber Partial Pressure | 300 mTorr of $O_2$ |
| Deposition Time | Thickness Dependent |
| Post Deposition Anneal Time | 60 minutes |
| Post Deposition Anneal Temperature | 650 ºC |
| Post Deposition Anneal Chamber Pressure | 100 Torr of $O_2$ |
| Post Anneal Cooling Rate | 1 ºC/minute |

*measured just outside of chamber viewport.

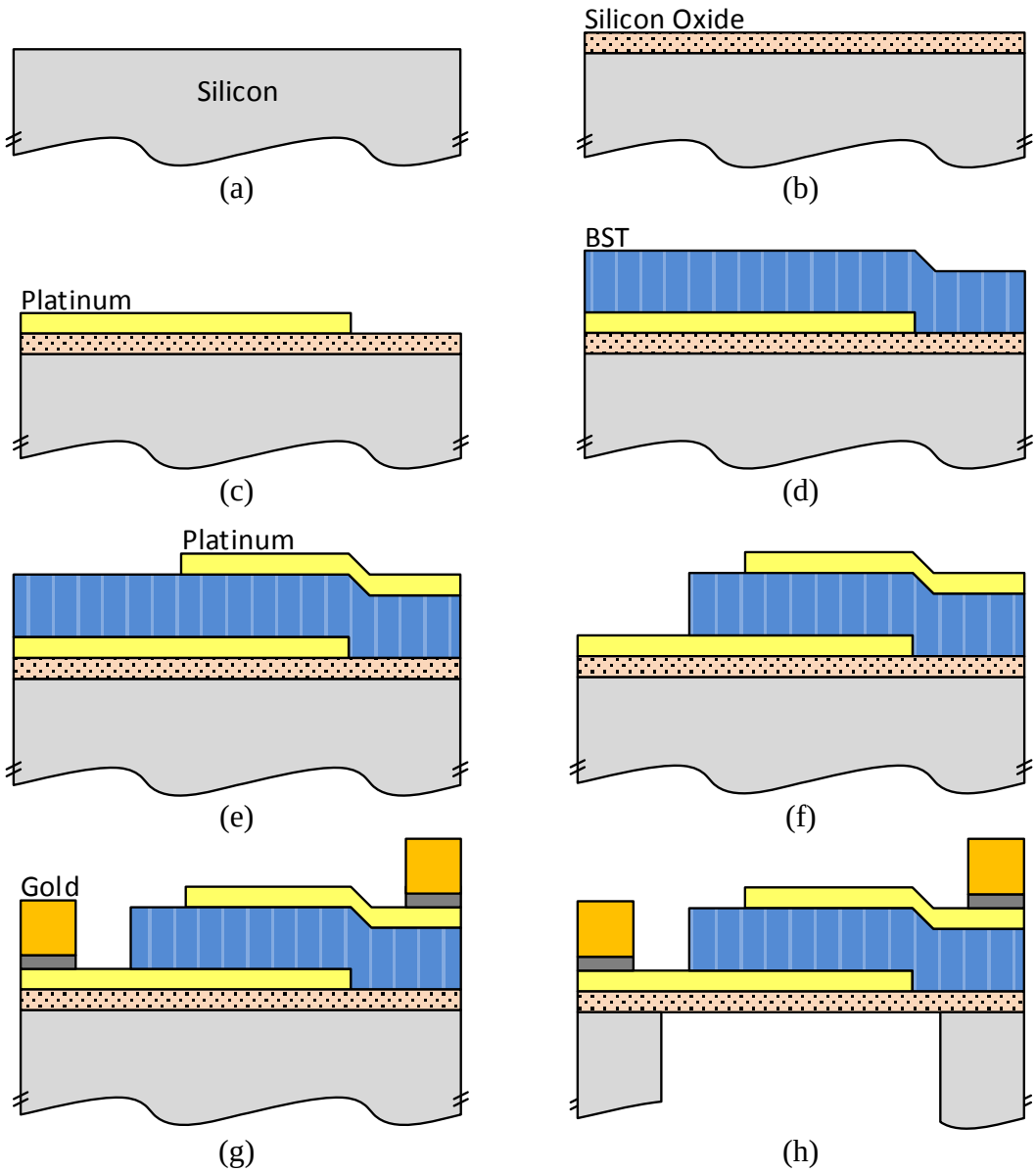

Figure 2.9: Step by step illustration of the fabrication process.

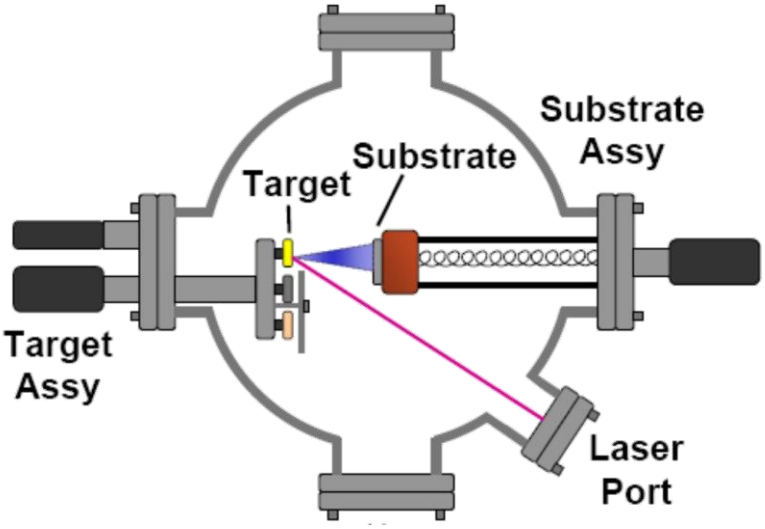

Figure 2.10: Setup of the pulsed laser deposition system used for depositing BST thin films.

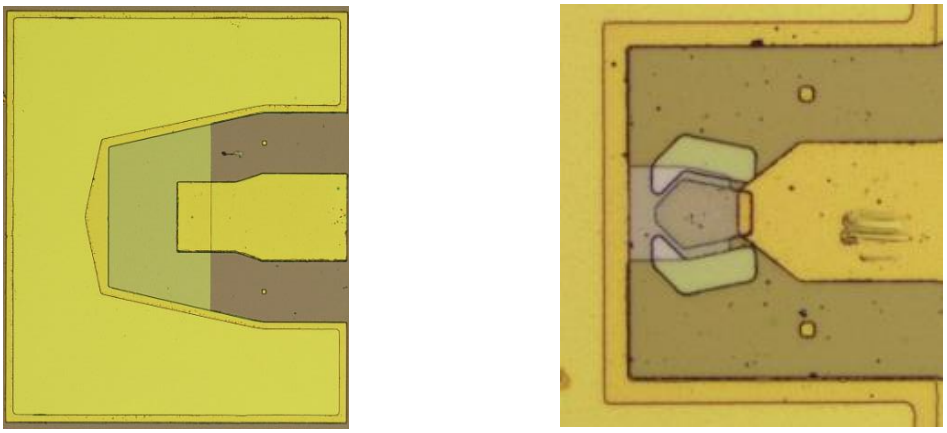
Figure 2.11: Microphotograph of various BST FBARs that have been fabricated.

Device measurements are performed in the open-air and the unpackaged devices are subjected to the ambient pressure, temperature, and humidity of the laboratory environment. The devices under test (DUTs) are mounted on the chuck of a Cascade Microtech probe station and are characterized by using 150 µm pitch GSG probes to make contact with the CPW test structure. DC bias voltages are provided by Agilent E3631A power supplies and applied through the bias-tees that are connected to each of the measurement ports as well as through additional dc probes. The complete setup is

illustrated in Figure 2.12. Short-open-load-through calibration is performed on an Agilent E8364B/C vector network analyzer using a calibration substrate prior to characterizing the DUTs, setting the measurement reference plane at the GSG probe tips. S-parameters are taken over a wide range of frequencies (e.g. from 100 MHz to 5 GHz in 1.5 MHz increments) with various dc bias voltages applied to the device and with -17 dBm up to 10 dBm of RF power available from the source.

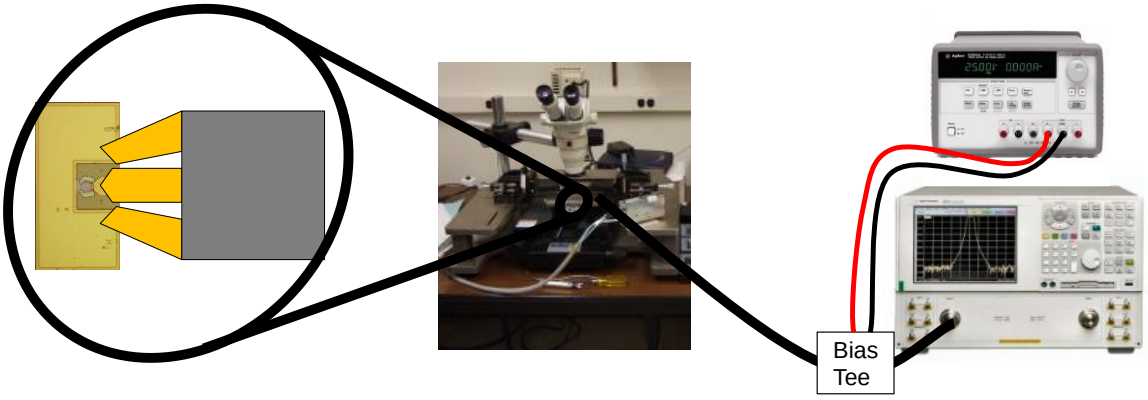


Figure 2.12: Measurement setup for measuring one-port BST FBARs.

## 2.2.3. Performance

Various properties and performance metrics of BST FBARs have been measured and studied in this work. In the following section, the voltage dependent behavior, RF power dependent behavior, and switching reliability of BST FBARs are discussed in detail.

### 2.2.3.1. Voltage Dependent Behavior

The dc voltage applied to BST FBARs controls whether or not the devices resonate and the voltage level controls their resonance frequencies. This behavior allows BST FBARs to be used for the design of switchable and tunable oscillators and filters that do not require

the use of solid-state or MEMS switches. Here, the performance of several different BST FBARs are given to illustrate their properties. All of the FBARs that are presented here have a BST thin film with a Ba:Sr ratio of 1:1 such that the ferroelectric material is in its paraelectric phase when characterized at room temperature.

In the absence of a dc bias voltage, BST FBARs behave as simple capacitors and do not exhibit any type of resonance behavior. This behavior is expected since BST is not piezoelectric under these conditions and therefore, RF signals applied to the device are not able to excite acoustic waves within the body of the resonators. The measured input impedance of a 650 $\mu m^2$ BST FBAR with a 0 V dc bias has been plotted on the Smith Chart from 1.8 to 2.2 GHz with a thick black trace in Figure 2.13 and agrees with the expected behavior of a capacitor.

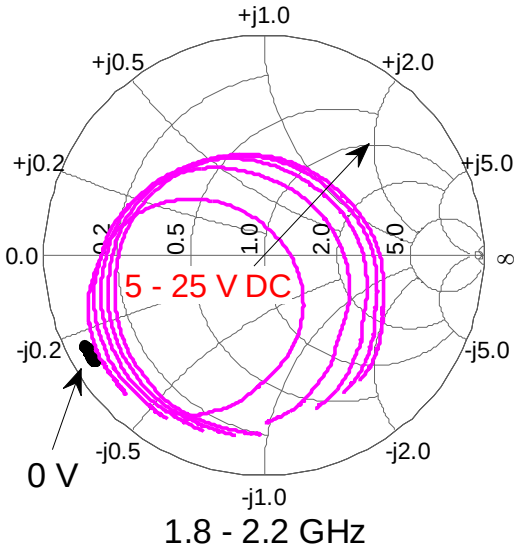


Figure 2.13: The measured input impedance of a one-port BST FBAR measured at dc bias voltages of 0, 5, 10, 15, 20, and 25 V shown on a Smith Chart at frequencies of 1.8 to 2.2 GHz.

When BST FBARs are given a dc bias, an electrical resonance is exhibited and as the bias voltage increases, the resonance grows stronger and the resonance frequency is tuned. The electrical resonance and its increase in strength can be seen from the measured input impedance of the same BST FBAR as previously discussed for dc bias voltages of 5, 10, 15, 20, and 25 V that have been plotted on the Smith Chart with magenta traces in Figure 2.13. When switched on, BST FBARs exhibit both a series resonance frequency ($f_s$) and a parallel resonance frequency ($f_p$), which are defined by the frequency at which the input reactance is zero and the input resistance is minimized and at which the input susceptance is zero and the input conductance is minimized, respectively. The decrease in resonance frequency with increase dc bias voltage is shown in Figure 2.14, which plots the reflection coefficient and input impedance of the BST FBAR at dc bias voltages of 0, 5, 10, 15, 20, and 25 V. Furthermore, the tunability of BST resonators can be calculated for both the series and the parallel resonance by using equation (2.7) and are evaluated to be 5.33% and 1.46% for the series and parallel resonance, respectively, with a $V_{min}$ and $V_{max}$ of $0^{+}$V and 25 V (where the resonance frequency was measured at a voltage just above 0 V for $f(V_{min})$) [35]. The measured resonance frequencies are plotted as a function of dc bias voltage in Figure 2.15.

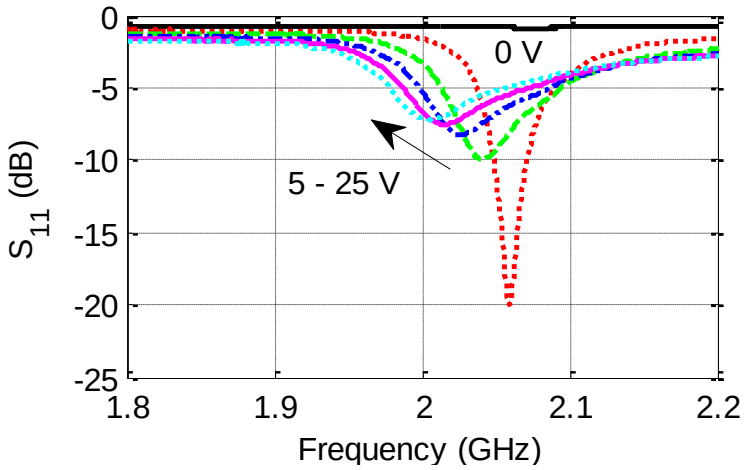


(a)

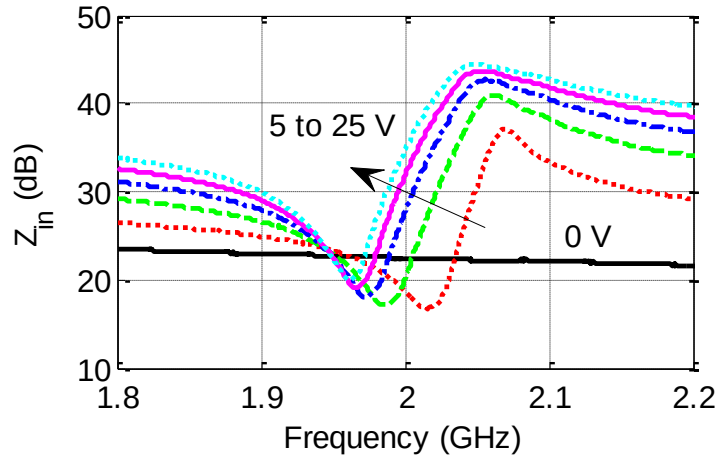


(b)

Figure 2.14: (a) Reflection coefficient and (b) input impedance vs. resonance frequency of a BST FBAR at dc bias voltages of 0, 5, 10, 15, 20, and 25 V.

$$T_f(V_{\min}, V_{\max}) = \frac{f(V_{\min}) - f(V_{\max})}{f(V_{\min})} 100\% \tag{2.7}$$

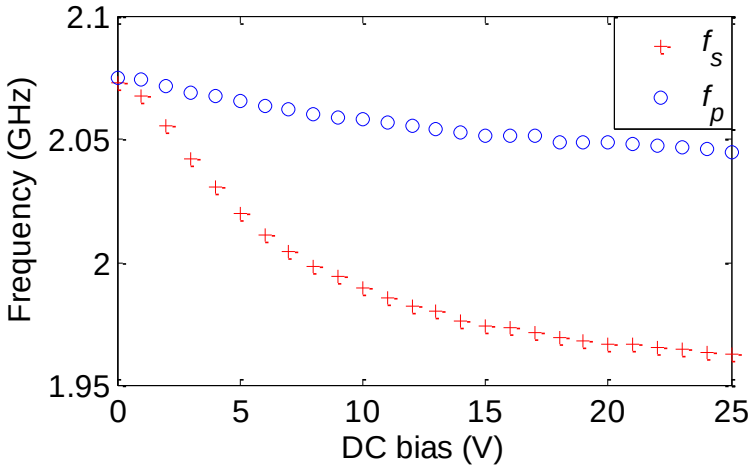


Figure 2.15: Resonance frequencies of a BST FBAR vs. dc bias voltage.

In addition to the changes in resonance frequencies, other properties of BST FBARs also change with dc bias voltage. The enlargement of the impedance-circle traced out on the Smith chart by the resonance of the BST FBAR in Figure 2.13 represents an increase in the effective piezoelectric coefficient and a related figure of merit of resonators, the effective electromechanical coupling coefficient. The effective electromechanical coupling coefficient ($K_t^2{}_{eff}$) for a resonator can be calculated using (2.8), where $f_s$ and $f_p$ are the series and parallel resonance frequencies. It is a measure of the electroacoustic energy conversion efficiency and the higher it is, the better, especially for FBAR filter design. Another important figure of merit for resonators is its quality factor, which represents the losslessness of the resonator and the higher it is the better. The quality factor ($Q$) can be calculated using (2.9), where $d\phi_{Zin}/df$ is the change in the phase of the input impedance with respect to frequency.

$$K_{t,eff}^2 = \frac{\pi}{2}\frac{f_s}{f_p}\tan\left(\frac{\pi}{2}\frac{(f_p - f_s)}{f_p}\right) \tag{2.8}$$

$$Q_{s,p} = \frac{f}{2}\left|\frac{d\phi_{Zin}}{df}\right|,\ f = f_s, f_p \tag{2.9}$$

The $K_t^2{}_{eff}$ and the $Q$ of the measured resonator is listed in Table 2.2 for different dc bias voltages. As bias voltage is increased, the $K_t^2{}_{eff}$ increases significantly and the $Q$ also increases a bit.

Table 2.2: Figures of merit for a BST FBAR for different dc bias voltages

| Bias Voltage | 0 | 5 | 10 | 15 | 20 | 25 |
|---|---|---|---|---|---|---|
| $Q$s | N/A | 64 | 66 | 70 | 74 | 78 |
| $K_t^2{}_{eff}$ | 0 | 4.35 | 7.29 | 8.38 | 8.8 | 8.93 |

### 2.2.3.2. Large Signal Performance

As for most voltage controlled devices, the large signal, RF power dependent, and nonlinear behavior of ferroelectric based devices needs to be characterized before they can be considered for use in high power applications. The nonlinear behavior of ferroelectric varactors [36] and piezoelectric FBARs [37, 38] have been characterized and modeled by various research groups. Here, the large signal and nonlinear behavior of ferroelectric FBARs are investigated.

BST FBARs are measured at frequencies of 100 MHz to 3 GHz and at bias voltages of 0 to 25 V as the power available from the source is swept from -18 to 8 dBm using the same setup shown in Figure 2.6. The measured input impedance of the resonator is plotted in Figure 2.16 at bias voltages of 5 and 25 V and RF power levels of -8, 0, and 8 dBm. Measurement results show that at both 5 and 25 V dc bias, the input impedance of both resonators begins to deviate from their small signal values when the power level is above 0 dBm and as the RF power applied to the device increases beyond 0 dBm, the size of the

impedance-circle on the Smith Chart decreases. This behavior reflects the decrease in the $K_t^2{}_{eff}$ and/or $Q$ of the resonator.

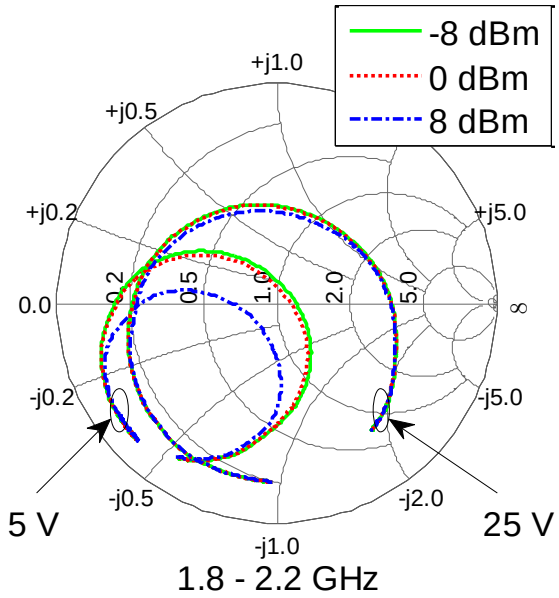


Figure 2.16: The Smith chart showing the input impedance of the BST FBAR at bias voltages of 5 and 25 V and power levels of -8, 0, and 8 dBm.

In order to quantitatively determine the decrease in $Q$ and $K_{t,}^2{}_{eff}$, they have been extracted from the measurement results taken at dc bias voltages of 5, 10, 15, 20, and 25 V and RF power levels of -18 to 8 dBm. Figure 2.17 shows that as the RF input power is increased beyond 0 dBm, $K_{t,}^2{}_{eff}$ and $Q$ begin to notably deviate from their small signal values and decrease. However, the change in performance is decreases as the bias voltage is increased.

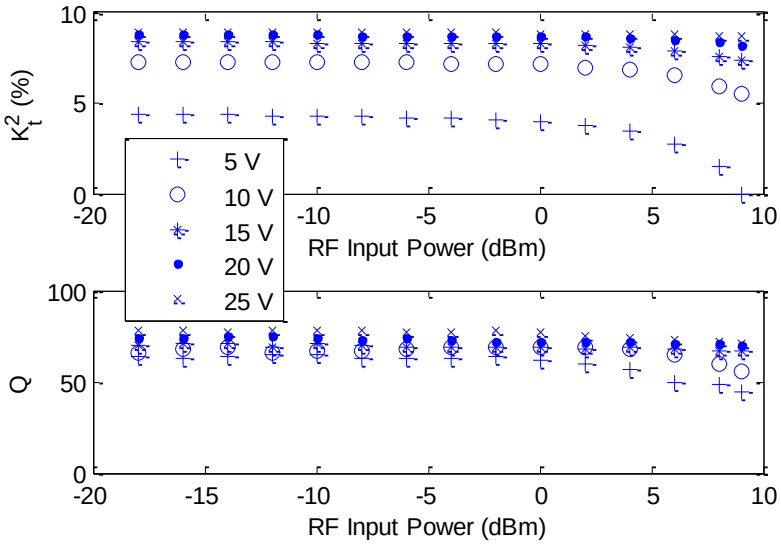


Figure 2.17: $K_{t,}^{2}{}_{eff}$ and $Q$ of the BST FBAR as a function of RF input power at applied dc bias voltages of 5, 10, 15, 20 and 25 V.

The change in the series and parallel resonance frequencies of BST FBAR with dc bias voltage and RF power are shown in Figure 2.18. Ferroelectric FBARs are electrically tunable and as bias voltage is increased, the resonance frequencies decrease, as expected. In addition, as the RF power is increased, the series resonance frequency increases and the parallel resonance frequency decreases. The decreases in the difference between the series and parallel resonance frequency is also expected since it is related to the $K_t^2{}_{eff}$, which decreases with RF power. From the measurement results discussed here, it is concluded that ferroelectric FBARs exhibit more power dependent behavior and nonlinearity at lower bias voltages. Therefore, for certain high power applications, BST FBARs may need higher dc biasing than would otherwise be required.

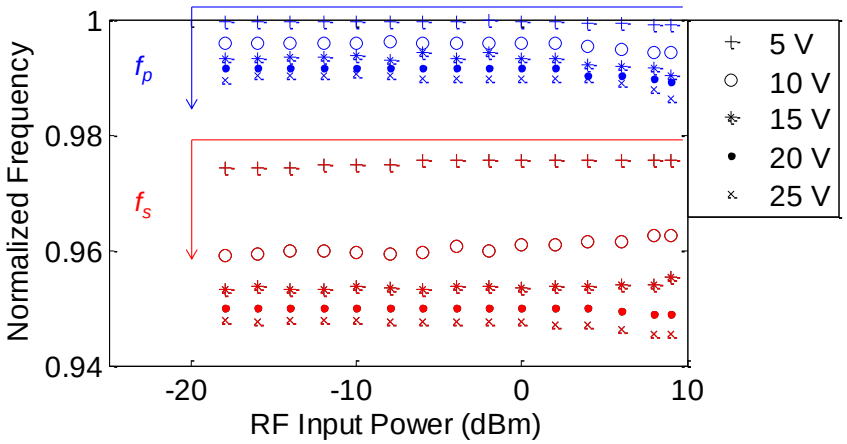


Figure 2.18: Resonance frequency of a BST FBAR as a function of dc bias voltage and RF power level.

### 2.2.3.3. Reliability Test

In order for BST thin film resonators to be widely used in tunable and switchable circuits such as oscillators and filters for commercial/industrial applications, they need to have great reliability. BST based resonators are expected to be very reliable. This is because they are electroacoustic devices and their switchability is directly due to the modification of the BST crystalline structure, which in turn alters its material properties, and is not mechanical in nature like in MEMS. Furthermore, reliability studies of BST based varactors have shown very stable performance over many tuning cycles [39] and for long periods of applied electric field [40]. Therefore, the same reliability is expected of the BST based intrinsically switchable resonators and filters. Here, the switching reliability of these devices is investigated.

The test setup for measuring the switching reliability of FBARs is shown in Figure 2.19. An arbitrary waveform generator is programmed to change between 0 and 10 V at a slew rate of 2 V/μs and 4 V/μs for the rising and falling edge, respectively, with a repetition

rate of 20 kHz (period T = 50 μs), and a duty cycle of approximately 50 %, as shown in Figure 2.19, and is similar to the waveform used in [41] for testing the switching reliability and lifetime of MEMS switches.

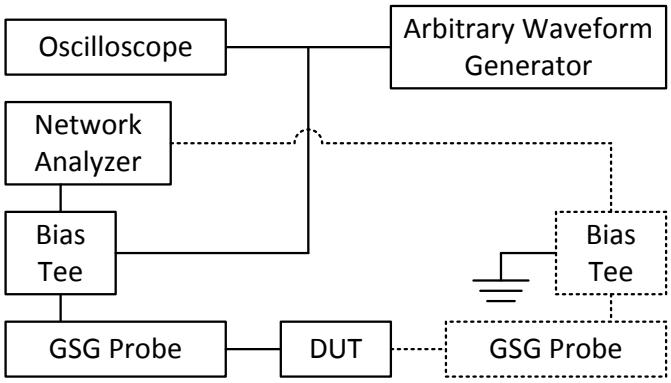


Figure 2.19: Test setup for measuring the switching reliability of FBARs. Biasing is applied through a bias tee. For 2-port FBARs, an additional GSG probe and bias tee are used to connect the 2nd port to the network analyzer.

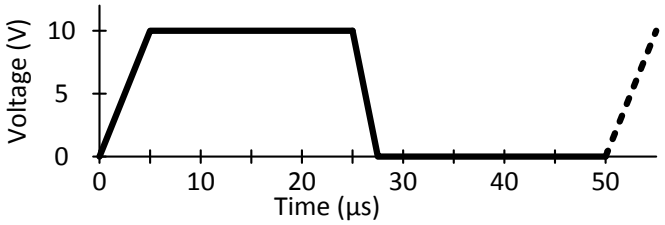


Figure 2.20: Programmed voltage waveform for switching the resonators on and off at a repetition rate of 20 kHz.

The output of the arbitrary waveform generator is connected to the bias-tee and an oscilloscope. An Agilent E8364C network analyzer feeds RF power into the device and measures the *S*-parameters to monitor its performance. The power loss due to the bias tees, cables, and probes have been measured to determine the power at the input and output of the device. The functionality of the DUT is determined by measuring its *S*-parameters with a network analyzer.

Several FBARs are tested for switching reliability and performance degradation. The network analyzer is configured to provide a continuous wave (CW) time sweep. The frequency is set to the average of the series ($f_s$) and parallel ($f_p$) resonance frequencies, which is in the frequency range that is generally of interest for oscillator design [42]. The power delivered to the input of the device is 10 dBm and the device is switched on and off for one billion cycles over a period of 14 hours.

The reliability of a device is determined by measuring its *S*-parameters over the frequency range of interest after many switching cycles. The *S*-parameters for one of the characterized 2-port FBARs after $10^3$, $10^6$, and $10^9$ switching cycles is shown in Figure 2.21 and an excellent overlap between the different traces is observed. This indicates that the device is reliable up to one billion switching cycles and the behavior of the device remains constant when switched on and off. The $K_t^2{}_{eff}$ and $Q$ for one of the characterized 1-port FBARs are summarized in Table 2.3, showing very consistent values after $10^3$, $10^6$, and $10^9$ switching cycles. Overall, the characterized intrinsically switchable BST resonators show very stable performance over many switching cycles.

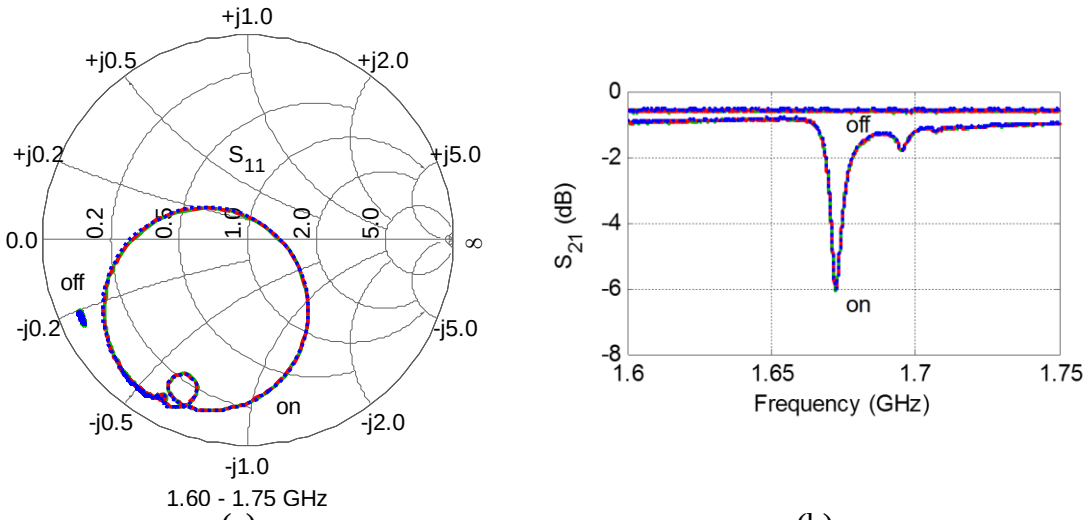


(a) (b)

Figure 2.21: (a) $S_{11}$ (when the 2nd port is shorted to ground through simulation) and (b) $S_{21}$ for a 2-port BST FBAR after $10^3$, $10^6$, and $10^9$ switching cycles.

Table 2.3: One-Port FBAR Figures of Merit

| **Number of Switching Cycles** | $Q_s$ | $Q_p$ | $K_{t,eff}^2$ (%) |
|---|---|---|---|
| $10^0$ | 415 | 552 | 0.80 |
| $10^3$ | 420 | 551 | 0.80 |
| $10^6$ | 417 | 550 | 0.80 |
| $10^9$ | 418 | 555 | 0.80 |

## 2.2.4. Nonlinear Model Parameter Extraction of BST FBARs

Accurate and comprehensive models are necessary to design BST FBAR based circuits. Physics [30, 31] and equivalent circuit based models [43] that represent the dc bias voltage dependent behavior of ferroelectric resonators have been developed. Furthermore, models that represent the nonlinear behavior of ferroelectric varactors [36] and piezoelectric FBARs [37, 38] have also been developed by various research groups. However, the large signal and nonlinear behavior of ferroelectric FBARs have yet to be modeled.

The nonlinear modified Butterworth-Van Dyke (MBVD) model shown in Figure 2.22 has been developed to represent the behavior observed in the large signal measurement results of BST FBARs. The model consists of the seven lumped elements defined in Figure 2.22 where the values of $L_m$ and $C_m$ determine $f_s$, the values of $L_m$, $C_m$, and $C_0$ determine $f_p$, and the rest of the components represent undesired parasitics.

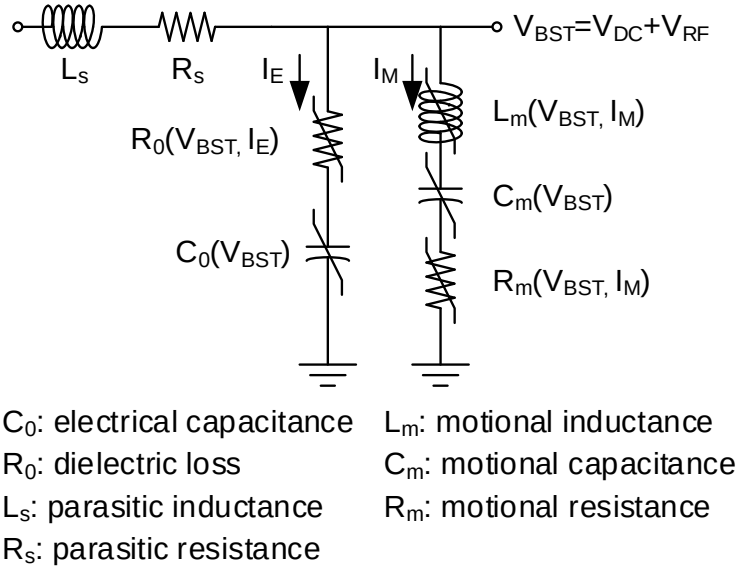


Figure 2.22: A Nonlinear MBVD model used to represent the large signal behavior of ferroelectric thin film FBARs.

The summary of the procedure for generating the nonlinear MBVD model for a measured device is as follows. First, the voltage dependent small signal equivalent circuit model parameters are extracted from the measurement results at the various dc bias voltages and fitted to a polynomial such that the value of each element is a function of the voltage across the device ($V_{BST}$), similar to the procedure used in [9]. Subsequently, additional current dependent nonlinear parameters ($I_M$, $I_E$) are incorporated into $R_0$, $L_m$, and $R_m$. Lastly, the nonlinear model is imported into a microwave circuit simulator and

analyzed using large signal *S*-parameters at different power levels and compared to measurement results.

The Smith Chart in Figure 2.23 shows the good agreement between the modeling and the measurement results. The solid traces in Figure 2.23(a) show the small signal performance of a BST FBAR at 4, 6, and 8 V dc bias while the dashed traces show the modeling results. In addition, the solid traces in Figure 2.23(b) show the power dependent performance at 0, 4, and 8 dBm at a dc bias of 5 V while the dashed traces show the modeling results. This nonlinear model shows a good match with measurement results and can be used in commercial circuit design tools for non-linear analysis and to better understand the effect of high power on ferroelectric based devices. More work on the nonlinear modeling of BST thin film resonators is discussed in greater detail in [44-46].

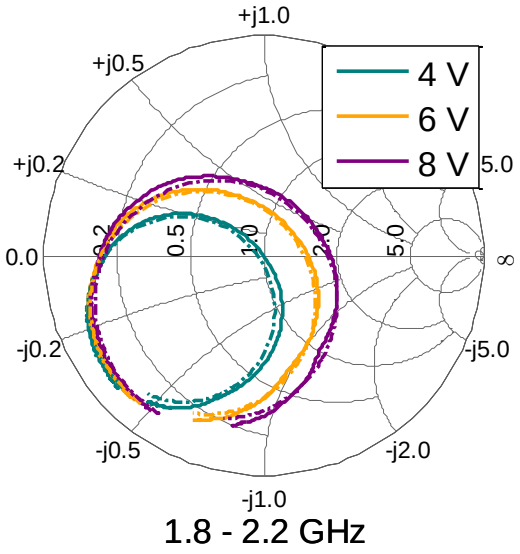


(a)

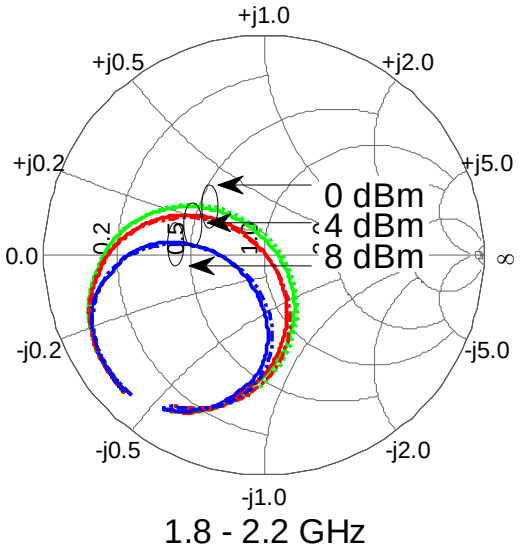


(b)

Figure 2.23: Comparison between the measurement (solid line) and nonlinear MBVD model results (dotted line) at (a) -17 dBm of RF power and dc bias voltages of 4, 6, and 8 V and (b) dc bias voltage of 5 V and RF power levels of 0, 4, and 8 dBm.

## 2.3. Reconfigurable Dual-Frequency BST FBAR

### 2.3.1. Design

Multiple intrinsically switchable and tunable BST FBARs can be integrated to create reconfigurable multi-frequency resonators. The resonance frequency is determined by controlling the dc bias voltage applied across each of the FBARs that make up the device. The FBARs can either be connected together in series or in parallel. A comparison between the two configurations has been performed through simulation with Advanced Design System. In the study, each FBAR is represented using the modified Butterworth-Van Dyke (MBVD) model, which is shown in Figure 2.22, due to its simplicity and accuracy.

The MBVD model used in the simulation is given the attributes listed in Table 2.4. The model uses two different set of parameters, one for when the BST resonator is switched on and the other for when it is switched off. The main differences between the two states is that when the resonator is switched on, the electromechanical coupling coefficient ($K^2$) of the BST thin film is 7% and the impedance ($Z_0$) is 50 Ω, and in contrast, when the resonator is switched off, $K^2$ is 0% and $Z_0$ is 50/τ Ω. Here, the change in $K^2$ represents the change in the electric field induced piezoelectric behavior of the BST thin film and the ability to excite acoustic waves within the resonator body. The change in $Z_0$ represents the change in the device capacitance. The parameter τ represents the dielectric tunability of the BST thin film and is varied in this study to determine its role on the performance of multi-frequency resonators.

Table 2.4:
MBVD Model Attributes

| Property | Expression | On Value | Off Value |
|---|---|---|---|
| Acoustic Quality Factor ($Q_m$) | $2\pi f_s L_m/R_m$ | 150 | 150 |
| Dielectric Loss Tangent (tanδ) | $R_e C_e 2\pi f_s$ | 0.02 | 0.02 |
| Electrode Resistance ($R_s$) | - | 1 Ω | 1 Ω |
| Series Resonance Frequency ( $f_s$) | $1/(2\pi(L_m C_m)^{0.5})$ | 1 GHz | 1 GHz |
| Electromechanical Coupling Coefficient ($K^2$) | $1.2 \cdot C_m/C_e$ | 7% | 0% |
| Impedance ($Z_0$) | $1/(2\pi f_s C_e)$ | 50 Ω | $50/\tau$ Ω |
| Dielectric Tunability ($\tau$) | $C_{e,\,max}/C_{e,\,min}$ | - | 1 to 4 |

In the simulation of the multi-frequency BST resonator model, one resonator is switched on while all others are switched off. An additional series inductor and resistor, with values of 0.1 nH and 1.5 Ω, respectively, are included in the model to represent the parasitic contributions from the contact pads used for characterizing the device. The number of resonators arranged in series and in parallel as well as the dielectric tunability of the BST thin film are varied. The different configurations are simulated to extract the *Q*s and $K_{t,}{}^2{}_{eff}$.

Table 2.5:
Figures-of-Merit for the Simulated FBAR Configurations

| | | $K_{t,}^{2}{}_{eff}$ (%) | $Q_s$ | $Q_p$ |
|---|---|---|---|---|
| Single Resonator | $\tau$ = N/A | 6.9 | 101 | 128 |
| Two in Parallel | $\tau$ = 1 | 3.6 | 95 | 119 |
| | $\tau$ = 4 | 1.8 | 67 | 81 |
| Two in Series | $\tau$ = 1 | 3.5 | 113 | 121 |
| | $\tau$ = 4 | 5.5 | 101 | 126 |
| Four in Parallel | $\tau$ = 1 | 2.0 | 77 | 99 |
| | $\tau$ = 4 | 1.2 | 28 | 43 |
| Four in Series | $\tau$ = 1 | 1.8 | 98 | 102 |
| | $\tau$ = 4 | 4.0 | 102 | 123 |

The simulation results for a single intrinsically switchable and tunable BST resonator as well as for the different multi-frequency resonator configurations that are considered here are summarized in Table 2.5. From the data, it is concluded that the resonators that have been switched off in both the series and parallel configuration reduces the $K_{t,}^{2}{}_{eff}$ of the resonator that is switched on. This occurs when the resonators are placed in series because the series capacitance due the resonators that are switched off increases $f_s$ as calculated by (2.10), (where $C_L$ is the effective series capacitance of the off devices [33]) and occurs when the resonators are placed in parallel since the shunt capacitance due to the resonators that are switched off decreases $f_p$ as calculated by (2.11).

$$f_{s,series} = \frac{1}{2\pi}\sqrt{\frac{1}{L_m C_m} + \frac{1}{L_m (C_0 + C_L)}} \tag{2.10}$$

$$f_{p,parallel} = f_s \sqrt{\frac{C_m + C_0 + C_L}{C_0 + C_L}} \tag{2.11}$$

However, it is also important to note that when the τ of the device is larger, the reduction in $K_{t,}^{2}{}_{eff}$ decreases when the resonators are placed in series and increases when the resonators are placed in parallel. This is in agreement with what is expected when considering (2.10) and (2.11), and is in support of using the series configuration.

The effect of the resonator configuration on quality factors (*Q*s) are also investigated. From the simulation results, it is concluded that the effect of placing the devices in parallel decreases the *Q*s more severely in comparison to placing them in series. The performance difference widens when taking into consideration the dielectric tunability of BST. This also supports the use of the series configuration. In general, as the equivalent capacitance of the resonators that are switched off increases, they behave more similar to an RF short. Therefore, when considering the electric field dependent capacitance of BST FBARs, it is more beneficial to use the series configuration for designing multi-frequency reconfigurable resonators.

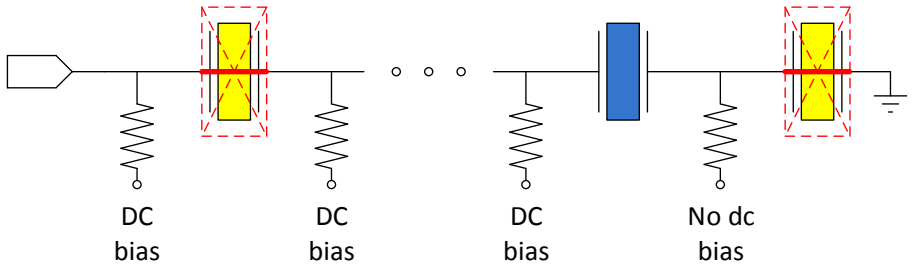


Figure 2.24: Schematic of a series connected multi-frequency BST FBAR. The resonator shown in blue is on and the resonators shown in yellow are off.

In the series connected configuration, multi-frequency BST resonators only require the addition of inductors or resistors to each node of the device, as shown in Figure 2.24, for dc biasing. Individual resonators are switched on by applying different dc bias voltages across its terminals. For switching on only a single resonator, a thermometer-style biasing scheme where the dc bias voltages applied to the all the nodes to the left and right of a particular device are the same is used. To demonstrate the multi-frequency resonator design discussed here, a simple dual-frequency BST resonator, which consists of two series

connected 80 μm × 80 μm BST FBARs and has the configuration shown in Figure 2.25, is fabricated and characterized as described in the next section.

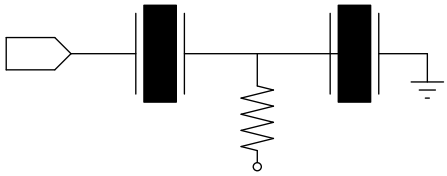

Figure 2.25: Schematic of a dual-frequency BST FBAR.

## 2.3.2. Fabrication and Measurement Procedure

Multi-frequency BST FBARs are fabricated using a similar procedure as described for individual BST FBARs. The only additional steps are the deposition of a thin layer of high resistivity material such as SiCr, chromium, nickel-chromium, or even platinum to create thin film resistors as well as mass loading/compensation layers to shift the frequency of the resonators. A microphotograph of a fabricated dual-frequency BST FBAR is shown in Figure 2.26. The fabricated device is characterized by using a vector network analyzer to measure the reflection coefficient of the one-port device. The thermometer style biasing scheme used for characterizing the device is implemented by using a bias tee to control the bias voltage at the port of the device a dc probe to control the bias voltage at the inner node of the device.

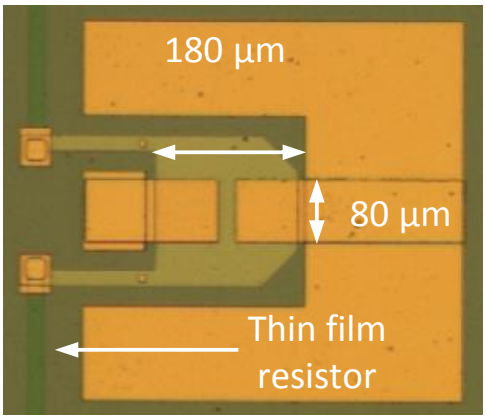

Figure 2.26: Microphotograph of a fabricated dual-frequency BST FBAR.

### 2.3.3. Performance

The fabricated dual-frequency resonators that consist of two series connected intrinsically switchable and tunable BST FBARs are characterized under various biasing conditions. The bias voltage at the port is applied through a bias-tee and the bias voltage at the inner node is applied through a dc probe. When the port and inner node are not biased, the resonator behaves as a capacitor, as shown in Figure 2.27(a), and each BST FBAR has a capacitance of 24.4 pF. When the thermometer-style biasing scheme is used to switch on an individual FBAR with the application of 20 V dc bias across its terminals, both a series and parallel resonance are excited with the application of an RF signal, resulting in the responses shown in Figure 2.27(b), and the capacitance of each FBAR decreases to 10.2 pF. When the low frequency BST FBAR is switched on, a series and parallel resonance frequency of 936.1 MHz and 949.8 MHz is obtained, respectively, which corresponds to a $K_{t,}^{2}{}_{eff}$ of 3.5 %. The *Q*s for the series and parallel resonance are 98 and 90, respectively. When the high frequency BST FBAR is switched, a series and parallel resonance frequency

of 1.136 GHz and 1.153 GHz is obtained, respectively, which corresponds to a $K_{t,eff}^2$ of 3.6 %. The *Q*s for the series and parallel resonance are 100 and 99, respectively.

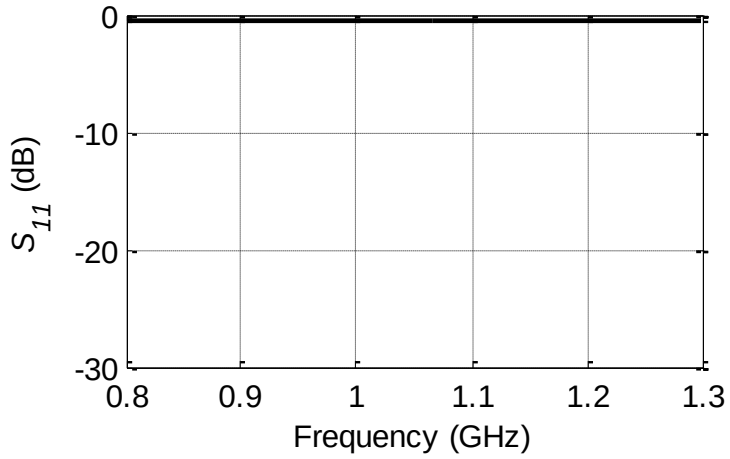


(a)

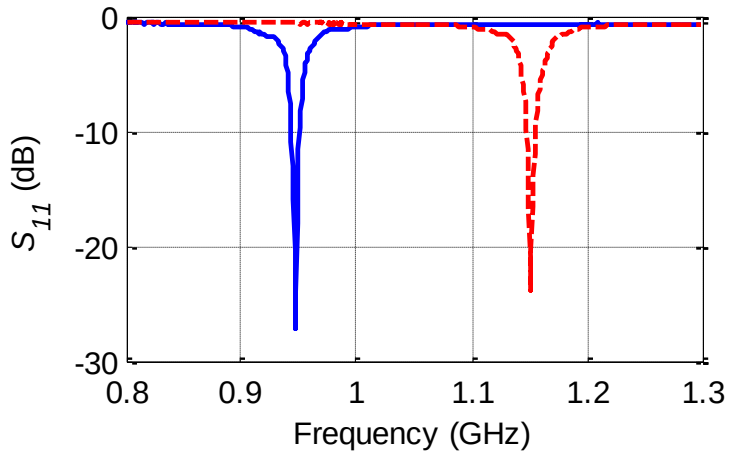


(b)

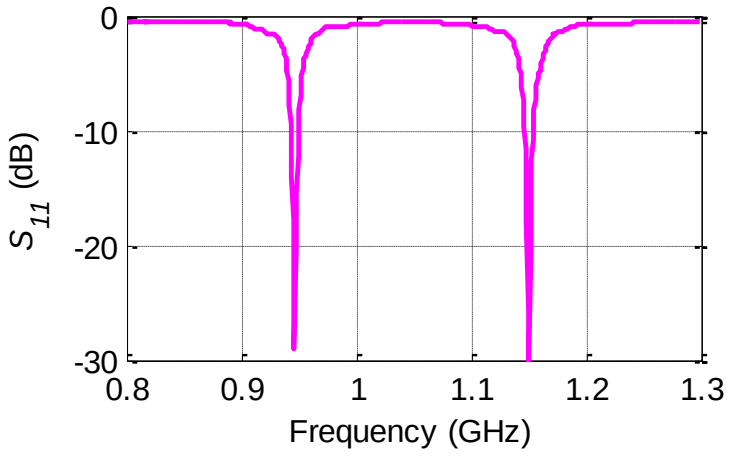


(c)

Figure 2.27: Response of an intrinsically switchable dual-frequency BST FBAR with (a) both resonators off, (b) each individual resonator on, and (c) both resonators simultaneously on.

The dual-frequency BST resonator can also exhibit both the low and high frequency resonances simultaneously by switching on both FBARs. This can be done by applying a bias voltage at the inner node, resulting in a voltage difference across the terminals of both FBARs. With the application of a 20 V dc bias, the dual-frequency response shown in Figure 2.27(c) is obtained. In this condition, the *Q*s for the series and parallel resonance of the low frequency resonator are 89 and 84, respectively, and the *Q*s for the series and parallel resonance of the high frequency resonator are 81 and 88, respectively. The reduction in the *Q*s of the resonances when both FBARs are switched on compared to when just a single device is switched on is attributed to the loss of energy from the excitation of evanescent acoustic waves in the other BST FBAR, which is designed for a different resonance frequency. The $K_{t,}^{2}{}_{eff}$s for the low and high frequency resonator are 2.8% and 2.4%, respectively. The reduction in $K_{t,}^{2}{}_{eff}$ of the resonators when both FBARs are switched on is attributed the smaller effective series capacitance of the other FBAR. The figures-of-merit of the characterized device is summarized in 2.6.

Table 2.6: Summary of Reconfigurable Dual-Frequency Resonator Performance

| Configuration | $f_s$ (GHz) | $f_p$ (GHz) | $Q_s$ | $Q_p$ | $K_{t,}^{2}{}_{eff}$ (%) | $K_{t,}^{2}{}_{eff,\ int}$ (%) |
|---|---|---|---|---|---|---|
| One on | 0.9361 | 0.9498 | 98 | 90 | 3.5 | 5.1 |
| One on | 1.136 | 1.153 | 100 | 99 | 3.6 | 5.0 |
| Both on | 0.9391 | 0.9498 | 89 | 84 | 2.8 | 5.1 |
| Both on | 1.141 | 1.153 | 81 | 88 | 2.4 | 5.0 |

The dual-frequency resonator demonstrated here shows the potential for using intrinsically switchable and tunable BST FBARs for designing reconfigurable multi-frequency resonators. For applications that require higher quality factors, a design similar

to the BST-on-Si composite FBARs in [29], which have demonstrated the highest quality factor BST FBARs to date, can be used. For applications that require higher $K_{t,}^{2}{}_{eff}$, higher bias voltages or BST thin films with higher τ can be used. The low and high frequency BST FBARs in this work had a $K_{t,}^{2}{}_{eff}$ of 5.1% and 5.0%, respectively, and a τ of 2.4. Furthermore, the use of multi-ferroelectric layer composite resonators [47, 48] and contour mode resonators [49] can be used to reduce the number of additional fabrication/processing steps necessary for realizing many more operating frequencies.

## 2.4. Conclusion

In this chapter, the theory of operation, design, fabrication, performance, and modeling of intrinsically switchable and tunable BST FBARs are presented. The voltage dependent behavior, RF power dependent behavior, and switching reliability of BST FBARs are discussed in detail. Furthermore, their application in the design of reconfigurable BST resonators is demonstrated.

DC bias voltage dependent measurement results of a BST FBAR show that without an applied dc bias, no electrical resonance is observed and with an applied dc bias, a series and parallel electrical resonance are exhibited. Furthermore, the resonance frequencies can be tuned by up to 5.33% by adjusting the bias voltage level. Large signal measurement results show that both quality factor ($Q$) and effective electromechanical coupling coefficient ($K_{t}^{2}{}_{eff}$) decrease at lower dc bias voltages as a function of RF power. However, the RF power dependence of $Q$ and $K_{t,}^{2}{}_{eff}$ is significantly reduced at higher bias voltages. Reliability testing of BST FBARs has also been performed. Devices that are switched on and off for over one billion cycles in an open-air environment do not show any signs of

performance degradation. A large signal nonlinear MBVD model that is able to represent the measured dc bias voltage and RF power dependent behavior of BST FBARs is also presented. When the modelling results are compared to the measurement results, excellent agreement is observed. Lastly, a reconfigurable dual-frequency resonator that consists of two series connected BST FBARs with *Q*s of 100 has been presented. It can be off, switched on and exhibit one of two resonances, or exhibit both resonances simultaneously. This is the first demonstration of BST-based frequency switchable devices for the design of adaptive and reconfigurable wireless devices.

# CHAPTER 3

# Design and Performance of Switchable, Tunable, and Reconfigurable BST FBAR Filters

## 3.1. Introduction

BAW resonators have been widely used for the design of bandpass filters for mobile wireless devices in the past decade. Their low insertion loss, high out-of-band rejection, small size, and large bandwidth have been are able to justify a price premium over conventional SAW filters and their market share is expected to continue to enjoy a strong demand into the future [50]. BAW resonators can be used in a wide variety of filter topologies. The two main categories of BAW filters are acoustically coupled and electrically coupled filters. Acoustically coupled filters consist of several resonators of the same frequency placed in very close proximity of one another such that the acoustic waves from each resonator are able to couple and cause the resonance mode to split [51]. They can either be coupled by being vertically stacked on top of one another or being places in very close lateral proximity to one another. Electrically coupled filters consist of multiple resonators that are connected electrically in series and in parallel and are traditionally configured in either a ladder or lattice topology, as described in [26]. The advantage of acoustically coupled filters is their very small feed through capacitance between the two ports of the filter, which results in a very high out of band rejection [26]. The advantage of

electrically coupled filters is their straightforward design process, which can be easily performed using circuit based simulators, and their commercial success, which has fueled continued research into the field [26]. In this chapter, intrinsically switchable and tunable ferroelectric FBAR are used to design electrically coupled filters that use the ladder configuration as well as reconfigurable ferroelectric FBAR filters.

## 3.2. Design, Modeling, and Simulation

Electrically coupled ladder filters consist of an arrangement of alternating series and shunt resonators as shown in Figure 3.1(a). The shunt resonators are designed to have resonance frequencies lower than the series resonator such that the parallel resonance frequency of the shunt resonators are approximately the same as the series resonance frequency of the series resonators, which results in the filter response shown in Figure 3.1(b). At frequencies far below the series resonance frequency of the shunt resonator ($f << f_{s2}$), the static capacitance of both resonators dominate the behavior of the filter and the out-of-band rejection is determined by the capacitance ratio between the series and shunt resonators [26]. At frequencies near the series resonance frequency of the shunt resonator ($f \sim f_{s2}$), the signal fed at the input is shunted to ground by the low impedance of the shunt resonator and a notch occurs below the center frequency of the filter response. At frequencies near the parallel resonance frequency of the shunt resonators ($f \sim f_{p2}$) and the series resonance frequency of the series resonators ($f \sim f_{s1}$), the signal sees a very large impedance to ground and a very small impedance to the output and therefore, most of the signal is transmitted from the input to the output. At frequencies near the parallel resonance frequency of the series resonator ($f \sim f_{p1}$), the signal sees a large impedance to the output

and is mostly reflected back to the input and a notch occurs above the center frequency of the filter response. At frequencies much higher than the parallel resonance of the series resonator ($f >> f_{p1}$), the capacitance of the resonators appear as very small impedances and again, the ratio of the capacitances between the series and shunt resonators determine the out-of-band rejection.

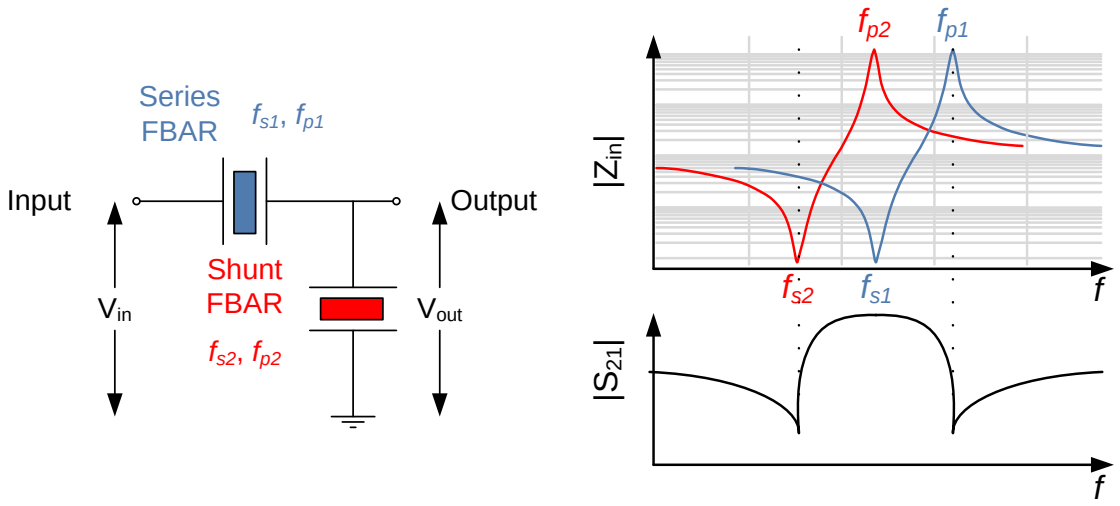


(a) (b)

Figure 3.1: (a) Schematic of a single stage electrically coupled ladder filter. (b) Synthesis of the bandpass filter response from the input impedance of the series and shut FBARs.

The performance of FBAR filters can be fine-tuned by using a variety of techniques. First, the number of stages (pair of series and shunt resonators) can be increased to obtain higher out-of-band rejection. Second, the resonators that make up the filter can be designed to have higher quality factors ($Q$s) at the price of lower effective electromechanical coupling coefficients ($K_t^2{}_{eff}$) to achieve a smaller bandwidth. Third, the series and parallel resonance frequencies of individual series and shunt resonators can be slightly tuned by adding compensation/mass loading layers or inductors. Many of these techniques are used in the design of commercially available aluminum nitride based FBAR and SMR filters

[26]. However, here the focus is to study the switching and tuning behavior of ferroelectric FBAR filters. Therefore, a simple 1.5 stage ladder filter has been designed to test the performance of ferroelectric-based FBAR filters.

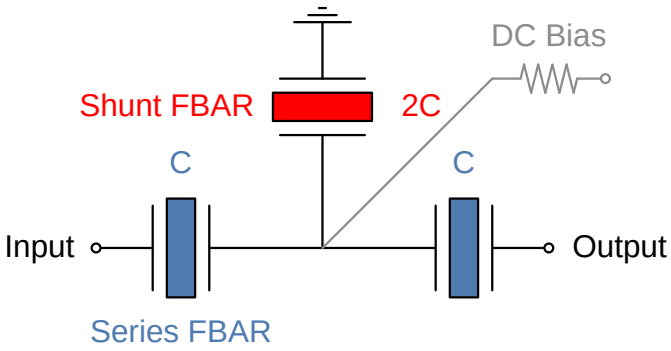


Figure 3.2: The schematic of an intrinsically switchable 1.5 stage ferroelectric FBAR filter.

Ferroelectric FBAR filters are designed by implementing the extracted MBVD model of measured ferroelectric FBARs or by creating an MBVD model (shown in Figure 3.3) based on desired filter characteristics in a circuit simulator such as Advanced Design System (ADS). The MBVD model parameter extraction procedure was given in Chapter 2. Here the focus is on creating an MBVD model to obtain the desired filter response and then designing a resonator that matches the MBVD model. The different MBVD model parameters can be related to the resonator characteristics by using the following equations [52]:

$$L_m = \frac{1}{(2\pi f_s)^2 C_m} \tag{3.1}$$

$$C_m = C_{cap} \cdot 2 \cdot BWR \tag{3.2}$$

$$R_m = \frac{2\pi f_s \cdot L_m}{Q_s} \tag{3.3}$$

$$C_0 = \frac{2C_{cap}}{2 + BWR} \tag{3.4}$$

$$R_0 = \frac{Q_d}{2\pi f_s C_0} \tag{3.5}$$

$$BWR = \frac{f_p - f_s}{f_p} \tag{3.6}$$

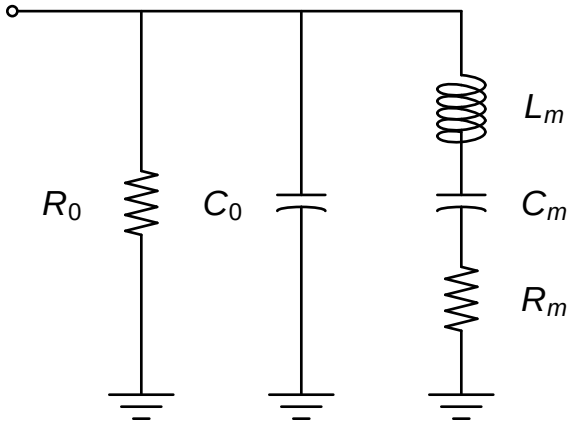


Figure 3.3: Simple MBVD model used for designing FBAR filters.

The parameters in these equations are the series resonance frequency ($f_s$), parallel resonance frequency ($f_p$), series resonance frequency quality factor ($Q_s$), dielectric quality factor ($Q_d$), device capacitance ($C_{cap}$), and bandwidth ratio ($BWR$). Once the desired filter response is obtained through the circuit simulation, the acoustic wave transmission line model can be used to design the thickness of each layer of material and the capacitance of the resonator. If the required resonator is not feasible, then the filter needs to be redesigned based on more practical FBAR figures of merit.

The schematic of the 1.5 stage filter that consists of two series FBARs and two shunt FBARs is shown in Figure 3.2. The dc bias for switching the resonators on and off is applied to the center node of the filter through a thin film resistor while all other nodes are

held at dc ground with the use of the bias tees at both ports. The thin film resistors should have a resistance that is large enough to prevent RF signals from leaking onto the dc port and increasing the insertion loss as well as small enough such that the switching/response time due to RC delay is insignificant and furthermore that any leakage current of the ferroelectric resonators does not cause a significant voltage drop across the thin film resistor, which would reduce the voltage and therefore electric field seen by the resonator [53]. It should be noted that by using this configuration, it is also possible to dynamically tune performance of the overall filter by changing dc bias across individual resonators. However, this is not investigated here.

## 3.3. Fabrication and Measurement Procedure

The fabrication procedure for ferroelectric FBAR filters is very similar to that of stand-alone ferroelectric FBARs. However, there are a few additional steps that are that are also needed. Figure 3.4 summarizes the fabrication procedures. The key differences in the fabrication process are shown in Figure 3.4(f), where a thin layer of gold is deposited on the top electrode of the shunt resonator to serve as a mass loading/compensation layer and shift its resonance frequencies down, and in Figure 3.4(g), where a thin layer of high resistivity material such as SiCr, chromium, nickel-chromium, and even platinum is use to create thin film resistors. Microphotographs of two different ferroelectric FBAR filters are shown in Figure 3.4. The filter in Figure 3.5(a) has been designed for top-side releasing with XeF2 gas and the filter in Figure 3.5(b) has been design for back-side releasing by DRIE [Figure 3.4(i)].

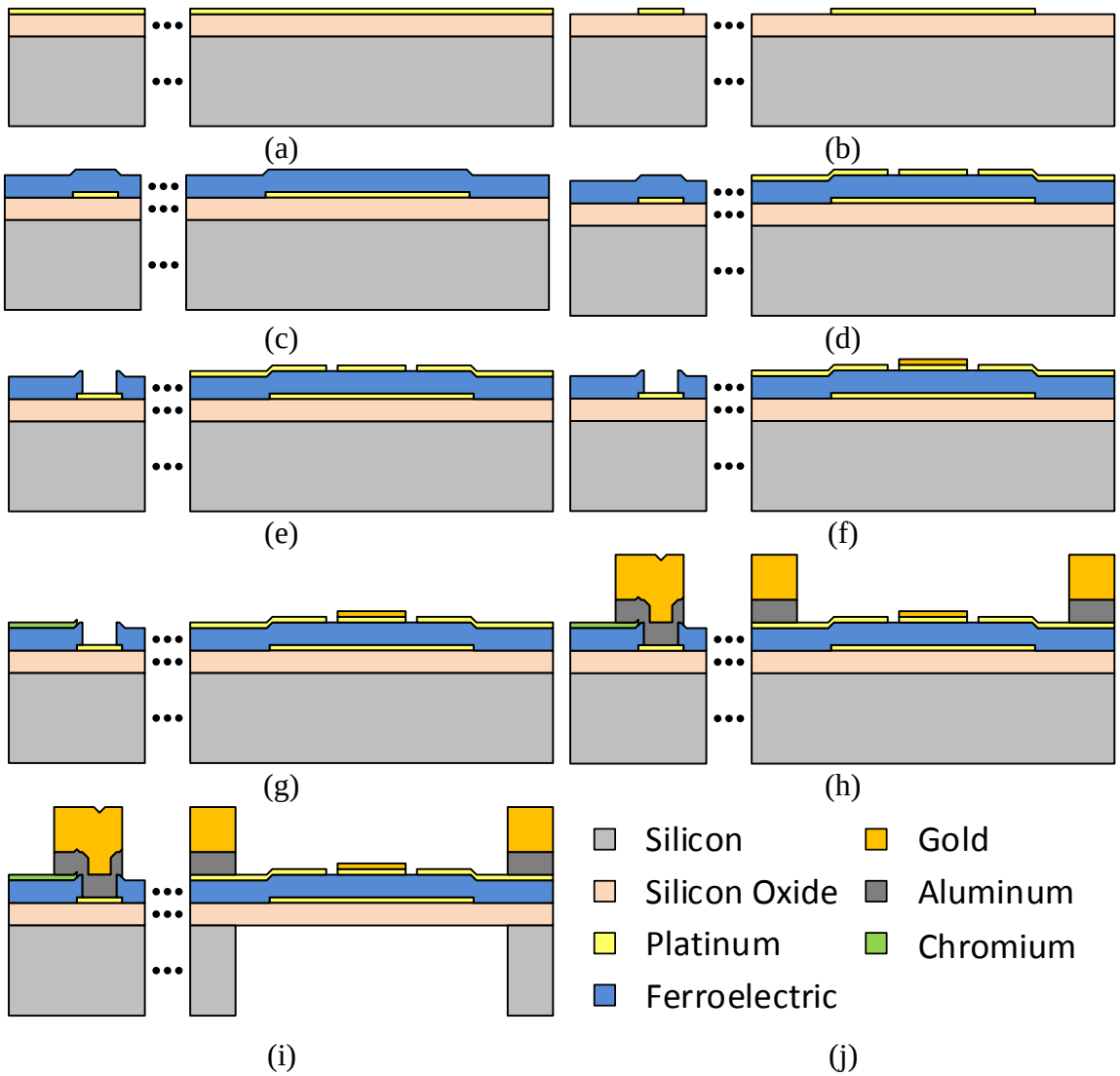


Figure 3.4: Fabrication procedure for ferroelectric FBAR filters. (a) A high resistivity silicon wafer with a thermally grown oxide layer and a 150 nm layer of platinum with 40 nm of TiO2 adhesion layer is cut to the desired size. (b) Bottom electrodes are defined by using ion milling to selectively etch away platinum. (c) Ferroelectric thin film is deposited. (d) Top electrodes are deposited. (e) The ferroelectric is selectively etched away using HF/BHF. (f) A gold mass loading/compensation layer is deposited on top of the top electrode of the shunt resonator. (g) Thin film resistor is deposited. (h) Gold and aluminum contacts are deposited. (i) The silicon beneath the device is etched. (j) The key labeling the different materials used in the fabrication process.

The performance of two different types of ferroelectric FBAR filters are discussed in the next section. The first filter has a 1 μm layer of SiO2 under the bottom electrode and has a 700 nm thin film of BTO as the ferroelectric transduction layer. Since BTO is in the

ferroelectric phase at room temperature, it possesses a spontaneous polarization and therefore, BTO resonators can exhibit an electrical resonance even in the absence of an applied dc bias voltage. The BTO FBAR filter has two shunt resonators in parallel instead of just one to compliment the symmetry of the CPWs used for characterizing the device as can be seen in Figure 3.5(a). The second filter has a 10 μm layer of Si under the bottom electrode and has a 550 nm thin film of BST as the transduction layer. BST is in the paralelectric phase at room temperature and should behave as a capacitor with dc bias. The filter just has one shunt resonator as can be seen in Figure 3.5(b).

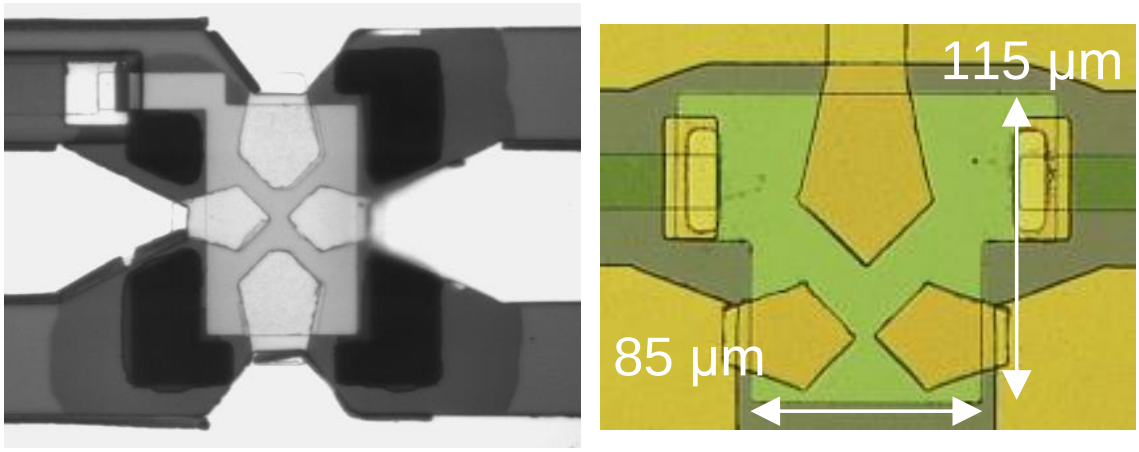

Figure 3.5: Microphotographs of a fabricated 1.5 stage electrically coupled ladder filter.

The fabricated filters are measured on a Cascade Microtech probe station with two 150 μm pitch GSG probes. S-parameters are acquired using an Agilent E8364B/C network analyzer after performing a SOLT calibration. The dc bias is controlled with an Agilent E3631A dc power supply and applied through bias tees and a dc probe.

## 3.4. Filter Performance

### 3.4.1. Voltage dependent behavior

The voltage dependent performance and switching behavior of several different ferroelectric FBAR filters that have been fabricated are reported here. The measurement results of the BTO FBAR filter shown in Figure 3.5(a) in the on and off state are giving in Figure 3.6. With the application of a -3 V dc bias, the filter is off and the two ports are isolated by 15 dB and the return loss at each port is 1.6 dB as shown in Figure 3.6(a). With the application of a 15 V dc bias, a bandpass response at 2.14 GHz is observed with a 3 dB bandwidth of 33 MHz as shown in Figure 3.6(b). The filter has an insertion loss in the passband of 6.5 dB, return loss greater than 10 dB for both ports, and out-of-band rejection of 19 dB.

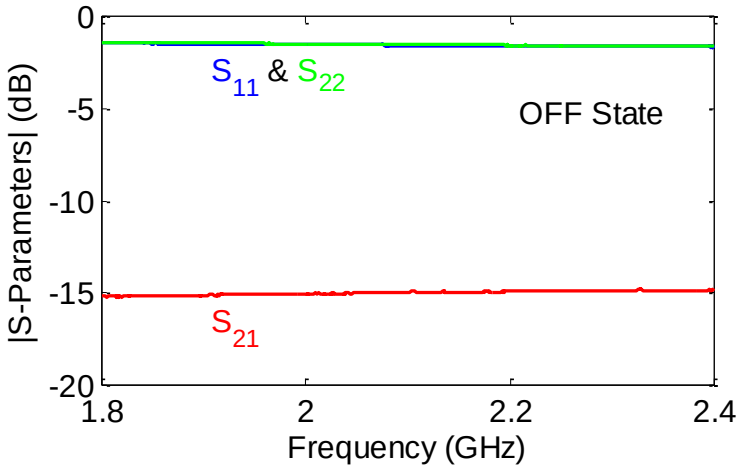


(a)

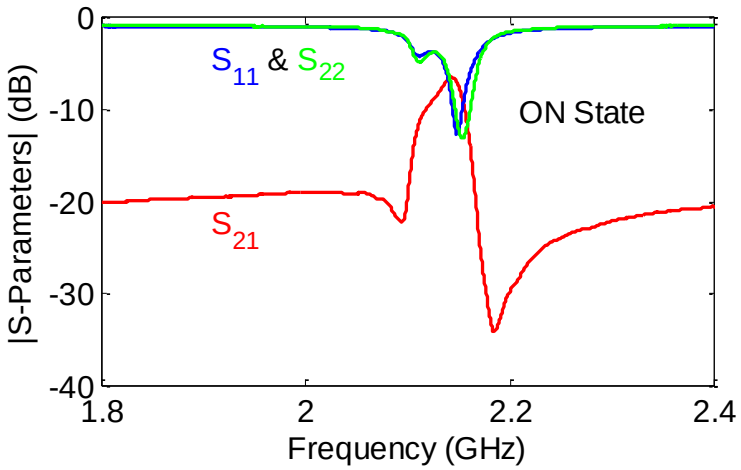


(b)

Figure 3.6: Response of a BTO FBAR filter in the on and off state.

The response of the filter can also be adjusted dynamically by tuning the dc bias voltage. Figure 3.6 shows the transmission and reflection coefficients of the filter as the bias voltage is increased from -3 to 15 V in increments of 3 V. Here, we see that even at 0 V, there is a filter response since the resonators are switched on due to the spontaneous polarization present in the BTO thin film. As the bias is increased, the effective

electromechanical coupling coefficient of the resonators increase, resulting in a higher return loss and lower insertion loss, as summarized in Table 3.1.

Table 3.1:
Measured Filter Characteristic at Various DC Bias Voltages

| DC Bias Voltage (V) | Return Loss (dB) | Insertion Loss (dB) |
|---|---|---|
| 0 | 4.7 | 13.4 |
| 3 | 9.9 | 10.8 |
| 6 | 12.7 | 8.7 |
| 9 | 13.2 | 7.5 |
| 12 | 13 | 6.8 |
| 15 | 12.8 | 6.5 |

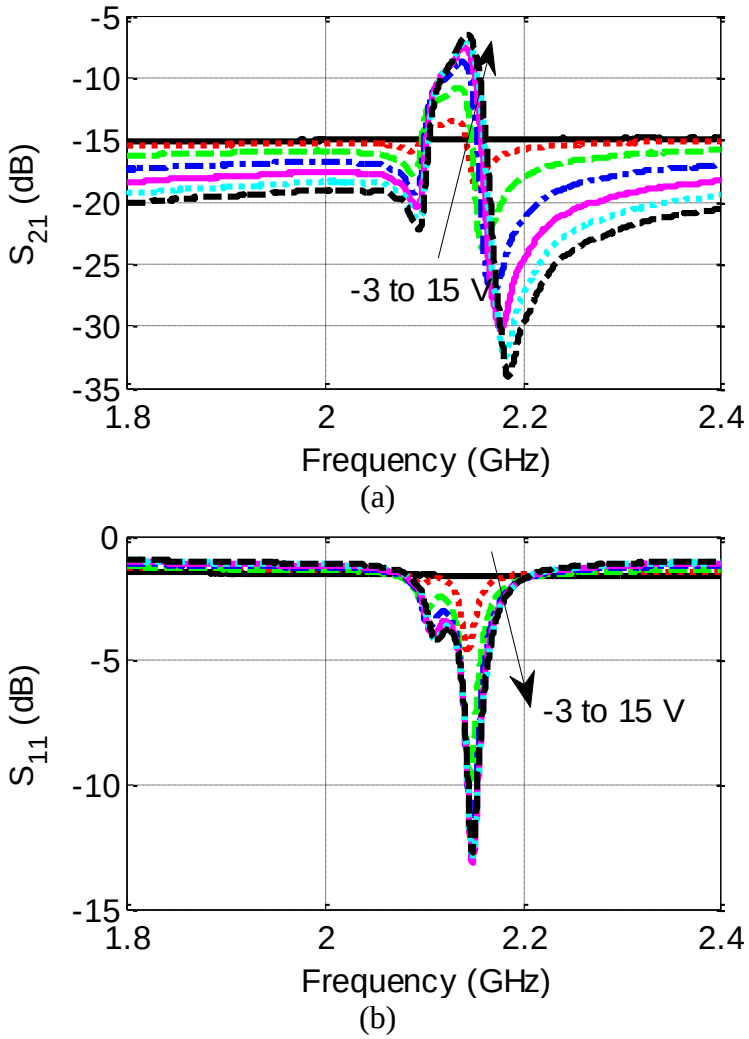


Figure 3.7: Measured BTO FBAR filter response at dc bias voltages of -3, 0, 3, 6, 9,12, and 15 V.

Voltage dependent measurement results of the 1.5 stage electrically coupled BST-FBAR-based ladder filter shown in Figure 3.5(b) are given in Figure 3.8. The solid black trace shows the transmission and reflection coefficient of the filter when in the off state, which occurs at a dc bias voltage of 0 V since BST is in its paraelectric state at room temperature and does not exhibit spontaneous polarization. When switched off, the devices has a return loss of 1 dB and an isolation of 14 dB. As the dc bias voltage is increased, a passband response emerges, the return loss increases, the insertion loss decreases, and the

center frequency is tuned. At 20 V dc bias, the filter has a center frequency of 1.60 GHz, bandwidth of 9 MHz, insertion loss of 4.1 dB, and a return loss exceeding 10 dB. The center frequency of the filter under different dc biasing is given in Table 3.2. A summary of the measurement results for both types of intrinsically switchable BST filters is given in Table 3.3.

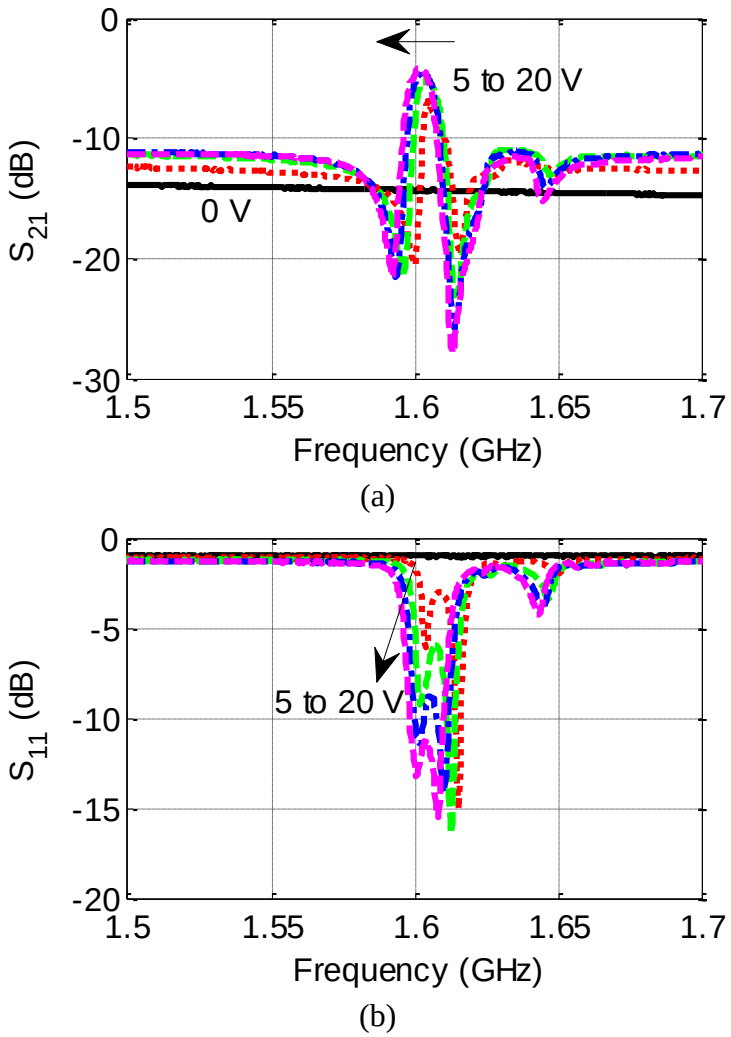


Figure 3.8: (a) Transmission coefficient and (b) reflection coefficient of a 1.5 stage electrically coupled bandpass ladder filter composed of BST at dc bias voltages of 0, 5, 10, 15, and 20 V.

Table 3.2:
Center Frequency of BST FBAR Filter

| DC Bias Voltage (V) | Center Frequency (GHz) |
|---|---|
| 5 | 1.604 |
| 10 | 1.604 |
| 15 | 1.603 |
| 20 | 1.601 |

Table 3.3: Summary of Filter Performance

| | BTO Filter | BST Filter |
|---|---|---|
| Off Bias Voltage | -3 V | 0 V |
| On Bias Voltage | 15 V | 20 V |
| Center Frequency | 2.14 GHz | 1.60 GHz |
| Bandwidth | 33 MHz | 9 MHz |
| Insertion Loss | 6.5 dB | 4.1 dB |
| Return Loss | >10 dB | >10 dB |
| Isolation | 15 dB | 14 dB |

From these results, it can be concluded that BST FBAR filters can be switched on and off and their insertion loss can be dynamically adjusted by controlling the bias voltage level. Furthermore, the center frequency of the filters can also be tuned.

### 3.4.2. Switching reliability and response time

Several FBAR filters are tested for switching reliability and performance degradation using the setup shown in Figure 3.9, which is similar to that used for measuring the reliability of BST FBARs. The network analyzer is set to the center frequency of the band pass response and 10 dBm of power is delivered to the input of the filter. The insertion loss and isolation of the filter, when switched on and off, respectively, are measured to monitor its performance degradation after a given number of switching cycles. The measurement results plotted in Figure 3.10 show that the performance of the filter in both the on and off state did not change after cycling the device one billion times. The reliability and stability

of the BST FBAR filters tested in this work demonstrate that these devices may be acceptable for use in tunable and switchable RF circuit designs for commercial/industrial applications.

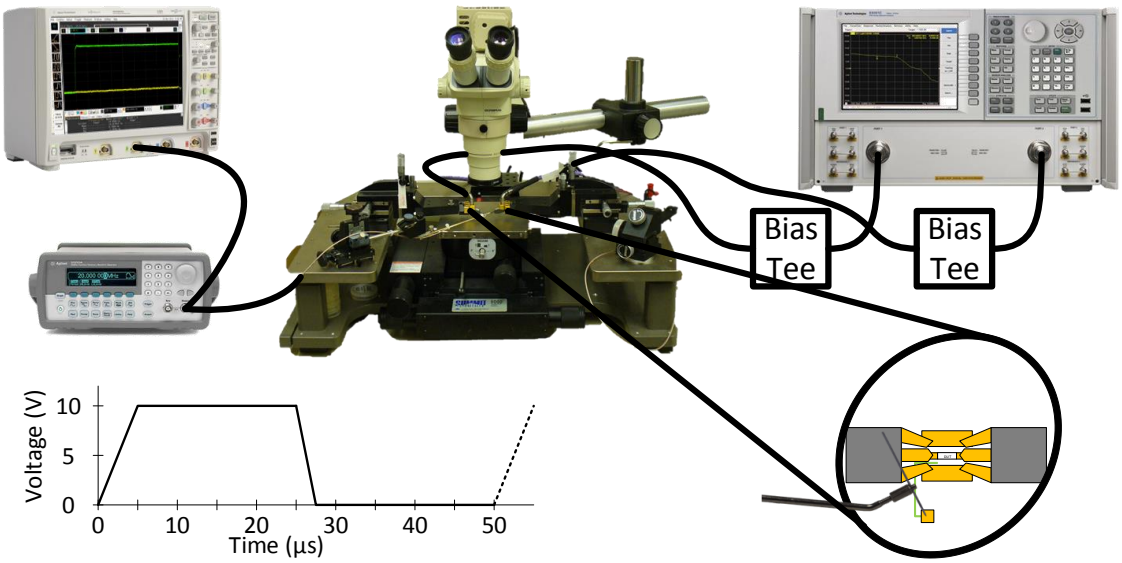


Figure 3.9: Measurement setup for measuring the reliability and switching speed of intrinsically switchable BST FBAR filters. Biasing is performed through a dc probe that is used to make contact with the thin film resistor that has been fabricated on chip.

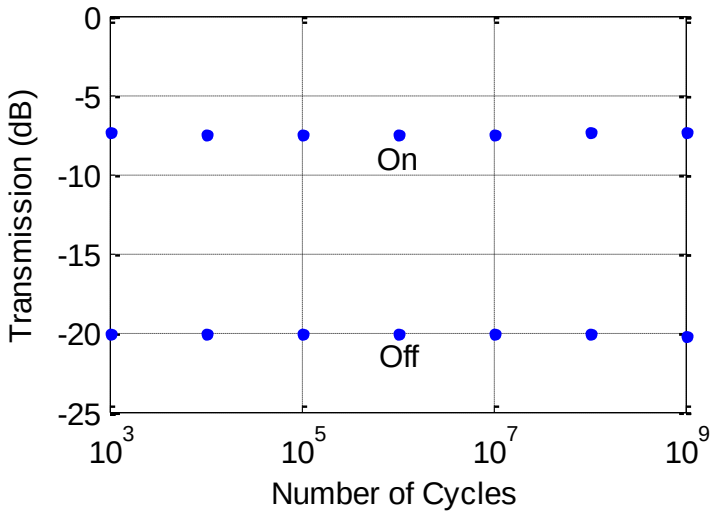


Figure 3.10: Measured transmission at the center frequency of an intrinsically switchable BST FBAR filter after the indicated number of switching cycles when switched 'On' and 'Off'.

Switching speed measurements have also been performed on a BST FBAR filter using the setup shown in Figure 3.11. For this measurement, a 4 dBm continuous wave signal with a frequency of 1.526 GHz, which is the center frequency of the BST FBAR filter under test, is fed into its input. The signal at the output of the device is measured using an Agilent MSO9404A Mixed Signal Oscilloscope as the filter is switched on and off by using an arbitrary wave form generator that provides a 1 kHz pulse wave with a 10 V amplitude and a duty cycle of 0.5 %. Figure 3.12 shows the waveform at the output of the arbitrary waveform generator (yellow trace) and the output of the filter (green trace). The output of the arbitrary waveform generator provides a pulse with a very fast rise and fall time, but it also shows some ringing, which has a frequency of 1.3 MHz and is due to the probe tip that is used for applying the dc bias to the filter. Nevertheless, even with the ringing in the dc biasing, the signal at the output of the filter demonstrates that intrinsically switchable ferroelectric based resonators and filters exhibit a switching speed of less than 100 ns. This is much faster than the switching speed of MEMS switches, which is on the order of 30 μs [54].

With a more sophisticated measurement setup, it is believed that the measured switching speed would be much faster that what has been demonstrated here. The lower limit is expected to be determined by the time it takes to setup a standing acoustic wave within the resonator body. Therefore, the lower limit of the switching speed can be calculated from the amount of time it takes for the excited acoustic waves to travel through the top electrode, ferroelectric thin film, and bottom electrode layers of the FBAR structure and back. Assuming that the top and bottom platinum electrodes are each 100 nm thick and

the ferroelectric thin film is 500 nm thick, and based on longitudinal acoustic wave velocities of 2767 m/s and 6192 m/s for platinum and the ferroelectric, respectively, the lower limit of the response time for the 3 GHz resonator is calculated to be roughly 300 ps. Furthermore, as the resonator is made thinner to achieve a higher resonance frequency, the response time is also expected to decrease, due to their inverse relationship.

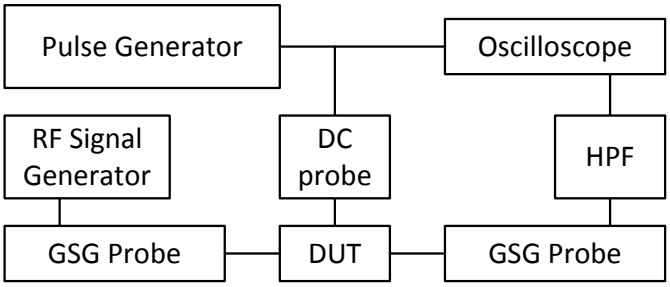

Figure 3.11: Measurement setup for testing the switching speed of BST FBAR filters.

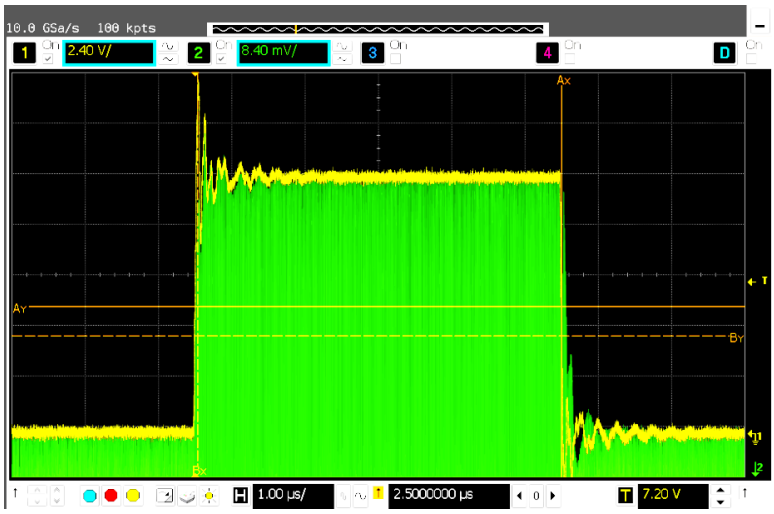


(a)

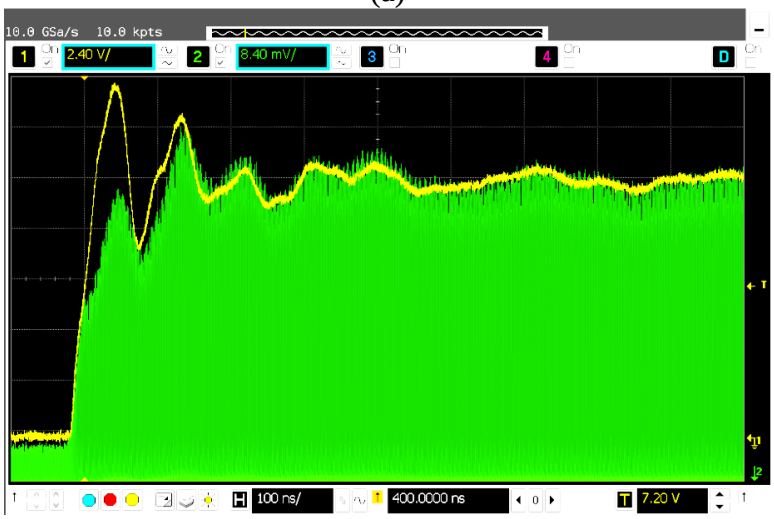


(b)

Figure 3.12: Oscilloscope waveform measuring the output of the arbitrary waveform generator and the output of the BST FBAR filter when switched on with a horizontal scale of (a) 1 µs/division and (b) 100 ns/division.

## 3.5. Dual-Band BST Filter

### 3.5.1. Design

Intrinsically switchable BST FBAR filters of different frequencies are connected in parallel with one another to form multi-band filters. Each individual intrinsically switchable BST filter consists of an electrically coupled 1.5 stage ladder filter placed in

between series connected BST MFM varactors as shown in Figure 3.13. The purpose of using the BST varactors is to improve the isolation of the filter without significantly impacting insertion loss or adding to fabrication complexity and device area.

The intrinsically switchable and tunable filter operates as follows. When it is switched on, the three resonators are switched on and the varactors are tuned to their highest capacitance such that they are at their lowest impedance, which occurs when the voltage across their terminals is 0 $V_{DC}$. When the filter is switched off, the shunt resonator is switched off and the varactors are set to their lowest capacitance such that they present a high impedance, which occurs when the voltage across their terminals is high.

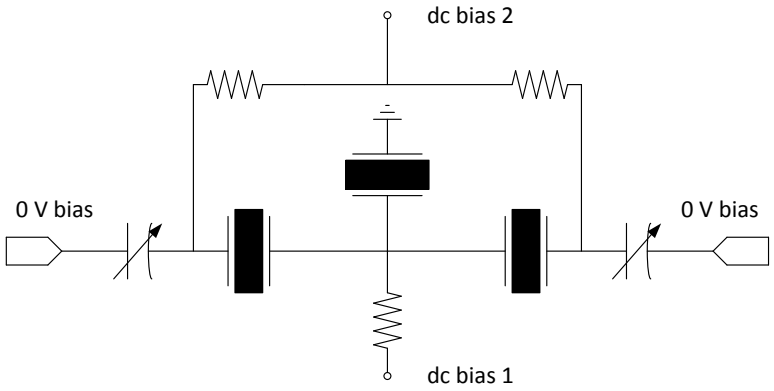

Figure 3.13: Schematic of a 1.5 stage BST FBAR filter with series BST varactors.

A comparison between the multi-band filter design discussed in the previous paragraph (shown in Figure 3.14(a)) and the same filter but without the series connected BST varactors (shown in Figure 3.14(b)) is performed through simulation to study the performance improvement obtained by using the varactors. Figure 3.15 shows the S-parameters of reconfigurable dual-band filters that consists of the exact same FBARs but with (red solid trace) and without (blue dashed trace) series varactors. From the results, it is concluded that the series BST varactors can greatly improve the matching and rejection

ratio of the filter. This is in part due to the additional impedance of the series varactor but mostly due to the ability to independently switch on the series and shunt resonators, which significantly helps reject the out-of-band signals. Furthermore, the biasing scheme provides a notch near the center frequency of the off filter, which is beneficial for many applications such as frequency-division multiplexing. In summary, the increase in complexity of the dc biasing scheme due to the added series BST varactors is justified by the improvement in performance. In this work, we demonstrate a dual-band filter, which has the configuration shown in Figure 3.14(a).

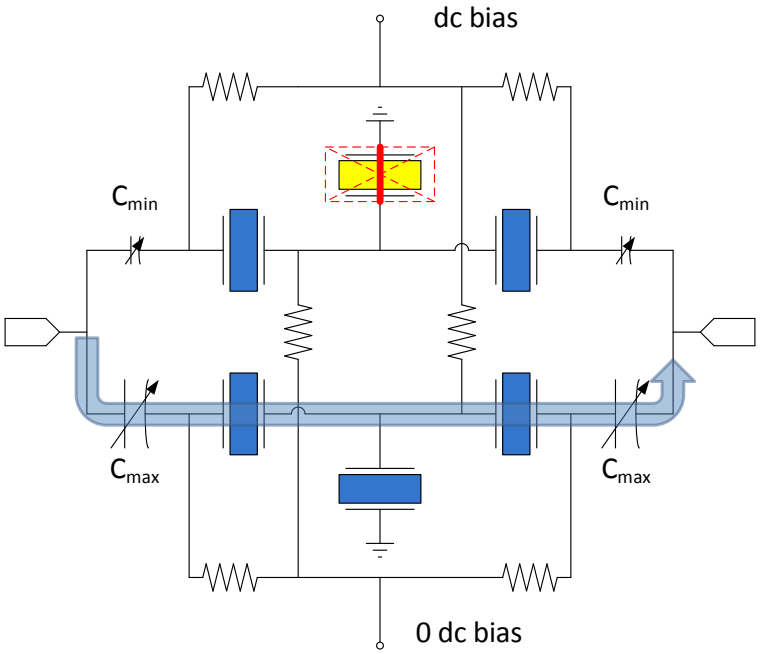


(a)

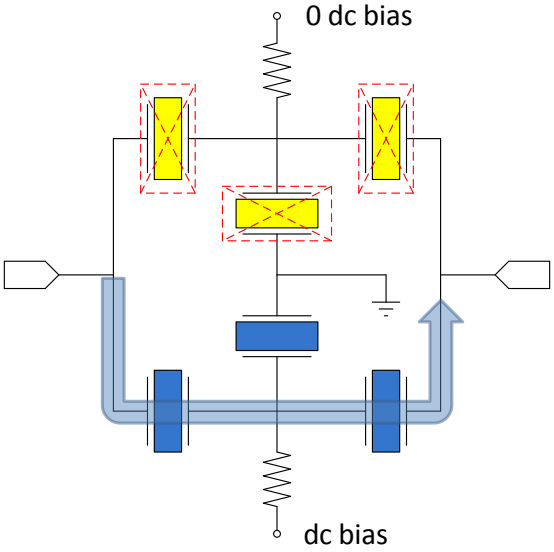


(b)

Figure 3.14: Schematic of a dual-band BST FBAR filter (a) with series connected BST varactors and (b) without series connected BST varactors. The biasing configuration for turning on a single filter is shown where the blue resonators are switched on and the yellow resonators are switched off. The arrow indicates the path of the RF signal within in the pass band of the filter.

The dual-band BST filter designed in this work consists of series resonators with an area of 32 μm × 37.5 μm and shunt resonators with an area of 60 μm × 40 μm for both filters, which results in a capacitance ratio of 1:2. The series BST varactor has an area of 30 μm × 40 μm and has the same capacitance as the series resonators. All of the resonators in the low frequency filter have a thicker top electrodes to shift their resonance frequency lower. In addition, the shunt resonators in both filters have a thicker top electrode to shift their frequency down and get the desired bandpass response. The fabrication process is discussed in more detail in the next section.

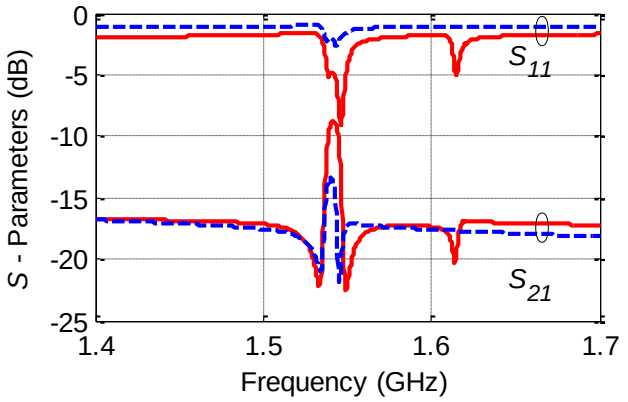


(a)

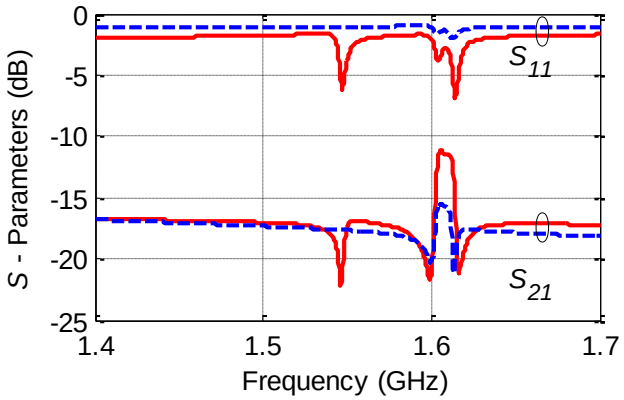


(b)

Figure 3.15: *S*-parameters of a simulated dual-band filter with (red solid trace) and without (blue dashed trace) the use of series BST varactors. (a) The low frequency filter is switched on while the high frequency filter is switched off. (b) The low frequency filter is switched on while the high frequency filter is switched off.

### 3.5.2. Fabrication and Measurement Setup

Multi-band BST FBAR filters are fabricated using a very similar procedure as described for individual BST FBAR filters. The only difference is the need for additional mass loading/compensation layers to offset the frequency of the two filters. A microphotograph of a fabricated device is shown in Figure 3.16. The measurement setup for characterizing the dc bias voltage dependent behavior of reconfigurable BST FBAR filters is also the same as with individual filters.

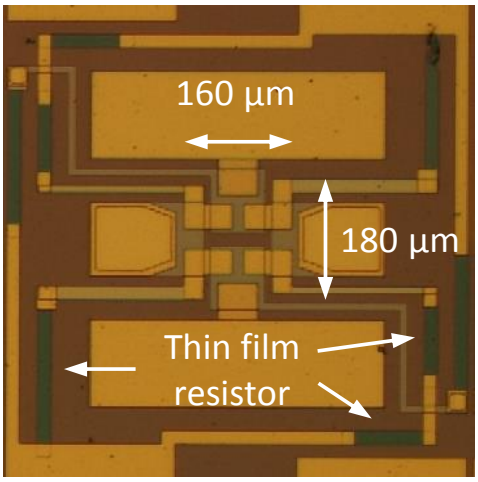


Figure 3.16: Microphotograph of a fabricated dual-band BST FBAR filter.

### 3.5.3. Performance

The dual-band BST filter with the design shown in Figure 3.14(a) has been characterized under various biasing conditions. The bias voltage at the port is applied through a bias-tee and is maintained at 0 V and the bias voltage at the two inner nodes are applied through dc probes. In the case both filters are off, the return loss is 0.7 dB and the

rejection is greater than 20 dB over a frequency range of 1.4 to 1.7 GHz, as shown in Figure 3.17(a). In the case the low frequency filter is switched on with a 20 V dc bias, a bandpass response with a center frequency of 1.541 GHz, insertion loss of 8.8 dB, and bandwidth of 7 MHz is obtained, as shown in Figure 3.17(b). In the case the high frequency filter is switched on with a 20 V dc bias, a bandpass response with a center frequency of 1.608 GHz, insertion loss of 9.2 dB, and bandwidth of 9 MHz is obtained, as shown in Figure 3.17(c).

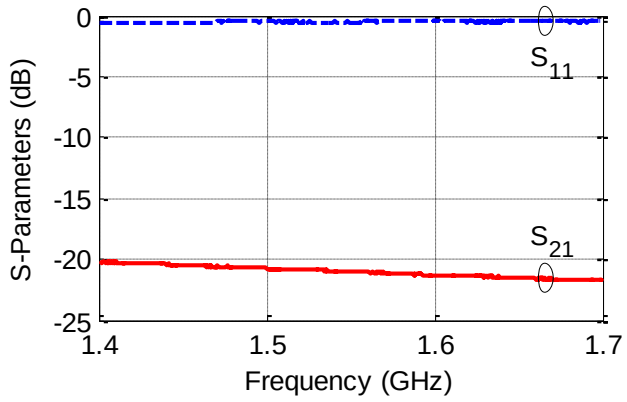


(a)

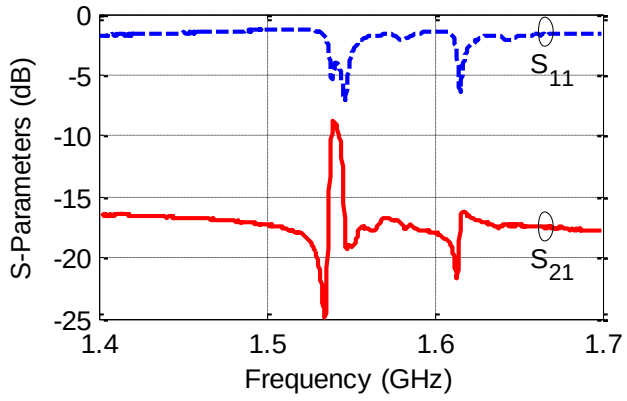


(b)

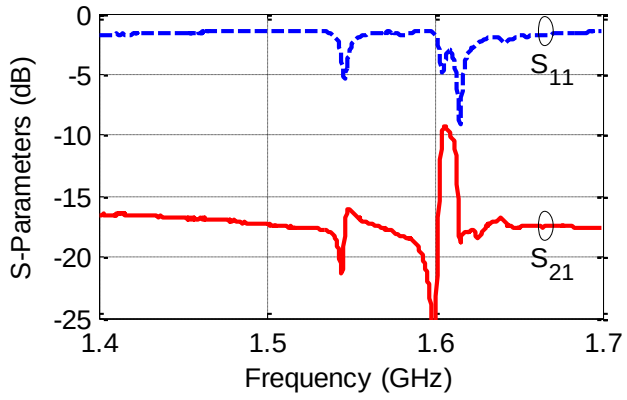


(c)

Figure 3.17: Measured reflection and transmission coefficients of a reconfigurable dual-band filter when (a) both filters are off, (b) one filter is on, and (c) the other filter is on.

The performance of the measured dual-band filter can also be improved by changing the port impedance to 20 Ω and adding 3 nH inductors in shunt at both ports as shown in the schematic in Figure 3.18 by using the software package Advanced Design System [55].

With this setup, the insertion loss decreases to a value of 6.5 dB and 6.2 dB for the low and high frequency filter response, respectively, as shown in Figure 3.19. The figures-of-merit of the dual-band filter demonstrated here are summarized in Table 3.4. The performance of the reconfigurable filter can be further improved by using similar techniques that were discussed for the reconfigurable BST resonator.

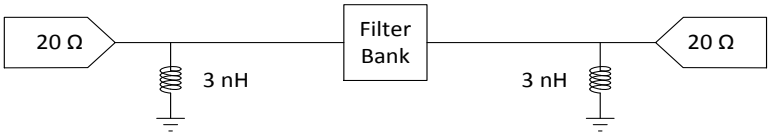


Figure 3.18: Schematic showing the impedance matching that is performed on the measured filter in simulation through the use of Advanced Design System.

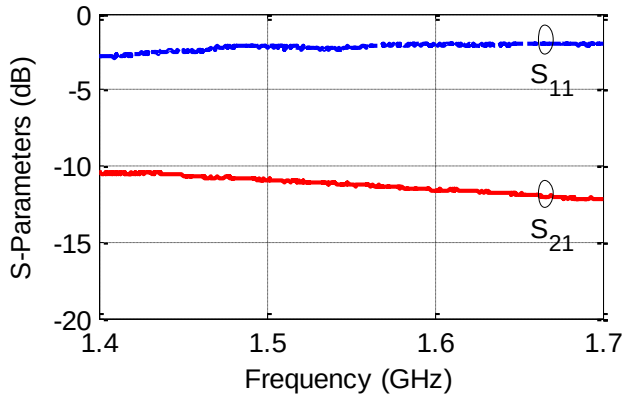


(a)

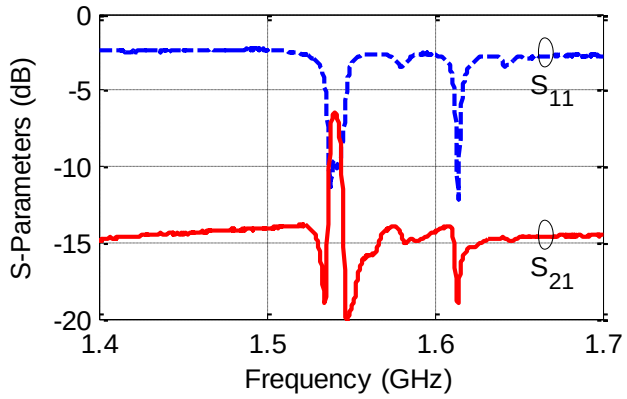


(b)

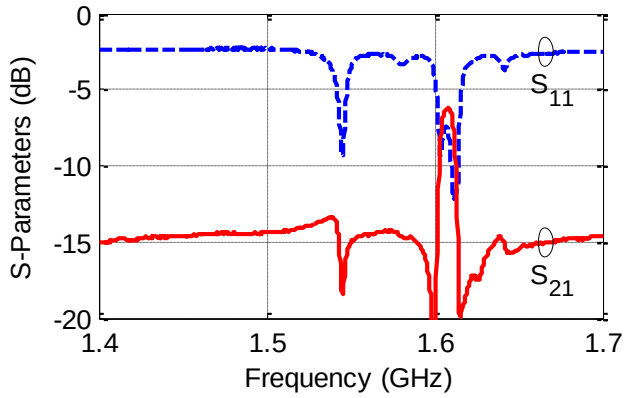


(c)

Figure 3.19: Simulated reflection and transmission coefficients of the measured reconfigurable dual-band filter when (a) both filters are off, (b) the low frequency filter is on, and (c) the high frequency filter is on for port impedances of 20 Ω and the addition of 3 nH shunt inductors.

Table 3.4:
Summary of Dual-Band Filter Performance

| | Low Frequency Filter | | High Frequency Filter | |
|---|---|---|---|---|
| | Without Matching Network | With Matching Network | Without Matching Network | With Matching Network |
| Center Frequency | 1.541 GHz | 1.541 GHz | 1.608 GHz | 1.608 GHz |
| Bandwidth | 7 MHz | 7 MHz | 9 MHz | 9 MHz |
| Insertion Loss | 8.8 dB | 6.5 dB | 9.2 dB | 6.2 dB |
| Return Loss | >4.0 dB | > 8.9 dB | >3.6 dB | >7.3 dB |
| Rejection | >16 dB | >13.5 dB | >16 dB | >13 dB |
| Isolation | >20 dB | >10 dB | >20 dB | >10 dB |

## 3.6. Conclusion

The theory of operation, design, fabrication, and performance of several ferroelectric thin film FBAR filters based on the electrically coupled ladder topology have been presented. The voltage controlled switching and tuning behavior of both BTO and BST based filters that work in the 1.5 – 2.5 GHz range are discussed. Ferroelectric FBAR filters are demonstrated to have very high switching reliability and a switching speed of less than 100 ns. Furthermore, a reconfigurable BST FBAR filter that utilizes BST varactors has been demonstrated for the very first time. The advantage of these devices is the elimination of dedicated switches that can be an additional source of signal loss, their excellent reliability due to their electrostriction based switching mechanism, and their very fast switching and response time.

# CHAPTER 4

# Design and Performance of BTO Contour Mode Resonators

## 4.1. Introduction

The intrinsically switchable film bulk acoustic wave resonators (FBARs) and solidly mounted resonators (SMRs) based on ferroelectric thin film technology that have been demonstrated in [56-59] rely on the controlled thickness of each layer in the device stack for obtaining the desired resonance frequencies, as discussed in Chapter 2. Intrinsically switchable bandpass filters, formed by arranging multiple ferroelectric FBARs in a ladder configuration have also been demonstrated in [60, 61], as discussed in Chapter 3. By using an array of such resonators and filters, intrinsically switchable resonator banks and filter banks can be demonstrated. However, as mentioned above, the resonance frequencies of FBARs are determined by the thickness of their structure. Therefore, for each operating frequency, a unique film thickness is required, increasing the number of processing steps, complexity, and overall cost of the device. One approach to address this issue is to use contour mode resonators in addition to FBARs.

Lateral (contour) mode resonators have their resonance frequency dictated by the lateral dimensions of the transduction layer and the geometry of their bottom and top electrodes. The advantage of contour mode resonators is that their frequency determining

design parameters of an individual device can be defined lithographically with the use of CMOS and MEMS fabrication techniques and therefore a limitless number of different resonance frequencies can be realized without increasing the number of processing steps. This is very beneficial for the design of monolithic, multi-frequency circuits [62]

In this chapter, 1-port intrinsically switchable contour mode resonators that have a barium titanate ($BaTiO_3$, BTO) thin film transduction layer are discussed. BTO is ferroelectric at room temperature and is utilized for its non-zero effective $d_{31}$ piezoelectric coefficient when polarized by an external electric field. This property allows the excitation of laterally propagating acoustic waves within the acoustically resonant cavity with the application of an RF signal applied across the top and bottom electrodes as shown in Figure 4.1. Here, two different electrode variations are used to excite the fundamental and higher order resonance modes as discussed in the following sections.

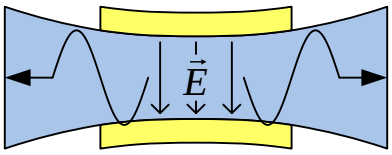


Figure 4.1: Cross section of a contour mode resonator that shows the excitation of laterally propagating acoustic waves due to the application of a vertical electric field.

## 4.2. Parallel Plate Electrodes - Fundamental Mode Resonator

### 4.2.1. Device Design and Simulation

The simplest intrinsically switchable contour mode resonator design consists of a thin film of BTO sandwiched between a pair of electrodes as shown in the bottom right of

Figure 4.2. The width ($W$) of the BST slab and the effective acoustic wave velocity ($v_{a,eff}$) of the structure determine the fundamental resonance frequency of the parallel plate contour mode resonators as given by

$$f_s \approx \frac{v_{a,eff}}{2W} \approx \frac{1}{2W}\sqrt{\frac{E_P}{\rho(1-\sigma^2)}}. \tag{4.1}$$

Table 4.1: Material Properties of BTO

| | $\rho$ (kg/m$^3$) | $\sigma$ | $E_P$ (GPa) |
|---|---|---|---|
| BTO | 5800 | 0.3 | 67 |

By neglecting the effects of the top and bottom electrode, the effective acoustic wave velocity can be approximated using the mass density ($\rho$), in-plane Poisson's ratio ($\sigma$), and equivalent Young's modulus ($E_P$) of the BTO thin film [63]. The values of these parameters are listed in Table 4.1. Parallel plate contour mode resonators are typically formed into the shape of a circular ring (as shown in Figure 4.1), rectangular loop, or rectangular plate. The circumference/length/area of the ring/loop/plate, the thickness and permittivity of the BST, and the coverage of the electrodes determine the capacitance of the resonator. The resonance frequency and capacitance of the resonator can be chosen to obtain the desired impedance level, which is typically 50 Ω.

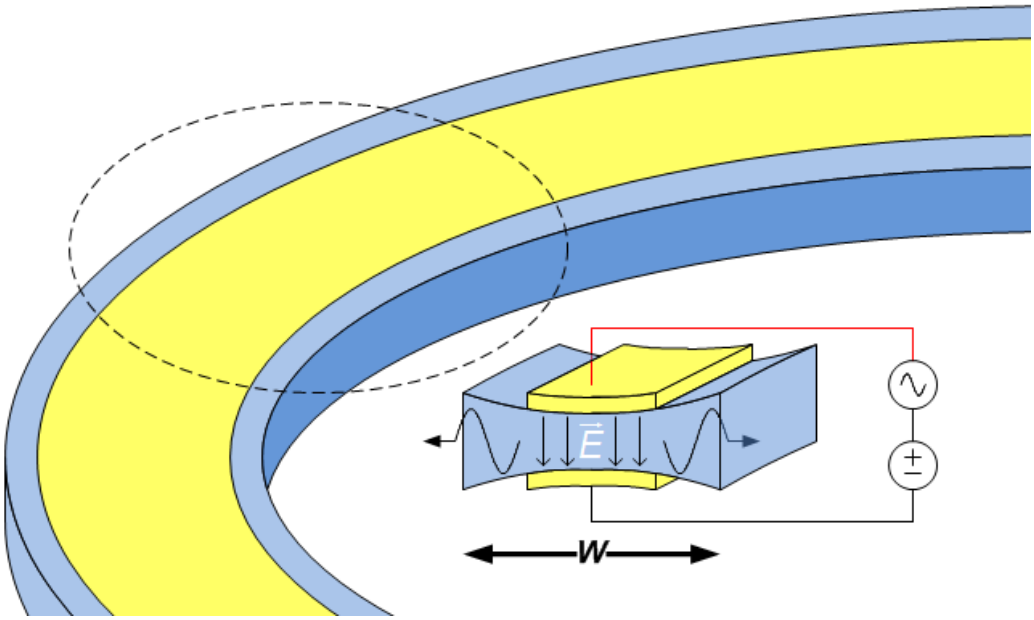


Figure 4.2: Ring-shaped contour mode resonator with single pair of parallel plate electrodes for exciting laterally propagating acoustic waves in response to the applied RF electric fields.

Contour mode resonators can also be designed using COMSOL Multiphysics with the same method used for designing FBARs as discussed in Chapter 2. A 2D simulation of a parallel plate contour mode resonator with a 400 nm BTO layer and 100 nm platinum electrodes is performed to illustrate the desired resonance mode, which is shown in Figure 4.3. In the simulation results, the color indicates the total displacement of the resonator body and shows that the displacement is only a function of lateral position and is maximized at the lateral boundaries of the device. This is in agreement with the mechanical boundary conditions of the device which require the boundary to be under zero strain. The eigenfrequency of this mode is also very similar to the value obtained analytically from (4.1).

Figure 4.3: COMSOL Multiphysics simulation showing the total displacement of a parallel plate electrode contour mode resonator. Red indicates a large displacement and blue indicated a small displacement.

### 4.2.2. Device Fabrication and Measurement Setup

After the resonator has been designed, it is fabricated using a process similar to the procedure given in Chapter 2. The procedure for fabricating parallel plate electrode fundamental mode resonators is summarized in Figure 4.4. A microphotograph of a fabricated circular ring-shaped contour mode resonator with an outer diameter of 80 μm, electrode width of 10 μm, and BST width of 20 μm is given in Figure 4.5.

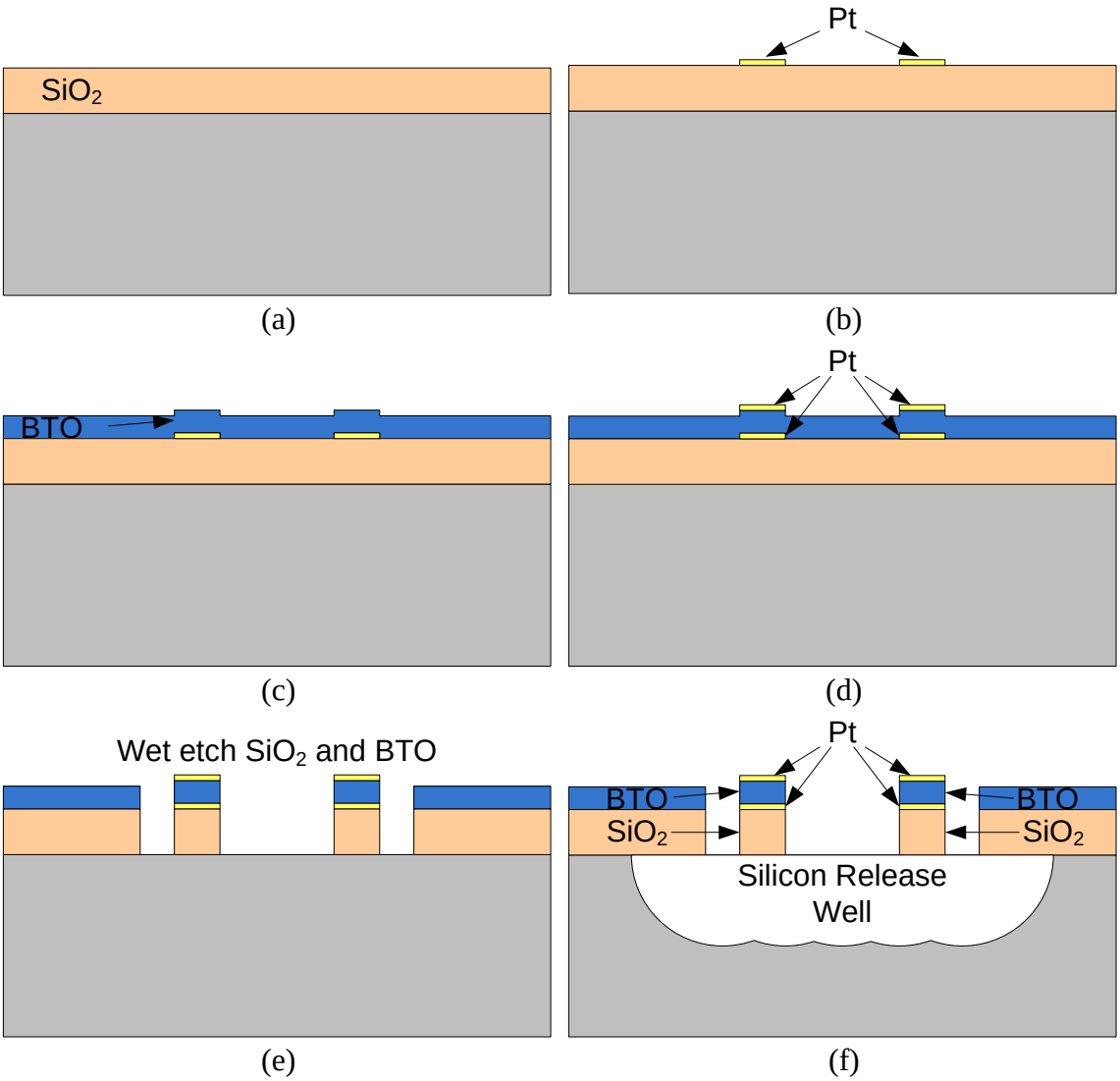


Figure 4.4: Step by step illustration of the fabrication process. (a) Start with a 525 μm thick high resistivity silicon substrate (5000 Ω·cm) with a layer of thermal SiO2 is deposited on top. (b) A 100 nm layer of platinum is patterned by e-beam evaporation and liftoff to serve as the bottom electrode. (c) A 405 nm BTO thin film is then deposited by pulsed laser deposition (PLD) using the conditions described in Chapter 2. (d) The top electrode is deposited using the identical procedure as for the bottom electrode. (e) The resonator structure is defined by wet etching the BTO and SiO2 layers. Then 500 nm of gold is deposited for the CPW probe pads (not pictured). (f) Device is released by an isotropic silicon dry etching process using $XeF_2$.

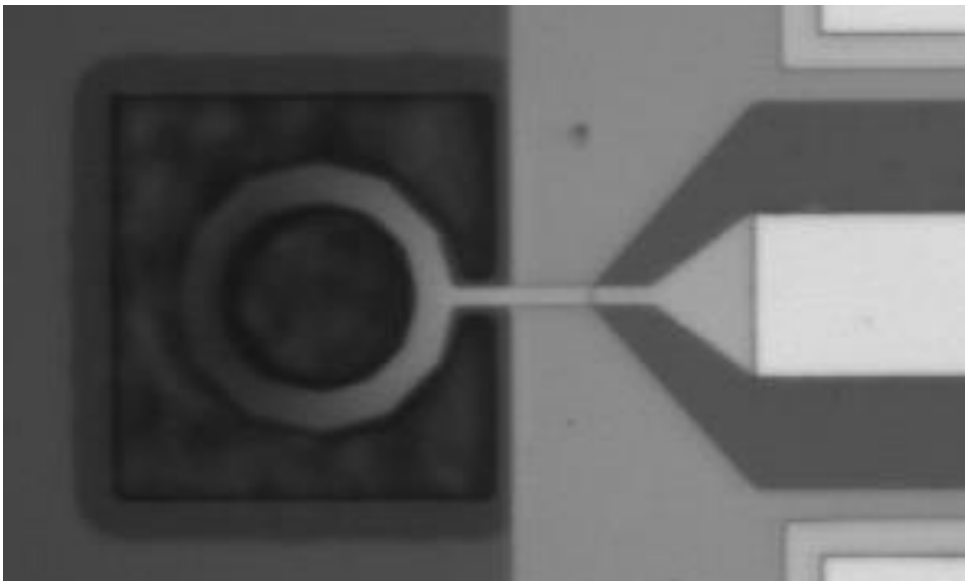

Figure 4.5: Microphotograph of a released one-port intrinsically switchable circular ring-shaped BTO thin film contour mode resonator. The bending of the resonator structure causes the section away from the tether to be out of focus.

The fabricated contour mode resonator is characterized using an Agilent E8364B vector network analyzer and a GGB ground-signal-ground (GSG) probe with a pitch size of 150 μm. Short-open-load calibration is performed using a GGB Industries CS-5 calibration substrate prior to characterizing the devices under test (DUTs), setting the measurement reference plane at the GSG probe tips. DC bias is applied to the port of the device through a bias tee.

### 4.2.3. Measurement Setup/Measurement Results

The input impedance of the resonator, $Z_{in}$, is measured as the dc bias voltage is gradually increased from 0 V to 12 V. In the absence of dc bias, the spontaneous polarization of the BTO thin film results in a weak resonance at 158 MH as shown by the blue solid trace in Figure 4.6 (a). At a 1 V DC bias, the film is unpolarized and has no piezoelectric response and therefore the resonance is turned off, as can be seen from the

green dotted trace shown in Figure 4.6 (a) and Figure 4.6(b). At 12 V dc bias, the polarization of the material leads to a strong piezoelectric response and the resonator exhibits a series resonance frequency $f_s$ of 159.7 MHz and a parallel resonance frequency $f_p$ of 160.45 MHz as can be seen from the blue solid trace in Figure 4.6 (a). The quality factors are calculated to be 47 and 83 for the series and parallel resonance frequencies, respectively. The effective electromechanical coupling coefficient is calculated to be 1.15%, which is comparable to that of piezoelectric AlN thin film contour mode resonators [63].

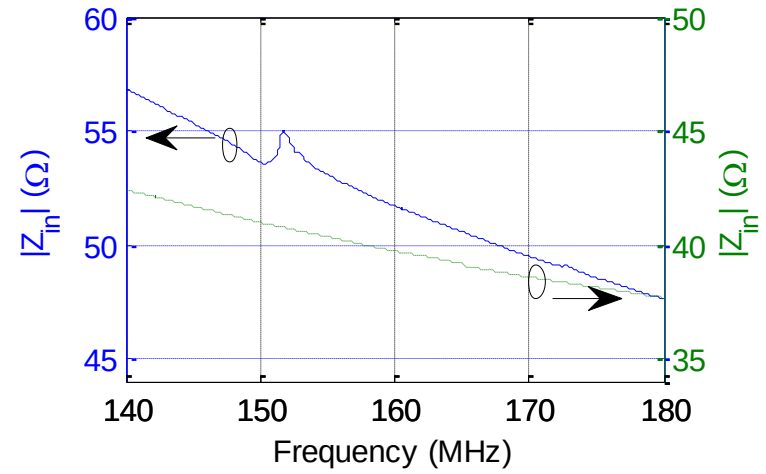


(a)

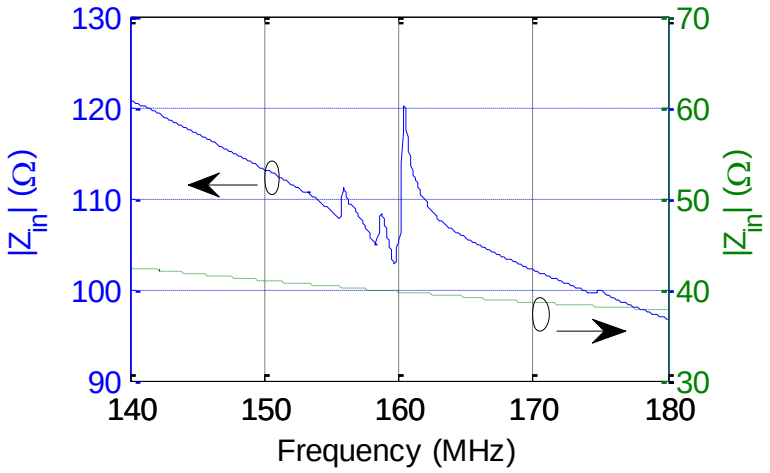


(b)

Figure 4.6: (a) Measured input impedance of a one-port circular ring-shaped contour mode resonator with an applied dc bias voltage of 0 V (blue solid trace) and 1 V (green dotted trace). (b) Input impedance of the same device with an applied dc bias voltage of 12 V (blue solid trace) and 1 V (green dotted trace).

The measured resonance frequencies of the BTO resonator at various dc bias voltage is shown in Figure 4.7. The results show that both the series and the parallel resonance frequencies increase with voltage. The tunability of this resonator can be calculated using

$$T_f(V_{\min}, V_{\max}) = \frac{f(V_{\min}) - f(V_{\max})}{f(V_{\min})} 100\% \tag{4.2}$$

where $V_{min}$, the minimum voltage at which resonance occurs, and $V_{max}$, the maximum applied voltage [35]. The tunability of the series and parallel resonance frequencies are -0.31% and -0.41%, respectively, for $V_{min}$ = 5 V and $V_{max}$ = 12 V.

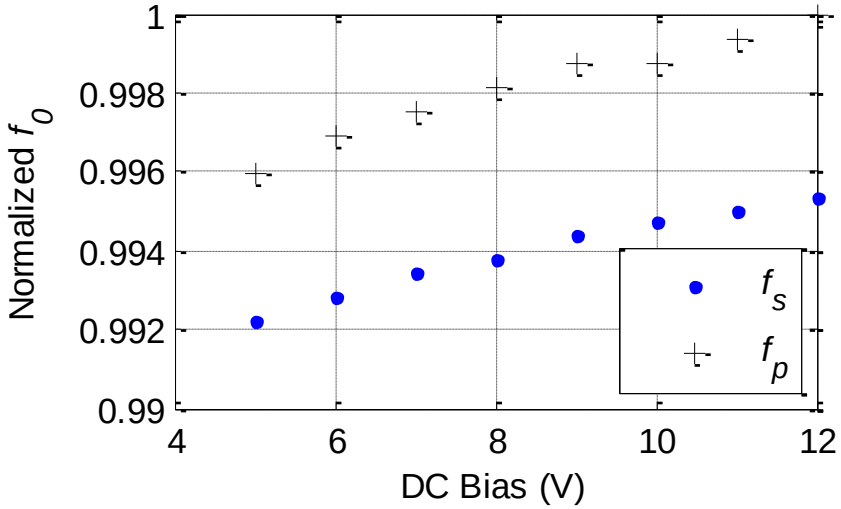


Figure 4.7: The measured series and parallel resonance frequency vs. applied dc bias voltage of a BTO circular ring-shaped contour mode resonator.

Circular ring-shaped, rectangular loop, and rectangular-plate contour mode resonators are most practical in the tens to hundreds of MHz range. In order to operate at higher frequencies, the width of the resonators would need to be significantly smaller than what has already been demonstrated. However, in reducing the resonator width, the required resonator geometry for maintaining adequate performance would be structurally unfeasible [63]. Another approach to achieving higher frequency devices is to utilize higher order resonance modes that can also exist within the resonator body. This is the approach that is discussed in the next section. To excite these higher order resonance modes, interdigitated electrodes are employed.

## 4.3. Interdigitated Electrodes - Overmoded Resonator

### 4.3.1. Design

The interdigitated contour mode resonators presented here consist of a rectangular BTO thin film with interdigitated top and/or bottom electrodes to obtain GHz frequency operation. This structure is more mechanically robust and better at suppressing spurious responses compared to non-interdigitated resonators of the same frequency [63]. Interdigitated contour mode resonators can be designed as either thickness field excitation (TFE) or lateral field excitation (LFE) devices. In TFE resonators, the electric field vector are almost entirely perpendicular to the plane of the thin film and in LFE resonators, the electric field vectors have a component parallel to the plane of the thin film [64]. Both utilize the transducing material's $d_{31}$ (effective) piezoelectric coefficient to realize contour mode resonators [64]. In both instances, induced acoustic waves that propagate in the lateral direction are confined within the resonator body due to the interface between the resonator body and air. However, LFE resonators are less complex and may not require as many fabrication steps while TFE resonators typically have larger effective electromechanical coupling coefficients [64, 65]. Here, one-port TFE interdigitated contour mode resonators, which are excited by applying an RF signal and dc bias to the interdigitated electrodes in the alternating fashion shown in Figure 4.8, are discussed.

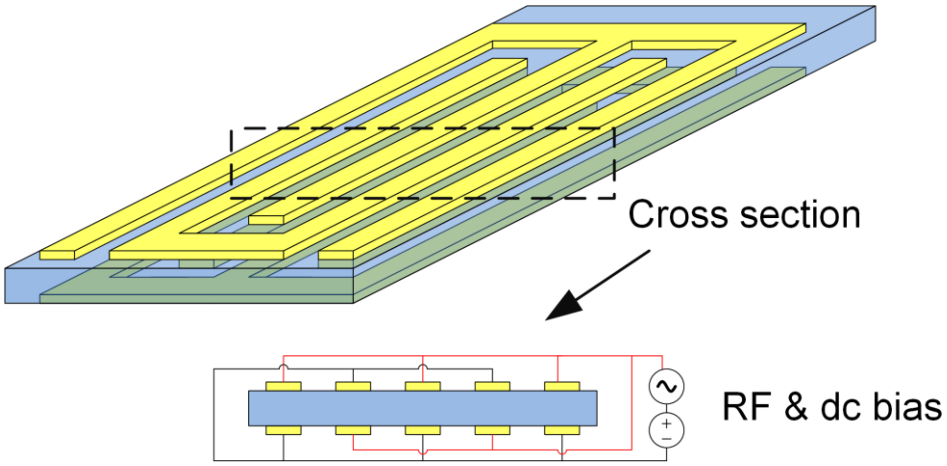


Figure 4.8: Cross sectional view of an interdigitated contour mode resonator showing the signal path and biasing configuration.

The series resonance frequency ($f_s$) of the contour mode resonator model shown in Figure 4.9(a) is determined by the width and spacing of the interdigitated electrodes as well as the material properties of the resonator body. The value of $f_s$ can be approximated with (4.3) based on the parameters defined in Table 4.2 [63, 66]. It is dependent on the lateral acoustic velocity of BTO ($v = \sqrt{E_{BTO} / \rho_{BTO}}$), the correction factor ($\Phi$), which accounts for the contributions of the electrodes, and the lateral periodicity of the structure ($2 \cdot W_{res}$). Since the lateral periodicity of the resonators is defined lithographically, the number of operating frequencies for devices on a single chip is independent of the number of processing steps, significantly reducing cost and complexity. This is very advantageous for the design of monolithic resonator and filter banks.

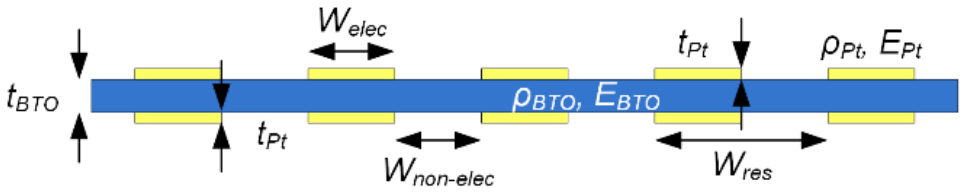


(a)

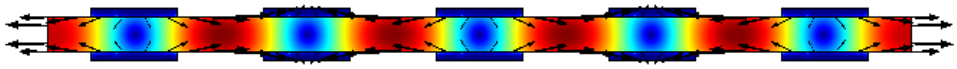

(b)

Figure 4.9: (a) The parameters of interdigitated contour mode resonators used for approximating the series resonance frequency. (b) The desired length extensional resonance mode of the BTO thin film resonator.

$$f_s \approx \frac{\sqrt{E_{BTO}/\rho_{BTO}}}{2W_{res}\Phi},$$

$$\Phi = \sqrt{\frac{1+\dfrac{\rho_{Pt}W_{elec}2t_{Pt}}{\rho_{BTO}(W_{elec}+W_{non-elec})t_{BTO}}}{1+\dfrac{E_{Pt}W_{elec}2t_{Pt}}{E_{BTO}(W_{elec}+W_{non-elec})t_{BTO}}}}. \tag{4.3}$$

Table 4.2: Variable Definition and Approximate Value

| Symbol | Quantity | Approximate Value |
|---|---|---|
| $E_{BTO}$ | BTO Young's modulus | 230 GPa |
| $t_{BTO}$ | BTO thickness | 400 nm |
| $\rho_{BTO}$ | BTO mass density | 5998.8 kg/m$^3$ |
| $E_{Pt}$ | Pt Young's modulus | 164.6 GPa |
| $t_{Pt}$ | Pt thickness | 100 nm |
| $\rho_{Pt}$ | Pt mass density | 21500 kg/m$^3$ |
| $W_{non\text{-}elec}$ | electrode separation | 1 μm |
| $W_{elec}$ | electrode width | 1 μm |
| $2{\cdot}W_{res}$ | lateral periodicity | $2{\cdot}(W_{elec} + W_{non\text{-}elec})$ |

The multi-physics simulation software COMSOL Multiphysics is used to solve for the different resonance modes of the resonator structure shown in Figure 4.9(a). Material parameters that are used for the simulation are taken from the COMSOL material library.

The simulation result of the desired contour mode resonance is shown in Figure 4.9(b) (where the arrows and colors show the displacement that occurs within the body of the resonator). It is observed that the displacement of the resonator body is periodic with respect to the lateral periodicity of the electrodes ($2 \cdot W_{res}$). This is expected since the electrodes are the source of the electrical excitation that causes the displacement within the resonator body by means of the electric field induced piezoelectric effect.

Although the contour mode resonance of the simple structure in Figure 4.9(a) can be easily excited and has a resonance frequency that can be analytically calculated using (4.3), the fabrication of this device is very complex. The modified structure shown in Figure 4.10(a) is utilized in this work to simplify the fabrication process while providing comparable performance. This new structure has an additional layer of dielectric below the bottom electrodes and a non-planar ferroelectric layer. COMSOL Multiphysics is used to simulate the frequency response of this resonator design. Only losses associated with the material are included.

The simulation results show a strong resonance at 1.57 GHz. The electric fields within the resonator are shown in Figure 4.10(b), (where the arrows show the electric field vectors and the colors represent the electric potential) and the mechanical displacement within the resonator is shown in Figure 4.10(c) (where the arrows show the displacement that occurs within the body of the resonator and the colors represent the lateral displacement). In Figure 4.10(c), the displacement is shown to be periodic with respect to the lateral periodicity of the electrical excitation applied to the top and bottom electrodes, which is the same as the desired mode shown in Figure 4.10(b). The results of the simulated five digit resonator illustrate the nature of the desired resonance mode for the fabricated device and validate

the excitation scheme. The physical dimensions of the simulated structure are used in the design and fabrication of the actual resonator.

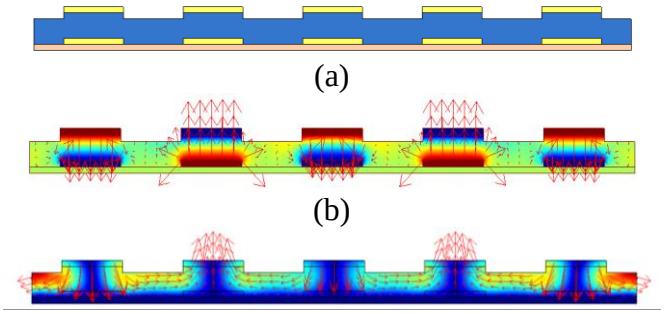


Figure 4.10: (a) The simulated 2-D resonator structure, (b) the electric fields due to the applied excitation, and (c) the mechanical displacement that occurs due to the contour mode resonance at 1.57 GHz.

## 4.3.2. Device Fabrication

The fabrication procedures of the interdigitated resonators are very similar to that of the circular ring-shaped contour mode resonators discussed earlier. Figure 4.11 visually summarized each fabrication step. A microphotograph of a fabricated interdigitated contour mode resonator with dimensions of 43 μm × 28 μm is given in Figure 4.12.

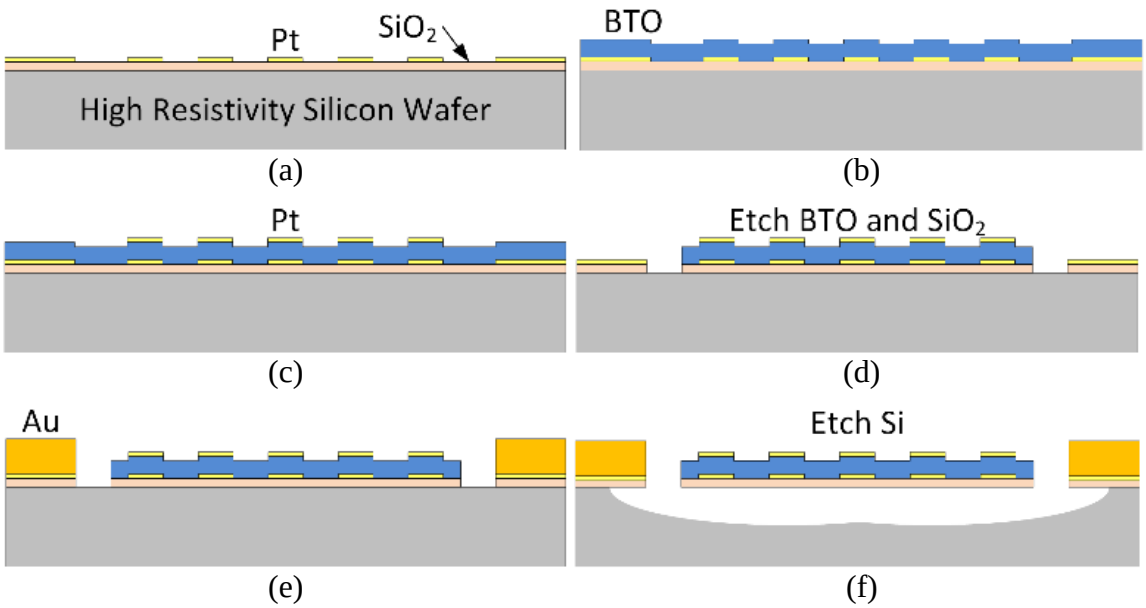


Figure 4.11: Step by step illustration of the fabrication process. (a) Bottom electrodes are deposited on top of a thermally oxidized silicon wafer. (b) Ferroelectric thin film is deposited. (c) Top electrodes are deposited. (d) Resonator body is defined by selectively etching away the ferroelectric and $SiO_2$. (e) Gold contacts are deposited. (f) The silicon beneath the device is etched, releasing the device which consists of $SiO_2$, Pt, BTO, and Pt (bottom to top).

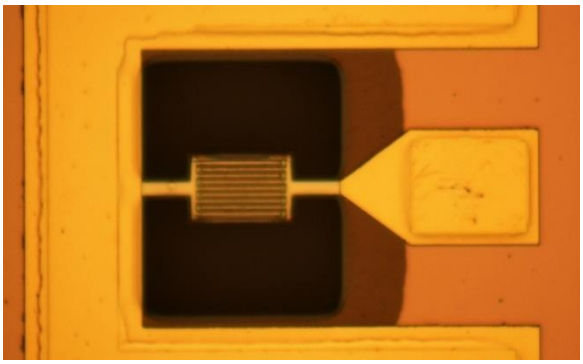

Figure 4.12: Microphotograph of a high frequency interdigitated contour mode resonator.

### 4.3.3. Measurement Setup

The fabricated interdigitated contour mode resonators are measured with 150 μm pitch GSG probes and the S-parameters of the devices are obtained using an Agilent E8364B vector network analyzer. Short-open-load calibration is performed using a GGB Industries

CS-5 calibration substrate prior to characterizing the devices under test (DUTs), setting the measurement reference plane at the GSG probe tips. S-parameters are taken from 100 MHz up to 5 GHz in 1.5 MHz increments at applied dc bias voltages starting from 0 to 15 V in 1 V increments.

### 4.3.4. Measurement Results

In order to determine the intrinsic performance of the DUT, the influence of the contact pads are de-embedded from the measurement results. Open and short test structures, where the resonator is not present and where the resonator is replaced with a conducting strip, respectively, are simulated in a 3-D electromagnetic solver, similar to what has been described in Hirano et. al. [67]. The material parameters used for simulating the de-embedding structures are determined as follows. The loss tangent of the ferroelectric thin film is extracted by measuring the test structures shown in Figure 4.13, which have been fabricated on the same chip as the resonators. It is calculated by using (4.4), where $Z_C$, $Z_1$, and $Z_2$ are the equivalent impedance of two series capacitors (Figure 4.13(a)), short through (Figure 4.13(b)), and long through (Figure 4.13(c)) 2-port CPW structures, respectively [68]. The conductivities of the platinum and gold that make up the contact pads are determined by measuring the S-parameters of a patch of material that has the same structure as the contact pads with SG probes and comparing them to S-parameters of a simulated patch. In addition, the dc resistance of the patch was also measured with a DMM and Signatone probe tips, verifying the conductivities. The high resistivity silicon substrate conductivity is provided by the manufacturer. After the simulation of the open and short test structures, the intrinsic device input admittance is calculated using (4.5), where $Z_{open}$,

$Z_{short}$, and $Z_{ext}$ are the input impedance of the open, short, and DUT, respectively, and $Y_{int}$ is the intrinsic input admittance of the resonator [18].

$$\tan\delta = \frac{\mathrm{Re}\{Z_C - Z_2 - 0.665\times(Z_1 - Z_2)\}}{\mathrm{Im}\{Z_2 + 0.665\times(Z_1 - Z_2) - Z_C\}} \tag{4.4}$$

$$Y_{\mathrm{int}} = \frac{1}{Z_{ext} - Z_{short}} - \frac{1}{Z_{open} - Z_{short}} \tag{4.5}$$

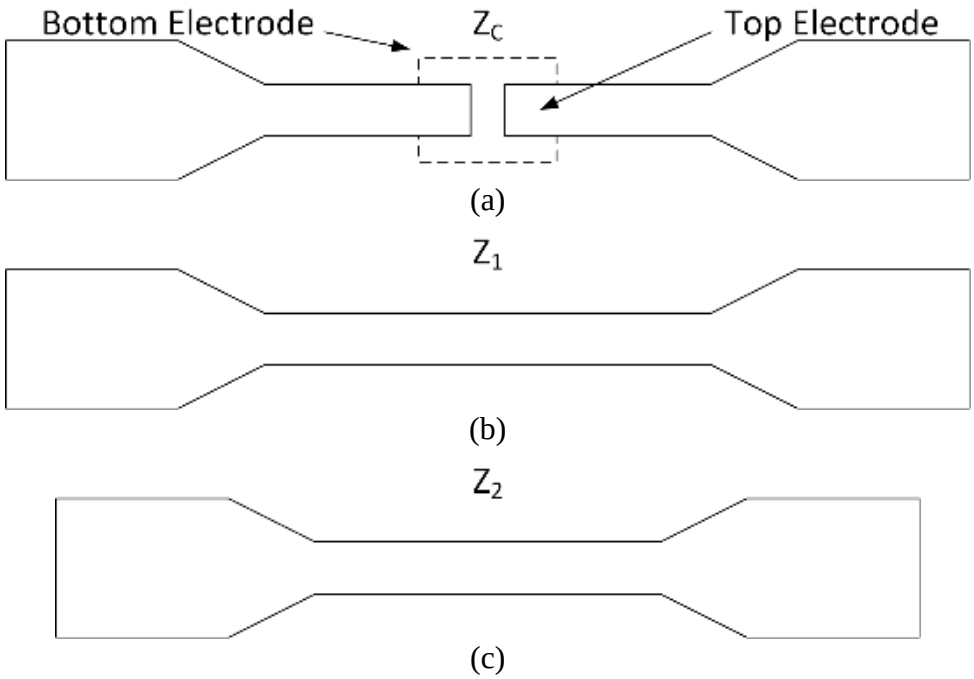


Figure 4.13: Layout of the top (solid line) and bottom (dashed line) electrodes for the CPW signal line of (a) two series capacitors, (b) long through, and (c) short through test structures for determining the loss tangent of the ferroelectric thin film (in between the top and bottom electrode) of the fabricated resonators.

Table 4.3:
Series Resonance Frequency of
Interdigitated Contour Mode Resonators at 15 V DC Bias

| Electrode Width | Electrode Spacing | Periodicity | $f_{series}$ |
|---|---|---|---|
| 4 μm | 4 μm | 16 μm | 0.46 GHz |
| 2 μm | 2 μm | 8 μm | 0.92 GHz |
| 1.4 μm | 1.4 μm | 5.6 μm | 1.26 GHz |
| 1 μm | 1 μm | 4 μm | 1.68 GHz |

Resonators of different periodicities and different number of digits are measured using the procedure discussed in the previous section. The electrode widths, periodicities, and series resonance frequencies of four different resonators are summarized in Table 4.3. The measured return loss, plotted in Figure 4.14 as a function of frequency, demonstrate the lithographically defined resonance frequencies of the resonator structure. The measured series resonance frequencies are also plotted against the calculated resonance frequencies from (4.3) in Figure 4.15, verifying the inverse relationship with the structure's periodicity, and subsequently electrode width. The series resonance frequency can be easily scaled to even higher frequencies and is only limited by the minimum feature size dictated by the process technology.

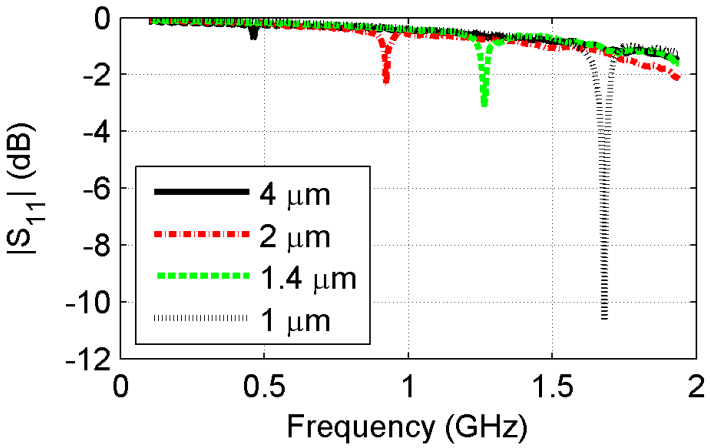


Figure 4.14: Measured $S_{11}$ of the interdigitated contour mode resonators with the indicated electrode width at 15 V dc bias.

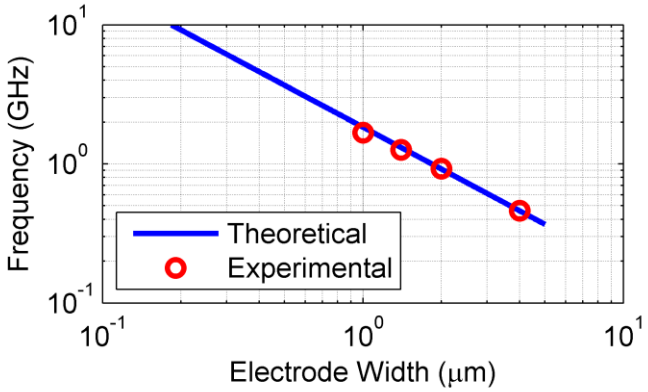


Figure 4.15: Fit of the calculated and experimentally measured resonance frequency of resonators (at 15 V dc bias) with different electrode widths.

The highest frequency interdigitated contour mode resonator that is demonstrated has a 1 μm electrode width and a series and parallel resonance frequency of 1.67 GHz and 1.68 GHz, respectively, with the application of a 10 V dc bias. In the absence of a dc bias, the response of the device is purely capacitive and does not exhibit any resonances. This is illustrated by Figure 4.16, which shows the measured input impedance of the resonator as a function of frequency at 0 and 10 V dc bias. The series and parallel resonance quality factors (*Q*s) of the resonator at 10 V dc bias are calculated to be 149 and 143, respectively,

using (4.6) [35, 69, 70]. After de-embedding the contributions of the contact pads, the intrinsic series and parallel resonance quality factors are calculated to be 178 and 152, respectively. The effective electromechanical coupling coefficient ($K^2_{eff}$) is calculated to be 2.0 % with (4.7), which is comparable to that of aluminum nitride interdigitated contour mode resonators [63, 66, 71].

$$Q_{s,p} = \frac{f}{2}\left|\frac{d\phi_{Zin}}{df}\right|,\ f = f_s, f_p \tag{4.6}$$

$$K^2_{eff} = \frac{\pi}{2}\frac{f_s}{f_p}\tan\left(\frac{\pi}{2}\frac{(f_p - f_s)}{f_p}\right) \tag{4.7}$$

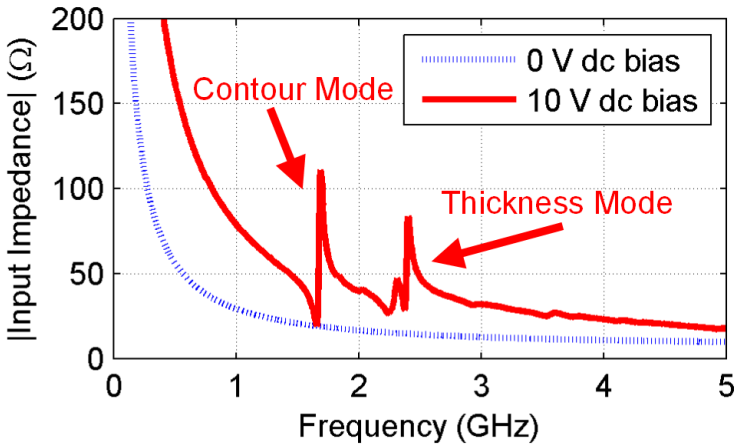


Figure 4.16: Measured input impedance for a 1 μm electrode width interdigitated contour mode resonator in the on and off state.

The additional resonances that occur near 2.4 GHz, shown in Figure 4.16, are present in all devices regardless of the electrode width as well as in the COMSOL simulation. They are the thickness mode resonances of the device. The theoretical thickness mode resonances for the fabricated devices are calculated to be approximately 2.6 GHz by using

the acoustic wave transmission line model of a $SiO_2$/Pt/BTO/Pt stack, corroborating with measurement results.

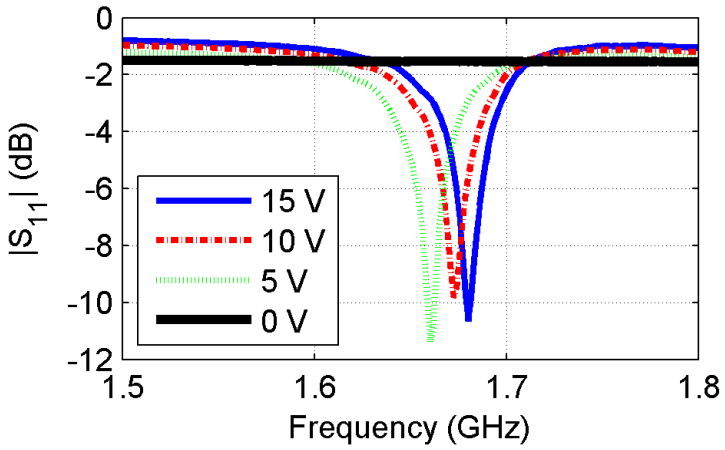


Figure 4.17: Measured $|S_{11}|$ of an interdigitated contour mode resonator with an electrode width of 1 μm at bias voltages of 0 V, 5 V, 10 V, and 15 V.

$Ba_xSr_{1-x}TiO_3$ based resonators exhibit bias voltage dependent resonance frequencies due to dc electric field dependent permittivity and polarization as well as nonlinear electrostrictive effects [30, 31]. Figure 4.17 shows the return loss of a 1 μm electrode width resonator at 0, 5, 10, and 15 V dc bias as a function of frequency. Figure 4.18 shows the measured input impedance of the same resonator from 1.3 to 2 GHz plotted on the Smith Chart. As the bias voltage increases the resonance frequency increases, which is consistent with the behavior of BTO resonators presented in [30, 35, 60]. Here, the series and parallel resonances are determined by where the input impedance is purely real and changes from capacitive to inductive and from inductive to capacitive, respectively. The tunability of the series and parallel resonance frequencies are calculated by using (4.2) to be -1.58 % and -1.81 %, respectively, for $V_{min}$ = 4 V and $V_{max}$ = 15 V. Figure 4.19 shows the normalized

resonance frequencies versus bias voltage and Table 4.4 summarizes the bias voltage dependent behavior of the contour mode resonator.

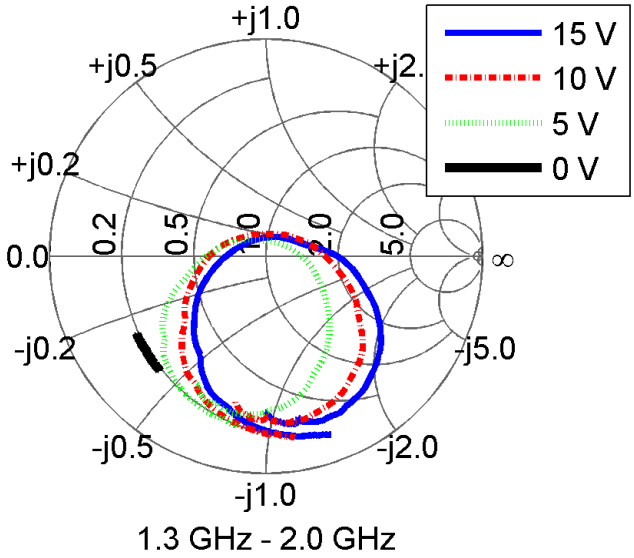


Figure 4.18: Response of an interdigitated resonator with a 1 μm electrode width at bias voltages of 0 V, 5 V, 10 V and 15 V plotted on a Smith Chart.

Table 4.4:
Measured Resonance at Various Bias Voltages

| Bias Voltage | $f_{series}$ | $f_{parallel}$ | $Q_{\text{series}}$ | $Q_{\text{parallel}}$ | $K^2_{eff}$ |
|---|---|---|---|---|---|
| 5 V | 1.652 GHz | 1.664 GHz | 111 | 192 | 1.8% |
| 10 V | 1.666 GHz | 1.680 GHz | 178 | 152 | 2.0% |
| 15 V | 1.676 GHz | 1.690 GHz | 160 | 121 | 2.0% |

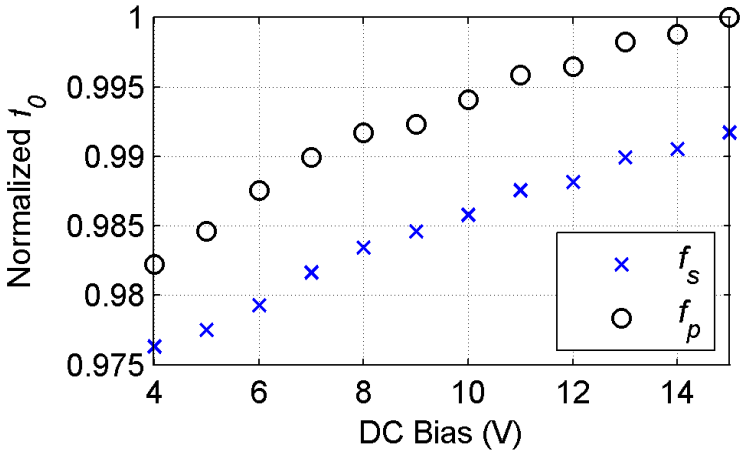


Figure 4.19: Plot of the normalized series and parallel resonance frequency versus bias voltage.

The tuning behavior in ferroelectric resonators can be used to correct for temperature and process variations (such as alignment error during photolithography and material growth variation). The dc voltages required to turn on and tune the resonators are larger than what is used for $V_{DD}$ of CMOS chips and would require dc-dc converters, which are commonly used in cell phones. However, the voltages are comparable to those used to actuate electrostatic resonators [10-12]. Furthermore, it should be possible to lower the dc bias voltages for turning on the resonators by reducing the thickness of the BTO thin film since the dc electric field strength within the ferroelectric would be maintained. The non-linear nature of ferroelectric devices is also a concern for high RF power applications. Nevertheless, there are techniques which have been developed for ferroelectric varactors and piezoelectric resonators that may also be applied to ferroelectric resonator design to increase their power handling [72-75].

### 4.3.5. Model Parameter Extraction of TFE Interdigitated Contour Mode Resonators

The equivalent circuit for interdigitated contour mode resonators is based on the Modified Butterworth-Van Dyke (MBVD) model, which is shown in Figure 4.20 [52]. It is useful for the design and analysis of resonators since it allows one to determine the electrical and acoustic characteristics of the device. In the model, the series connected $R_m$, $L_m$, and $C_m$ are the motional resistance, inductance, and capacitance of the resonator, respectively, and make up the acoustic branch. The series connected $C_0$ and $R_0$ are the electrical capacitance and its dielectric loss of the resonator, respectively, and make up the electrical branch. The parameter $R_s$ represents the ohmic loss of the metallization. The series resonance frequency is determined by the acoustic branch and occurs at a lower frequency than the parallel resonance frequency, which is determined by the combination of the acoustic and electrical branch. The value of each parameter in the model can be calculated from the resonance frequencies, effective electromechanical coupling coefficient, and quality factors of the measured device as outlined in [52]. Figure 4.21 shows the good agreement between the measurement results for a 1 μm electrode width interdigitated contour mode resonator and the extracted MBVD model over the frequency range of 0.1 to 2 GHz for dc bias voltages of 0, 5, 10, and 15 V.

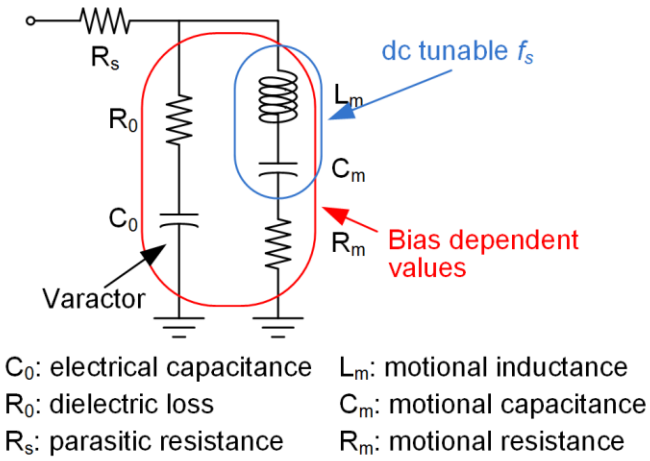


Figure 4.20: The Modified Butterworth-Van Dyke model for ferroelectric BAW resonators.

The performance of ferroelectric FBARs are dc bias voltage dependent and therefore the parameters of the equivalent circuit must be voltage dependent as well [43]. Without any dc bias, the value of $R_m$ is very large and behaves as an open circuit, preventing any resonances from occurring. As dc bias is applied and increased, the value of $R_m$ decreases, causing the resonances to turn on and grow stronger, respectively. The values of $L_m$ and $C_m$ also vary with bias voltage; as bias voltage increases, $L_m$ increases and $C_m$ decreases. The electrical capacitance of the resonator ($C_0$) decreases with increasing bias voltage, which is in agreement with the performance of ferroelectric varactors. Figure 4.22 and Figure 4.23 show the extracted value of $L_m$, $C_m$, and $C_0$ at voltages from 4 to 15 V for a 1 μm electrode width interdigitated contour mode resonator. The extracted values represent the tunability of the series ( $f_s \approx 1/(2\pi\sqrt{L_m C_m})$ ) and parallel ( $f_p \approx f_s\sqrt{1+C_m/C_0}$ ) resonance frequencies with bias voltage, which is shown in Figure 4.19. The bias voltage dependent MBVD model illustrates the equivalent electrical behavior of ferroelectric resonators [45]. It can be used to integrate the switching and tuning capabilities of ferroelectric thin film resonators into microwave circuit designs [76].

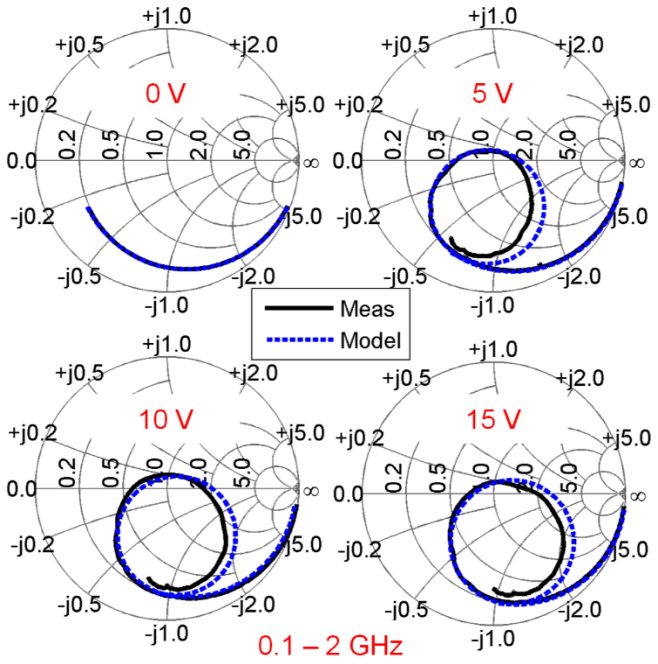


Figure 4.21: Comparison between measurement and MBVD modeling results of a 1 μm electrode width resonator for dc biases of 0, 5, 10, and 15 V from 0.1 to 2 GHz.

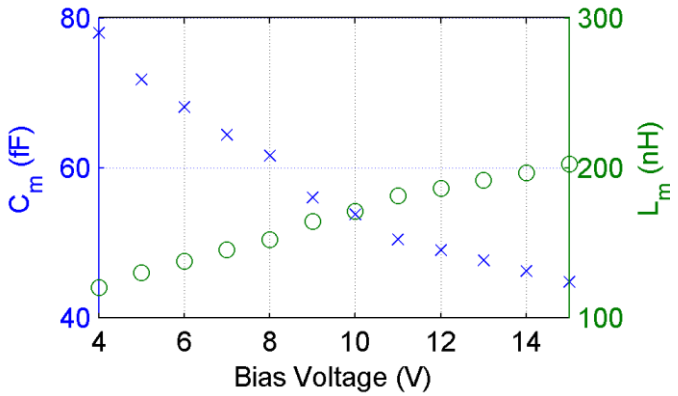


Figure 4.22: Extracted motional capacitance and motional inductance as a function of bias voltage of a 1 μm electrode width resonator.

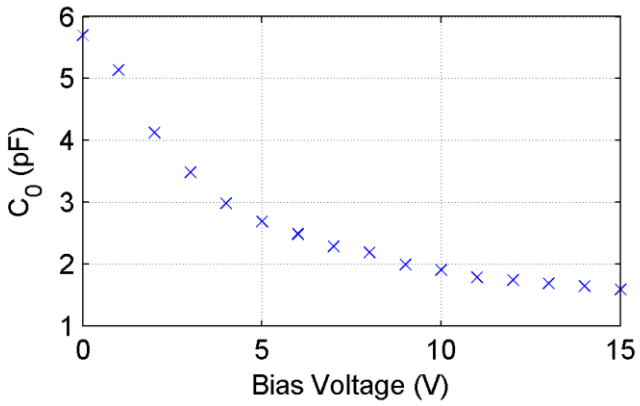


Figure 4.23: Extracted device capacitance as a function of bias voltage of the 1 μm electrode width resonator.

## 4.4. LFE Interdigitated Resonator

### 4.4.1. Design

LFE interdigitated contour mode resonators based on BTO have also been designed, measured, and fabricated. The structure of the resonator is shown in Figure 4.24. The resonator structure, excitation, and dc biasing is essentially the same as the TFE counterpart of the resonator except that the bottom electrodes and related design considerations are absent.

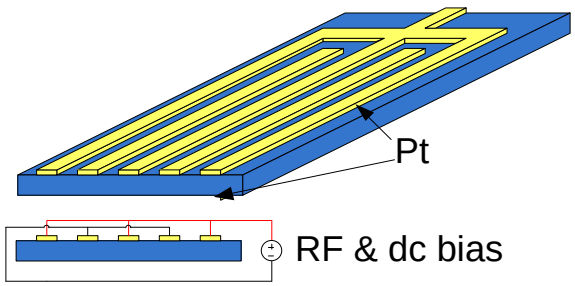


Figure 4.24: Structure of an LFE interdigitated contour mode resonator with top electrodes only. The excitation and dc biasing scheme is also shown.

### 4.4.2. Measurement Results

LFE interdigitated contour mode resonators are fabricated and characterized using procedures similar to what was used for their TFE counterparts. When 50 V of dc bias is applied to an LFE resonator with a 1 μm electrode width and 4 μm periodicity, two resonance modes are observed, as shown by the magenta trace in Figure 4.25. The contour mode response has series and parallel resonance frequencies of 1.734 and 1.797 GHz, respectively. The thickness mode response has series and parallel resonance frequencies of 2.499 and 2.631 GHz, respectively. Without dc bias, no resonances are observed, as shown by the black trace in Figure 4.25.

LFE interdigitated contour mode resonators have dc voltage controlled resonances and lithographically defined resonance frequencies similar to their TFE counterparts, yet have a much simpler fabrication process. However, the LFE resonators demonstrated here have weaker resonances compared to the demonstrated TFE resonators, suggesting that the electric field induced piezoelectricity is weak and the quality factor of the resonator is low. To address the former, a larger dc bias voltage can be applied or the electrode separation can be decreased in subsequent designs. To address the latter, the BTO thin film deposition process for non-platinized substrates can be studied and optimized.

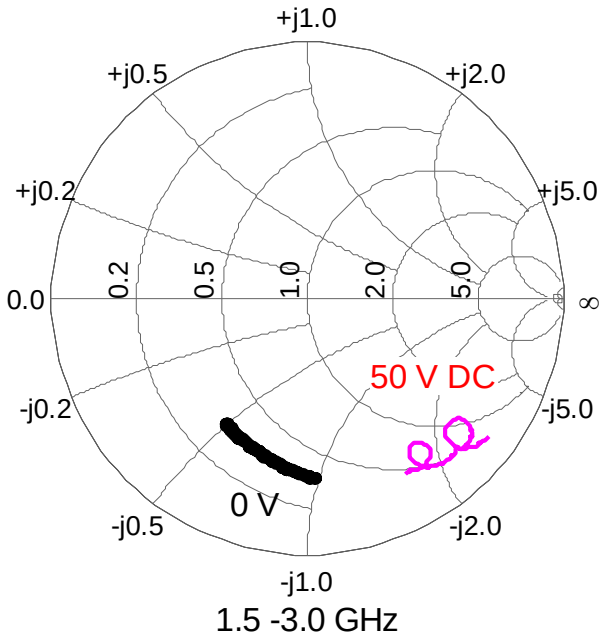


Figure 4.25: Measurement result of the top electrode only LFE interdigitated contour mode resonator at a bias voltage of 50 V.

## 4.5. Conclusion

In this chapter, contour mode resonators, which have resonance frequencies that are determined by their lateral dimensions, allowing resonators of virtually any frequency to be integrated onto a single substrate without the need for additional fabrication steps, are presented. BTO-based contour mode resonators can be intrinsically switched on and off by applying and removing the dc bias voltage across its terminals, respectively. Furthermore, its resonance frequency can be tuned by adjusting the dc bias voltage level.

Several different contour mode resonator designs are discussed. A parallel-plate fundamental mode contour mode resonator with a circular ring-shaped structure and a BTO thin film transduction layer has been designed, fabricated, and characterized. When a 12 V dc bias is applied to one such device, a contour mode resonance is observed with a series

and parallel resonance frequency of 159.7 and 160.45 MHz, respectively. The calculated quality factors of the former and latter are 47 and 83, respectively. Furthermore, thickness field excitation (TFE) and lateral field excitation (LFE) interdigitated contour mode resonators are discussed. At 10 V dc bias, the highest frequency TFE resonator exhibits series and parallel resonance frequencies of 1.67 GHz and 1.68 GHz with quality factors of 178 and 152, respectively. At 50 V dc bias, the demonstrated LFE resonator exhibits series and parallel resonance frequencies of 1.734 and 1.797 GHz, respectively. These devices are the first demonstration of intrinsically switchable interdigitated contour mode bulk acoustic wave resonators based on ferroelectric BTO thin films.

# CHAPTER 5

# Design and Assembly of an RF Magnetron Sputtering System for BST Deposition

## 5.1. Introduction

One major challenge in realizing our objective of integrating BST thin film capacitors, resonators, and filters to create very simple yet reconfigurable RF circuits for the design of intelligent/cognitive radios is realizing very high performance BST thin films with excellent within wafer and wafer-to-wafer uniformity. BST devices are made using micro-fabrication technology (similar to semiconductor device fabrication). For most of the intrinsically switchable and tunable microwave circuits discussed in this dissertation, the BST thin films have been deposited using a process called pulsed laser deposition (PLD). However, the design of larger and more sophisticated RF circuits for use in multi-standard radios require very precise, accurate, and uniform BST films which are not obtainable with the PLD system. The PLD system is also being shared among other research groups at the university, which deposit various other materials with the system, increasing the risk of contamination from other materials and the variation in film quality from sample to sample. In this chapter, an RF magnetron sputtering system that has been designed for and dedicated to BST thin film growth, shown in Figure 5.1, is discussed.

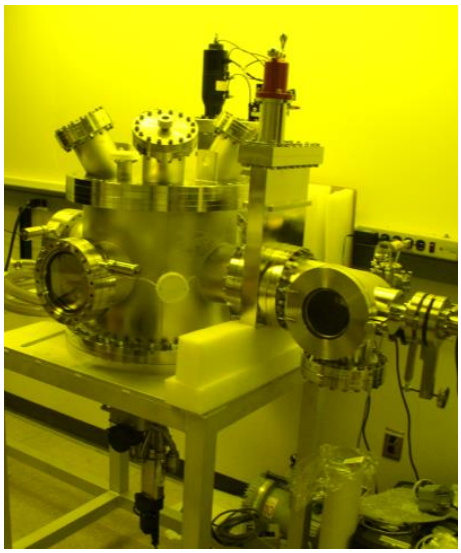

(a)

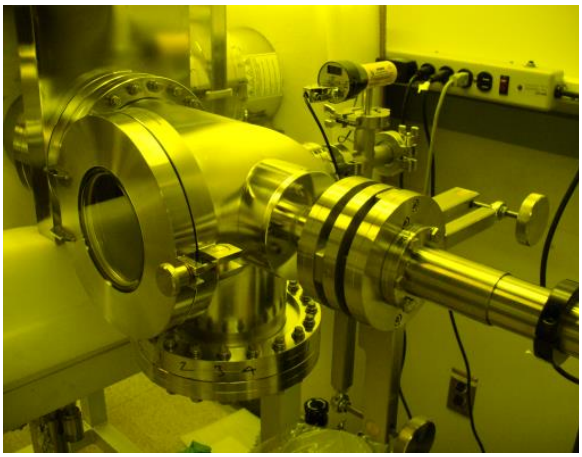

(b)

Figure 5.1: Assembled RF magnetron sputtering system for the deposition of ferroelectric BST thin films. (a) Main processing chamber. (b) Load lock and transfer arm.

Ferroelectric thin films are commonly deposited using RF sputtering, pulsed laser deposition (PLD), metal-organic vapor phase epitaxy (MOCVD), and atomic layer deposition (ALD) [18]. The setup of an RF magnetron sputtering system is chosen due to their ease of use, high quality films, and low operating cost. Furthermore, the deposition of uniform, high performance, and low impurity BST has been demonstrated by Professor Robert York's and Professor Suzanne Stemmer's group at UCSB as well as Professor Spartak Gevorgian's group at Chalmers University of Technology. The system assembled and setup at the University of Michigan is configured with two sputtering guns, which allows for the co-sputtering of $BaTiO_3$ and $SrTiO_3$ and enables the growth of BST with any stoichiometry. Also, the sputtering system is designed to hold up to four sputtering guns, which allows for the reactive sputter deposition of BST, providing even more control over BST stoichiometry. Stoichiometrically graded BST thin films can also be deposited with both of these methods. The ability to control the various stoichiometrically dependent properties of BST is essential for high performance BST thin film devices. In addition to

fine control over BST composition, the RF magnetron sputtering system has been designed for high temperature, high deposition rate, and high uniformity thin film growth and can accommodate wafers up to 4” in diameter. This new system will enable the design and fabrication of fully integrated BST based circuits and systems.

## 5.2. RF Magnetron Sputtering System Components

The RF magnetron sputtering system shown in Figure 5.1 is located in a UV light filtered cleanroom environment and is dedicated to the deposition of ferroelectric BST thin films. It has been assembled from parts that were purchased from various vendors. Each of the major components/subsystems are listed and described below.

### 5.2.1. Main Processing Chamber

The main processing chamber is a double walled cylindrical stainless steel vessel with a diameter and height of 16” and is the location where the film deposition occurs. The chamber is cooled by flowing chilled water through the chamber walls. There are three 8” and one 10” CF ports which are separated by 90º on the perimeter of the chamber. The 8” ports are attached to the load lock and view ports for transferring wafers into and out of the chamber. The 10” port is attached to the cryogenic pump through the 3-position gate valve. The top lid of the chamber has four 6” CF ports and can accommodate a maximum of four sputtering guns. Each port is 30º off the vertical axis and points to the exact center of the chamber. The bottom lid is configured with an 8” CF clearance port to accommodate the substrate assembly as well as a 1.33” mini CF flange for the substrate shutter. Several additional 2.75” CF ports are also located on the wall and lid of the chamber for gas

management, pressure measurement, etc. The entire main processing chamber rests on an aluminum support frame.

### 5.2.2. Load Lock and Substrate Assembly

The sputtering system is configured with a load lock and uses a manual linear motion transfer arm to transport the wafers between the load lock and the substrate assembly that is inside of the main processing chamber. The load lock enables the main processing chamber to be maintained under vacuum at all times, which helps prevent the introduction of contaminates into the thin film deposition environment. The load lock is also configured with a downward facing 8" CF port, which can be used to accommodate a turbomolecular pump a later time if necessary.

The substrate assembly is designed to be used with wafers up to 4" in diameter and has quartz lamp heaters that can heat the wafers up to 850 ºC. In addition, it is connected to an electrical motor that rotates the sample to improve film uniformity. Furthermore, the substrate assembly can be biased up to 100 V to adjust the plasma characteristics and deposition conditions inside the main processing chamber.

### 5.2.3. Mechanical Scroll Pump

The sputtering system requires a pump to bring the load lock and main processing chamber from atmospheric pressure to medium vacuum before the cryogenic pump can be used to reach ultra-high vacuum (UHV). Mechanical scroll pumps are commonly used for such purposes in thin film deposition systems because they are a type of dry pump and do not expose the vacuum system to any oils that are usually used for lubrication in other types of mechanical pumps. The introduction of hydrocarbons into the main processing chamber

should be avoided because it will contaminate the wafers and pollute the activated charcoal in the cryogenic pump, preventing the system from reaching its ultimate vacuum [77]. The sputtering system that has been setup is configured with an Edwards XDS 10 pump. Relevant specifications of the pump are listed in Table 5.1.

Table 5.1: Specification of the Scroll Pump

| **Parameter** | **Value** |
|---|---|
| Ultimate Vacuum | < 6 Pa (45 mTorr) |
| Maximum Pumping Speed | 11.1 $m^3$/hour |
| Inlet/Outlet Connections | DN25NW flange |

## 5.2.4. Cryogenic Pump

The sputtering system requires an additional pump to bring the main processing chamber from medium vacuum to ultrahigh vacuum. A Cryogenic pump was chosen due to their ease of operation and robustness. Cryogenic pumps operate by condensing gases (with the exception of helium, hydrogen, and neon) onto a cold head which is kept at cryogenic temperatures with the use of a closed-loop helium gas cooling system. The gases that do not condense are adsorbed by activated carbon cooled to 15-20 K within the cold head. Although cryogenic pumps have an initialization time of several hours and require periods of regeneration to restore the original pumping capacity, they have no mechanical components and are very robust. Furthermore, they have high water vapor pumping speed and high Ar, and $N_2$ retention [77]. The cryogenic pump is attached to the 10" 3-position gate valve that is attached to the 10" port of the main processing chamber.

## 5.2.5. RF Magnetron Sputtering Gun

The sputter system has two RF magnetron sputtering guns installed in the main processing chamber to allow for the deposition of either two distinct materials or the simultaneous deposition of the same material for increasing deposition rate. Each sputtering gun is fed by an RF power supply that can provide up to 300 W of power and is controlled by an automatic matching network for minimizing the reflected power. The sputtering guns can also be used with a DC power supply for depositing metals.

### 5.2.6. Sputtering Targets

The sputtering system is setup to sputter $Ba_{0.5}Sr_{0.5}TiO_3$ and $BaTiO_3$ thin films. These 4" diameter, 0.125" thick targets have a 0.125" copper backing plate which is used to help conduct heat away from the target as well as for attaching the target to the RF magnetron sputtering guns.

### 5.2.7. Gas Management and Pressure Measurement

The process gases are managed by a 3-position gate valve, mass flow controllers (MFCs), and pressure sensors. The 3-position gate valve throttles the pumping speed of the cryogenic pump and is used for establishing the partial pressure during deposition. The two MFCs control the flow of $O_2$ and Ar into the chamber. Lastly, the pressure sensors monitor the chamber pressure and indicate whether the 3-position gate valve position needs to be adjusted to achieve the desired partial pressure.

### 5.2.8. Water Chiller

The sputter system has a water chiller which cools the main processing chamber, the RF magnetron sputtering guns, the helium compressor that is used for the cryogenic pump,

and the substrate assembly. The chiller has a 7.0 kW cooling capacity and the heat is dissipated through the closed-loop chilled water lines of the building so that the heat is not dissipated into the laboratory environment.

## 5.3. Film Deposition Parameters

There are many different deposition parameters that affect the properties of the sputtered film. Table 5.2 gives the deposition parameters that have been chosen for the system discussed here.

Table 5.2: RF Sputter Deposition Parameters

| | |
|---|---|
| Target Material | $Ba_{0.5}Sr_{0.5}TiO_3$ |
| Number of Target/Sputtering Guns | 2 |
| RF Power | 2 × 300 W |
| Substrate Temperature | 650 ºC |
| Gas Flow | Ar/O2: 75/25 sccm |
| Chamber Partial Pressure | 45 mTorr |
| Deposition Time | Thickness Dependent |
| Substrate Temperature Ramp Up/Down Rate | 20 ºC/minute |

## 5.4. Film Characterization

Material characterization is a significant portion of setting up the system for thin film deposition. Many different growth conditions affect the properties/quality of the BST. Deposition parameters, such as gas pressure, gas ratio, substrate temperature, growth rate, source to target distance, etc., need to be studied to understand how each affects the following film properties. The composition of the film, which can vary due to the different atomic weights of Ba, Sr, Ti, and O, needs to be determined by using Rutherford backscattering spectrometry (RBS). The crystallinity of the film, which is extremely

important in the tunability of the capacitors, needs to be characterized by X-ray diffraction (XRD). The film roughness, which determines the quality factor of resonators and the signal loss in filters, needs to be measured using atomic force microscopy (AFM). Once material characterization is completed and the deposition parameters for the growth of high quality films are determined, the performance BST capacitors, resonators, and filters need to be characterized with DC (constant voltage) and RF probes. The results of the film characterization are not a part of this thesis.

## 5.5. Conclusion

An RF magnetron sputtering system has been setup for depositing uniform, high performance, and repeatable BST thin films. The system is currently configured with two 4" RF magnetron sputtering guns that are oriented 30º off the vertical axis and is able to accommodate wafer up to 4" in diameter. The deposition parameters such as substrate temperature, partial pressure, gas mixture ratio, RF power, target-to-substrate distance, etc. have been determined to obtain high quality films. Complete film characterization is currently underway.

# CHAPTER 6
# Conclusions and Future Work

## 6.1. Conclusion

The work in this thesis demonstrates how the unique and multifunctional properties of ferroelectric thin films can be used to develop intrinsically switchable resonators and filters for applications such as intelligent/cognitive wireless communication systems. BST, which has been well characterized in the microwave frequency regime and exhibits a large and electric field dependent permittivity as well as electric field induced piezoelectricity, allows for the fabrication of highly compact and potentially monolithic adaptive and reconfigurable RF circuits.

The contribution of this thesis in the area of ferroelectric thin film devices fall into four major categories. In Chapter 2, the design, fabrication, characterization, and modeling of BST FBARs is been discussed. FBAR design is performed by using the acoustic wave transmission line model, which represents each different thin film that makes up the FBAR structure as a transmission line for acoustic waves, to obtain the desired resonance frequency and impedance level. Multiphysics FEM simulation tools such as COMSOL Multiphysics can be used in conjunction with the acoustic wave transmission line model for design verification. Once the design is finalize, device fabrication is perform in the Lurie Nanofabrication Facility located at the University of Michigan. The fabricated

devices are characterized for their dc bias dependent behavior, RF power dependent/large-signal behavior, and switching reliability. BST FBARs that are in the paraelectric phase behave as capacitors when there is no dc bias. When dc bias is applied to BST FBARs, RF signals of particular frequencies excite acoustic waves that add constructively within the bulk of the device, resulting in an electrical resonance. As the dc bias is increased, the electric field induced piezoelectricity grow stronger, causing an increase in the effective electromechanical coupling coefficient of the device. Furthermore, the non-linear electrostrictive effect and electric field dependent permittivity cause the resonance frequency to shift/tune. A BST FBAR has been demonstrated with a tunability as high as 5.33%. In this work, it was also determined that by increasing the RF power applied to BST resonators, changes in the electromechanical coupling coefficient, quality factor, and resonance frequency are also observed. Furthermore, these effects can minimized by increasing the dc bias voltage. To ensure that the performance of BST resonators do not degrade when exploiting their voltage dependent behavior, a reliability study that switched a device on and off for over one billion cycles was completed and no apparent degradation was observed. With the assurance of their high reliability and consistent behavior in addition to the interest in utilizing BST FBARs in more advanced and high power microwave and RF circuits, their dc bias and RF power dependent behavior are modeled using a non-linear version of the MBVD model to enable circuits designs that can take advantage of their multifunctional capabilities. After studying individual ferroelectric FBARs, their electric field dependent piezoelectricity was utilized to design reconfigurable BST FBARs that could switch on individual or multiple electrical resonances by using a very simple dc biasing scheme that can be easily controlled by low cost digital circuitry.

In Chapter 3, intrinsically switchable ferroelectric FBAR filters that utilize the properties of BTO and BST FBARs have been designed, fabricated, and characterized. The filters are designed by using the modified Butterworth-Van Dyke (MBVD) and acoustic wave transmission line models established in Chapter 2 together with the circuit simulator, Advanced Design System (ADS), to represent the resonators that form the electrically coupled ladder filters. They are fabricated using the same basic process as was used for BST FBARs with the addition of a few extra steps for the mass loading/compensation layers and the thin film resistors used for biasing. The fabricated 1.5 stage ladder filters were then characterized for their dc bias voltage dependent behavior, switching reliability, and switching speed. When the ferroelectric FBAR filters are off, the input and output are isolated by 14 dB. When they are switched on by controlling the applied dc bias, a passband response with an insertion loss as low as 4.1 dB and center frequency of 1.60 GHz is observed. Furthermore, the insertion loss and center frequency can be tuned with the bias voltage level. BST FBAR filters that leverage BST varactors have also been used to design reconfigurable BST FBAR filters. The BST varactors are used as an internal dc block and improve the performance of the filters that are switched on by minimizing the loading effect of the filters that are switched off. Furthermore, with the biasing scheme developed here, a notch response is observed at the center frequency of the filters that are switched off.

In Chapter 4, several different BTO contour mode resonators, which have resonance frequencies defined by their lateral dimension and operate at resonance modes determined by the electrode patterning, have been designed, fabricated, and characterized. The benefit of this type of structure is the ability to fabricate resonators over a wide range of frequencies

without the need for additional processing steps. Parallel plate and interdigitated electrode contour mode resonators are designed analytically and their mode of operation is verified with COMSOL Multiphysics. The resonators are fabricated using a very similar approach as compared to BST resonators but require their BTO thin film be precisely etched to define the acoustic boundaries for the laterally propagating bulk acoustic waves. As with BST based resonators, BTO contour mode resonators can be switched on and off by controlling the applied dc bias voltage and as the bias voltage is increased, the resonance frequency increases, which agrees with measurement results of BTO based FBARs. A circular ring-shaped parallel plate resonator with a frequency of 160 MHz and an interdigitated resonator with a frequency of 1.67 GHz have been demonstrated.

In Chapter 5, the design, assembly, and setup of an RF magnetron sputtering system dedicated to BST thin film deposition is discussed. The different components of the system are described and the deposition parameters for depositing high quality BST thin film are given. Complete film characterization is currently underway.

## 6.2. Future Work

The work presented here only represents a small fraction of what is possible with ferroelectric thin film technology. There are still many significant contributions that can be made in the field of ferroelectric thin film BAW devices. For example, there is a need to develop ferroelectric thin film BAW resonators that can achieve higher frequencies, higher quality factors, higher effective electromechanical coupling coefficients, and improved linearity. Ongoing work in Professor Mortazawi's research group is aimed at addressing these issues. Additional projects involving new designs and applications of ferroelectric

thin film resonators, and improved understanding of ferroelectric thin films and devices are given in the following sections.

### 6.2.1. Reconfigurable Contour Mode Resonators and Filters

In Chapter 4, the design, fabrication, and performance of individual BTO contour mode resonators that operated in the low GHz frequency range was presented. The different resonators had resonance frequencies that were determined by lithographically defined features and therefore, each device was able to be fabricated on the same wafer using a minimal number of processing steps. The next phase of research is to incorporate several different contour mode resonators to create more sophisticated devices. One particular application is the design of reconfigurable resonators, which was previously demonstrated in Chapter 2 with BST FBARs. The fabrication process for reconfigurable contour mode resonators would not require the additional processing steps used for depositing additional mass loading/compensation layers that were previously used. The benefit of contour mode resonators also applies to the design of filters and reconfigurable filters, which were previously demonstrated with ferroelectric FBARs in Chapter 3.

### 6.2.2. Fully Characterize and Automate RF Magnetron Sputtering System

The RF magnetron sputtering system discussed in Chapter 5 has been setup for the deposition of ferroelectric thin films. Additional work to fully automate the thin film deposition process and data logging of the deposition parameters would significantly help with the complete characterization of the system. The system has been designed with computer automation in mind from the very beginning. By creating a computer program

for controlling all the different components and instruments, the number of extraneous variables that influence the quality of the deposited films would be decreased. Furthermore, once a recipe is established, the run to run variation can be minimized.

### 6.2.3. Complete Physics Based Modeling of Ferroelectric Resonators

In Chapter 2, a nonlinear MBVD model was developed to represent the dc bias voltage and RF power dependent behavior of characterized BST FBARs. The nonlinear model parameters of a measured device can extracted by using the procedure that have been outlined. Other research groups have developed voltage dependent physics based models of BST resonators that are derived from Landau free energy P-expansion. One new project would be to incorporate the RF power dependent behavior of BST FBARs into the dc bias voltage dependent physics based models for a complete physics based model.

## 6.3. Select List of Publications

### 6.3.1. Journal Papers

**V. Lee**, S. A. Sis, J. Phillips, and A. Mortazawi, "Intrinsically Switchable Ferroelectric Contour Mode Resonators," *IEEE Transactions on Microwave Theory and Techniques,* vol. 61, no. 8, pp. 2806-2813, Aug. 2013.

S. Lee, **V. Lee**, S. A. Sis, and A. Mortazawi, "Large-Signal Performance and Modeling of Intrinsically Switchable Ferroelectric FBARs," *IEEE Transactions on Microwave Theory and Techniques,* vol. 61, no. 1, pp. 415-422, Jan. 2013.

X. Zhu, **V. Lee**, J. Phillips, and A. Mortazawi, "An Intrinsically Switchable FBAR Filter Based on Barium Titanate Thin Films," *IEEE Transactions on Microwave and Wireless Components Letters*, vol. 19, no. 6, pp. 359-361, June 2009.

### 6.3.2. Conference Proceedings/Digests

**V. Lee**, S. A. Sis, S. Lee, X. Zhu, and A. Mortazawi, "Lateral Mode Intrinsically Switchable Barium Titanate Bulk Acoustic Wave Resonators," in *Proceedings of the 8th European Microwave Integrated Circuits Conference (EuMIC)*, Nuremberg, Germany, 2013, pp. 1-4.

**V. Lee**, S. Lee, S. A. Sis, and A. Mortazawi, "Switching Reliability of Tunable Ferroelectric Resonators and Filters," in *IEEE MTT-S International Microwave Symposium Digest*, Seattle, WA, 2013, pp. 1-3.

**V. Lee**, S. A. Sis, S. Lee, and A. Mortazawi, "Intrinsically Switchable Ferroelectric Bulk Acoustic Wave Filters Based on Barium Strontium Titanate Thin Films," in *IEEE MTT-S International Wireless Symposium Digest*, Beijing, China, 2013, pp. 1-4.

**V. Lee**, S. Lee, S. A. Sis, and A. Mortazawi, "Large signal performance of ferroelectric FBARs," in *IEEE MTT-S International Microwave Symposium Digest*, Montreal, QC, Canada, 2012, pp. 1-3.

**V. Lee**, S. A. Sis, and A. Mortazawi, "Ferroelectric Resonators and Filters for Reconfigurable Radios," in *Proceedings of the Army Science Conference* (27th), Orlando, FL. 2010.

**V. Lee**, S. A. Sis, X. Zhu, and A. Mortazawi, "Intrinsically switchable ferroelectric BAW resonators and filters," in *Proceedings of the 2010 European Microwave Conference (EuMC)*, Paris, France, pp. 803-806.

**V. Lee**, S. A. Sis, X. Zhu, and A. Mortazawi, "Intrinsically switchable interdigitated barium titanate thin film contour mode resonators," in *IEEE MTT-S International Microwave Symposium Digest*, Anaheim, CA, 2010, pp. 1448-1450.

**V. Lee** and A. Mortazawi, "Ferroelectric Thin Film Based Intrinsically Switchable Resonators and Filters," in *Materials Research Society (MRS) XVIII International Materials Research Congress (IMRC)*, Cancun, Mexico, 2009.

S. Lee, **V. Lee**, S. A. Sis, and A. Mortazawi, "A Simple Nonlinear mBVD Model Parameter Extraction Method for Intrinsically Switchable Ferroelectric FBARs," in *Proceedings of the 8th European Microwave Integrated Circuits Conference (EuMIC)*, Nuremberg, Germany, 2013, pp. 1-4.

S. Lee, **V. Lee**, S. A. Sis, and A. Mortazawi, “Linearity Analysis of Intrinsically Switchable Ferroelectric FBAR Filters,” in *IEEE MTT-S International Microwave Symposium Digest*, Seattle, WA, 2013, pp. 1-3.

S. A. Sis, **V. Lee**, S. Lee, and A. Mortazawi, "Intrinsically Switchable Thin Film Ferroelectric Resonators Utilizing Electric Field Induced Piezoelectric Effect," in *IEEE MTT-S International Wireless Symposium Digest*, Beijing, China, 2013, pp. 1-4.

S. Lee, **V. Lee**, S. A. Sis, and A. Mortazawi, "Large signal modeling of switchable ferroelectric FBARs," in *Proceedings of the 7th European Microwave Integrated Circuits Conference (EuMIC)*, 2012, pp. 24-27.

S. A. Sis, **V. Lee**, J. D. Phillips, and A. Mortazawi, "A DC voltage dependent switchable acoustically coupled BAW filter based on BST-on-silicon composite structure," in *IEEE MTT-S International Microwave Symposium Digest*, Montreal, QC, Canada, 2012, pp. 1-3.

S. A. Sis, **V. Lee**, J. D. Phillips, and A. Mortazawi, "Intrinsically switchable thin film ferroelectric resonators," in *IEEE MTT-S International Microwave Symposium Digest*, Montreal, QC, Canada, 2012, pp. 1-3.

S. A. Sis, **V.C. Lee**, and A. Mortazawi, "Intrinsically switchable, BST-on-silicon composite FBARs," in *IEEE MTT-S International Microwave Symposium Digest*, Baltimore, MD, 2011, pp. 1-4.

X. Zhu, **V. Lee**, J. Phillips, and A. Mortazawi, "Intrinsically switchable contour mode acoustic wave resonators based on barium titanate thin films," in *IEEE MTT-S International Microwave Symposium Digest*, Boston, MA, 2009, pp. 93-96.

X. Zhu, J. S. Fu, **V. Lee**, and A. Mortazawi, "Thin Film Ferroelectric Tunable Devices for Reconfigurable Radios," in *Proceedings of the Army Science Conference (26th)*, Orlando, FL. 2008.

# APPENDICES

# Appendix A

# BST Thin Film Resonator and Filter Fabrication Procedure

## A.1 Fabrication Process Overview

1 Wafer preparation and cleaning

2 Bottom electrode deposition/patterning

3 BST thin film deposition using pulsed laser deposition (PLD)

4 Top electrode deposition

5 BST annealing

6 BST etch

7 Compensation layer deposition

8 Thin film resistor deposition

9 Contact deposition

10 Device release

## A.2 Detailed Fabrication Procedures

### A.2.1 Wafer preparation and cleaning

1 Dice a wafer to the desired size using a scribe

2 Blow off any dust or particles that may have gotten onto the wafer from the dicing process with a nitrogen gun

3 Soak the wafer in a beaker of hot acetone for 3 minutes while inside an ultrasonic bath

4 Transfer and soak the wafer in a beaker of hot isopropyl alcohol (IPA) for 3 minutes while inside an ultrasonic bath

5 Blow the IPA off the surfaces of the wafer with a nitrogen gun

6 Bake the wafer at 130 °C for 3 minutes

### A.2.2 Bottom electrode patterning

1 Soak the wafer in a beaker of hot acetone for 3 minutes while inside an ultrasonic bath

2 Transfer and soak the wafer in a beaker of hot IPA for 3 minutes while inside an ultrasonic bath

3 Blow the IPA off the surfaces of the wafer with a nitrogen gun

4 Bake the wafer at 130 °C for 3 minutes

5 Spin HMDS onto the wafer using the CEE 200X PR Spinner at a speed of 4000 RPM

6 Spin SPR 220 3.0 onto the wafer using the CEE 200X PR Spinner at a speed of 3000 RPM

7 Softbake the photoresist at 115 °C for 90 seconds

8 Align the mask and the wafer with the MA/BA-6 Mask/Bond Aligner and expose the photoresist for 6 seconds at an intensity of 20 $mW/cm^2$

9 Post exposure bake the photoresist at 115 °C for 90 seconds

10 Develop the photoresist with the CEE Developer using the 30/30 second double puddle recipe for the AZ726 developer

11 Inspect the photoresist patterning under the optical microscope

12 Descum the surface of the wafer using the March Asher at a pressure of 250 mTorr and a power of 80 W for 60 seconds

13 Pattern the bottom electrode using step a or b

   a. Selectively etch away the blanket platinum bottom electrode layer using the Plasmatherm 790

   b. Deposit 30 nm of titanium and 100 nm of platinum onto the wafer with the Enerjet Evaporator

14 Place the wafer into a beaker of hot acetone for 1 hour

15 Transfer and place the wafer into a beaker of hot IPA for 3 minutes

16 Blow the IPA off the surfaces of the wafer with a nitrogen gun

17 Inspect the surface of the wafer under the optical microscope, clean again if necessary

18 Bake the wafer at 130 °C for 3 minutes

### A.2.3 BST thin film deposition using pulsed laser deposition (PLD)

1 Adhere the wafer onto the stage of the PLD using silver paint

2 Wait for the silver paint to dry

3 Load the substrate assembly into the chamber

4 Switch on the roughing pump

5 Open the gate valve

6 Wait for the chamber pressure to go below 2.5 Torr

7 Switch on the turbomolecular pump

8 Program the temperature controller to increase the temperature of the stage up to 650 °C at a ramp rate of 5 °C/minute

9 Wait until the wafer reached 650 °C

10 Open the flow of ultrahigh purity oxygen into the chamber

11 Turn on the speed controller for the turbomolecular pump

12 Adjust the flow of the oxygen until the partial pressure reaches 300 mTorr

13 Switch on the target rotation motor

14 Turn on the laser

15 Verify the laser is hitting the BST target

16 Wait until the desired film thickness has been obtained

17 Turn off the laser

18 Close the gate valve

19 Switch off the turbomolecular pump

20 Switch off the target rotation motor

21 Wait for the chamber pressure to reach 100 Torr

22 Close the flow of ultrahigh purity oxygen into the chamber

23 Wait one hour

24 Switch off the roughing pump

25 Program the temperature controller to decrease the temperature of the stage down to 25 °C at a ramp rate of 1 °C/minute

26 Wait for the wafer to cool down to 25 °C

27 Vent the chamber using nitrogen

28 Remove the wafer

29 Replace the substrate assembly and pump down the chamber

### A.2.4 Top electrode deposition

1 Soak the wafer in a beaker of hot acetone for 3 minutes while inside an ultrasonic bath

2 Transfer and soak the wafer in a beaker of hot IPA for 3 minutes while inside an ultrasonic bath

3 Blow the IPA off the surfaces of the wafer with a nitrogen gun

4 Bake the wafer at 130 °C for 3 minutes

5 Spin HMDS onto the wafer using the CEE 200X PR Spinner at a speed of 4000 RPM

6 Spin SPR 220 3.0 onto the wafer using the CEE 200X PR Spinner at a speed of 3000 RPM

7 Softbake the photoresist at 115 °C for 90 seconds

8 Align the mask and the wafer with the MA/BA-6 Mask/Bond Aligner and expose the photoresist for 6 seconds at an intensity of 20 $mW/cm^2$

9 Post exposure bake the photoresist at 115 °C for 90 seconds

10 Develop the photoresist with the CEE Developer using the 30/30 second double puddle recipe for the AZ726 developer

11 Inspect the photoresist patterning under the optical microscope

12 Descum the surface of the wafer using the March Asher at a pressure of 250 mTorr and a power of 80 W for 60 seconds

13 Deposit 100 nm of platinum onto the wafer with the Enerjet Evaporator

14 Place the wafer into a beaker of hot acetone for 1 hour

15 Transfer and place the wafer into a beaker of hot IPA for 3 minutes

16 Blow the IPA off the surfaces of the wafer with a nitrogen gun

17 Inspect the surface of the wafer under the optical microscope, clean again if necessary

18 Bake the wafer at 130 °C for 3 minutes

### A.2.5 BST annealing

1 Switch on the furnance

2 Place the wafer into the center of the tube furnace

3 Program the temperature controller to increase the temperature of the furnace up to 500 °C at a ramp rate of 5 °C/minute

4 Open the flow of ultrahigh purity oxygen into the furnace at a rate of 2-3 sccm

5 Wait for 30 minutes

6 Close the flow of oxygen

7 Program the temperature controller to decrease the temperature of the furnace down to 25 °C at a ramp rate of 1 °C/minute

8 Wait until the furnace reaches 25 °C

9 Remove the wafer from the furnace

10 Switch off the furnace

### A.2.6 BST etch

1 Soak the wafer in a beaker of hot acetone for 3 minutes while inside an ultrasonic bath

2 Transfer and soak the wafer in a beaker of hot IPA for 3 minutes while inside an ultrasonic bath

3 Blow the IPA off the surfaces of the wafer with a nitrogen gun

4 Bake the wafer at 130 °C for 3 minutes

5 Spin HMDS onto the wafer using the CEE 200X PR Spinner at a speed of 4000 RPM

6 Spin SPR 220 3.0 onto the wafer using the CEE 200X PR Spinner at a speed of 3000 RPM

7 Softbake the photoresist at 115 °C for 90 seconds

8 Align the mask and the wafer with the MA/BA-6 Mask/Bond Aligner and expose the photoresist for 6 seconds at an intensity of 20 $mW/cm^2$

9 Post exposure bake the photoresist at 115 °C for 90 seconds

10 Develop the photoresist with the CEE Developer using the 30/30 second double puddle recipe for the AZ726 developer

11 Inspect the photoresist patterning under the optical microscope

12 Descum the surface of the wafer using the March Asher at a pressure of 250 mTorr and a power of 80 W for 60 seconds

13 Pattern the BST by using step a or b

a. Soak the wafer in a beaker of diluted BHF and rinse in DI water

b. Mount the wafer onto a 6” carrier wafer with Crystalbond and etch the BST with the LAM 9400 using a recipe with an $Cl_2$-Ar chemistry

14 Place the wafer into a beaker of hot acetone for 1 hour

15 Transfer and place the wafer into a beaker of hot IPA for 3 minutes

16 Blow the IPA off the surfaces of the wafer with a nitrogen gun

17 Inspect the surface of the wafer under the optical microscope, clean again if necessary

18 Bake the wafer at 130 °C for 3 minutes

### A.2.7 Compensation layer deposition

1 Soak the wafer in a beaker of hot acetone for 3 minutes while inside an ultrasonic bath

2 Transfer and soak the wafer in a beaker of hot IPA for 3 minutes while inside an ultrasonic bath

3 Blow the IPA off the surfaces of the wafer with a nitrogen gun

4 Bake the wafer at 130 °C for 3 minutes

5 Spin HMDS onto the wafer using the CEE 200X PR Spinner at a speed of 4000 RPM

6 Spin SPR 220 3.0 onto the wafer using the CEE 200X PR Spinner at a speed of 3000 RPM

7 Softbake the photoresist at 115 °C for 90 seconds

8 Align the mask and the wafer with the MA/BA-6 Mask/Bond Aligner and expose the photoresist for 6 seconds at an intensity of 20 $mW/cm^2$

9 Post exposure bake the photoresist at 115 °C for 90 seconds

10 Develop the photoresist with the CEE Developer using the 30/30 second double puddle recipe for the AZ726 developer

11 Inspect the photoresist patterning under the optical microscope

12 Descum the surface of the wafer using the March Asher at a pressure of 250 mTorr and a power of 80 W for 60 seconds

13 Deposit the desired amount of gold onto the wafer with the Enerjet Evaporator

14 Place the wafer into a beaker of hot acetone for 1 hour

15 Transfer and place the wafer into a beaker of hot IPA for 3 minutes

16 Blow the IPA off the surfaces of the wafer with a nitrogen gun

17 Inspect the surface of the wafer under the optical microscope, clean again if necessary

18 Bake the wafer at 130 °C for 3 minutes

### A.2.8 Thin film resistor deposition

1 Soak the wafer in a beaker of hot acetone for 3 minutes while inside an ultrasonic bath

2 Transfer and soak the wafer in a beaker of hot IPA for 3 minutes while inside an ultrasonic bath

3 Blow the IPA off the surfaces of the wafer with a nitrogen gun

4 Bake the wafer at 130 °C for 3 minutes

5 Spin HMDS onto the wafer using the CEE 200X PR Spinner at a speed of 4000 RPM

6 Spin SPR 220 3.0 onto the wafer using the CEE 200X PR Spinner at a speed of 3000 RPM

7 Softbake the photoresist at 115 °C for 90 seconds

8 Align the mask and the wafer with the MA/BA-6 Mask/Bond Aligner and expose the photoresist for 6 seconds at an intensity of 20 $mW/cm^2$

9 Post exposure bake the photoresist at 115 °C for 90 seconds

10 Develop the photoresist with the CEE Developer using the 30/30 second double puddle recipe for the AZ726 developer

11 Inspect the photoresist patterning under the optical microscope

12 Descum the surface of the wafer using the March Asher at a pressure of 250 mTorr and a power of 80 W for 60 seconds

13 Deposit 30 nm of nickel-chromium onto the wafer with the Cooke Evaporator

14 Place the wafer into a beaker of hot acetone for 1 hour

15 Transfer and place the wafer into a beaker of hot IPA for 3 minutes

16 Blow the IPA off the surfaces of the wafer with a nitrogen gun

17 Inspect the surface of the wafer under the optical microscope, clean again if necessary

18 Bake the wafer at 130 °C for 3 minutes

### A.2.9 Contact deposition

1 Soak the wafer in a beaker of hot acetone for 3 minutes while inside an ultrasonic bath

2 Transfer and soak the wafer in a beaker of hot IPA for 3 minutes while inside an ultrasonic bath

3 Blow the IPA off the surfaces of the wafer with a nitrogen gun

4 Bake the wafer at 130 °C for 3 minutes

5 Spin HMDS onto the wafer using the CEE 200X PR Spinner at a speed of 4000 RPM

6 Spin SPR 220 3.0 onto the wafer using the CEE 200X PR Spinner at a speed of 3000 RPM

7 Softbake the photoresist at 115 °C for 90 seconds

8 Align the mask and the wafer with the MA/BA-6 Mask/Bond Aligner and expose the photoresist for 6 seconds at an intensity of 20 $mW/cm^2$

9 Post exposure bake the photoresist at 115 °C for 90 seconds

10 Develop the photoresist with the CEE Developer using the 30/30 second double puddle recipe for the AZ726 developer

11 Inspect the photoresist patterning under the optical microscope

12 Descum the surface of the wafer using the March Asher at a pressure of 250 mTorr and a power of 80 W for 60 seconds

13 Deposit 50 nm of titanium, 1.5 μm of aluminum, 50 nm of titanium, and 500 nm of gold onto the wafer with the Enerjet Evaporator

14 Place the wafer into a beaker of hot acetone for 1 hour

15 Transfer and place the wafer into a beaker of hot IPA for 3 minutes

16 Blow the IPA off the surfaces of the wafer with a nitrogen gun

17 Inspect the surface of the wafer under the optical microscope, clean again if necessary

18 Bake the wafer at 130 °C for 3 minutes

### A.2.10 Device release

1 Soak the wafer in a beaker of hot acetone for 3 minutes while inside an ultrasonic bath

2 Transfer and soak the wafer in a beaker of hot IPA for 3 minutes while inside an ultrasonic bath

3 Blow the IPA off the surfaces of the wafer with a nitrogen gun

4 Bake the wafer at 130 °C for 3 minutes

5 Spin HMDS onto the wafer using the CEE 200X PR Spinner at a speed of 4000 RPM

6 Spin SPR 220 3.0 onto the wafer using the CEE 200X PR Spinner at a speed of 5000 RPM

7 Bake the photoresist at 115 °C for 130 seconds

8 Spin HMDS onto the back of the wafer using the CEE 200X PR Spinner at a speed of 4000 RPM

9 Spin SPR 220 3.0 onto the back of the wafer using the CEE 200X PR Spinner at a speed of 2500 RPM

10 Softbake the photoresist at 115 °C for 90 seconds

11 Align the mask and the backside of the wafer with the MA/BA-6 Mask/Bond Aligner and expose the photoresist for 6 seconds at an intensity of 20 $mW/cm^2$

12 Post exposure bake the photoresist at 115 °C for 90 seconds

13 Develop the photoresist with the CEE Developer using the 30/30 second double puddle recipe for the AZ726 developer

14 Inspect the photoresist patterning under the optical microscope

15 Strip the photoresist from the front of the wafer by spinning the wafer using the CEE 200X PR Spinner at a speed of 5000 RPM and spraying acetone onto the wafer

16 Descum the back of the wafer using the March Asher at a pressure of 250 mTorr and a power of 80 W for 60 seconds

17 Mount the wafer face down on a 4" or 6" oxidize silicon carrier wafer using Crystalbond

18 Selectively etch away the silicon wafer with the STS Pegasus 4 or 6

19 Measure the depth of the trench to make sure the silicon has been etched away with the Zygo NewView 5000

20 Unmount the wafer from the carrier wafer

21 Place the wafer into a beaker of hot acetone for 1 hour

22 Transfer and place the wafer into a beaker of hot IPA for 3 minutes

23 Gently blow the IPA off the surfaces of the wafer with a nitrogen gun

24 Inspect the surface of the wafer under the optical microscope, clean again if necessary

25 Bake the wafer at 130 °C for 3 minutes

# Appendix B

# RF Magnetron Sputtering System - Standard Operating Procedures

## B.1 Initializing the System

1. Make sure both water filters are “clean”
2. Open the building water valves (both source (S) and return (R)) going to and from the water chiller
3. Make sure there is enough DI water in the reservoir of the water chiller (> 50%) of the gauge on the side
    a. If there is not enough water
        i. Remove the lid of the water chiller
        ii. Add DI water obtained from the cleanroom staff
        iii. Replace the lid of the water chiller
4. Switch on the water chiller
5. Turn on roughing pump
6. Open the valve connecting the roughing pump to the cryogenic pump
7. Wait for roughing pump pressure gauge to read < 50 mTorr
8. Close the valve connecting the roughing pump to the cryogenic pump

9 Make sure the main processing chamber is below 50 mTorr

a. If the pressure is too high

b. Open the valve connecting the roughing pump to the load lock

c. Open the gate valve connecting the load lock to the main chamber

d. Wait until the pressure of the main chamber is < 50 mTorr

e. Close the gate valve connecting the load lock to the main chamber

f. Close the valve connecting the roughing pump to the load lock

10 Turn off the roughing pump

11 Make sure the cryogenic pump temperature gauge is on (should read below 300 K)

12 Make sure the cryogenic pump has adequate water flow (> 0.5 gpm)

13 Turn on the cryogenic pump compressor

14 Make sure the water chiller is being properly cooled

a. When the compressor is running, the head pressure should never exceed 500 psi

i. If this is the case, the compressor will automatically shut off

ii. If this is the case, most likely the building water valves are not both opened

b. The compressor should only be on for several minutes at a time and the refrigerant head pressure should not exceed 300 psi

c. If the compressor is running for > 3 minutes at a time, check the water filter and make sure it is clean

15 Make sure the water chiller is properly chilling the circulating water

16 The temperature reading on the cryogenic pump temperature gauge should start to decrease and after roughly 2 – 3 hours, will reach 11 K

17 Open the gate valve connecting the cryogenic pump to the main processing chamber

## B.2 Running the System

(M) = Manual procedure

(C) = Computer controlled procedure

### B.2.1 Sample Loading

1 Isolate cryopump from main chamber (C)

2 Vent load-lock (C)

3 Open load-lock door (M)

4 Turn off nitrogen (C)

5 Take out sample holder (M)

6 Put sample on holder (M)

7 Put sample holder back in load-lock (M)

8 Close load-lock door and use the thumb-screw to seal the door shut (M)

9 Rough out load-lock to < 50 mTorr

a. Turn on roughing pump (M)

b. Open valve connecting load-lock to roughing pump (M)

c. Wait until load-lock pressure reading is < 50 mTorr (C)

d. Close valve connecting load-lock to roughing pump (M)

e. Turn off roughing pump (M)

f. Loosen the thumb-screw and rotate out of position (M)

10 Lower heater (M)

11 Open gate valve connecting load-lock to main chamber (M)

12 Gently slide transfer arm to move sample holder over heater (M)

13 Slowly raise heater until sample holder is resting on heater (M)

14 Slowly rotate the heater in the unlock direction to disengage the sample holder from the loading arm (M)

15 Move the transfer arm back into the load-lock (M)

16 Close the gate valve between the load-lock and the chamber (M)

17 Open the nitrogen gas cylinder (M)

18 Open gate valve connecting cryopump to main chamber (C)

## B.2.2 Film Deposition

1 Wait for the chamber to reach the desired base pressure (for high tunability optimized conditions < 5×10-8 Torr) (M)

2 Turn on sample rotation (usually 10-20 rpm) (M)

3 Close substrate shutter (C)

4 Adjust the heater height to the 0.8” mark (so sample is just below substrate shutter) (M)

5 Make sure sputtering guns and substrate heater are adequately cooled (M)

a. Turn on secondary water pump (M)

b. Check to see water flow is > 0.5 gpm for both sputtering guns (M)

c. Check to see water flow is > 0 gpm for the substrate heater (M)

6 Set the heater ramp rate (20 ºC/min is relatively conservative, good for dissimilar materials) (M)

7 Set the desired temperature (M)

8 When the sample reaches 300 ºC, start the gas flow

a. Turn on “Power” (pulling and moving up)

b. Set mass flow controller (MFCs) to 75 sccm for argon and 25 sccm for oxygen (M)

c. Open the argon and oxygen gas cylinders (M)

d. Switch on the argon mass flow controller (M)

e. Open the argon valve (C)

f. Switch on the oxygen mass flow controller (M)

g. Open the oxygen valve (C)

h. Set gate valve between the chamber and the cryopump to its 3rd position (C)

9 Adjust the partial pressure to 45 mTorr by using the pressure regulator on the gate valve (M)

10 Turn on the power to the sputter gun power supply and automatic matching network controllers for both guns, set to automatic (M)

a. Press the power button on each unit (M)

b. Turn on the ramp mode for the power supply (M)

c. Set the turn on and turn off time so that the power ramps up and down at 20 W/min (M) EX) It will take15 min to reach 300 W. So, it needs to start at temp=350 deg when 650 deg maximum.

11 Set the RF sputtering gun power supplies to 300 W (M)

12 Turn on the “RF” output (M)

13 Check and make sure the plasma ignites (M)

14 Check and make sure the sample is still on the sample holder (M)

15 Open the shutter (C) after ensuring the stage height is correct.

16 Start your timer quickly (M)

17 Mid-way through the deposition record the load and tune values of the automatic matching network (M)

18 When your timer goes off, close the shutter (C)

19 Turn off the “RF” output (M)

20 Set the heater ramp rate (if ramp up and ramp down rates are different) (M)

21 Set the desired temperature to 25 ºC

22 Wait until RF output power reaches 0 W

23 Turn off the gases

a. Close the argon and oxygen valves (M)

b. Turn off the argon and oxygen flow at the mass flow controller (C)

c. Close the argon and oxygen cylinders (M)

d. Turn off “Power” (M)

24 Turn off the power supplies (M)

25 Turn off the automatic matching network controllers (M)

26 Turn off secondary water pump (M)

27 Open the gate valve between the chamber and the cryopump, turn off relay 6 (C)

28 Below 200 C, turn off rotation (M)

29 Turn off substrate heater power supply and controller (M)

### B.2.3 Sample unloading

1 Make sure rotation is off (M)

2 Lower substrate heater assembly (M)

3 Rough out load-lock to < 50 mTorr (M)

4 Open gate valve between load-lock and main chamber (M)

5 Slide transfer arm into chamber (M)

6 Adjust heater height to match transfer arm (M)

7 Rotate in lock direction to attach sample holder to transfer arm (M)

8 Lower heater (M)

9 Move transfer arm back into load-lock (M)

10 Close gate valve between load-lock and chamber (M)

11 Open door to load-lock (M)

12 Flow nitrogen to vent load-lock (C)

13 Take out sample holder (M)

14 Remove sample (M)

15 Replace sample holder (M)

16 Turn off nitrogen (M)

17 Close door to load-lock (M)

18 Rough out load lock to 50 mTorr (M)

# Appendix C

# MATLAB Code

## C.1 Acoustic Wave Transmission Line Model

```
%% Resonator Design
*******************************************************
% Instructions
% Set freq_sweep
clear
clc
close all
freq_sweep = linspace(100e6, 5e9, 3201);
material_data

%% Plot Options
*************************************************************
x_label = 'Frequency (GHz)';
freq_sweep_plot = freq_sweep/1e9;

%% REFLECTIVITY OF DIFFERENT BRAGG REFLECTORS
*****************************

N = input('Choose the number of repeated pairs of low/high refractive
index material : ');

%v Bragg Reflector on Sapphire Substrate (Sapphire -> Pt -> SiO2 -> (Pt
-> SiO2) x (N number of pairs - 1))
% Z_S = AZ_S; % Sapphire substrate
Z_S = AZ_air; % Air substrate
% Z_S = AZ_S.*(AZ_air + AZ_S.*tanh(gamma_S.*t_S))./(AZ_S +
AZ_air.*tanh(gamma_S.*t_S));

Z_Pt = AZ_Pt.*(Z_S + AZ_Pt.*tanh(gamma_Pt.*t_Pt(1)))./(AZ_Pt +
Z_S.*tanh(gamma_Pt.*t_Pt(1)));
Z_SiO2 = AZ_SiO2.*(Z_Pt +
AZ_SiO2.*tanh(gamma_SiO2.*t_SiO2(1)))./(AZ_SiO2 +
Z_Pt.*tanh(gamma_SiO2.*t_SiO2(1)));

for i = 1:N-1
```

```
    Z_Pt = AZ_Pt.*(Z_SiO2 + AZ_Pt.*tanh(gamma_Pt.*t_Pt(i+1))).(AZ_Pt +
Z_SiO2.*tanh(gamma_Pt.*t_Pt(i+1)));
    Z_SiO2 = AZ_SiO2.*(Z_Pt +
AZ_SiO2.*tanh(gamma_SiO2.*t_SiO2(i+1))).(AZ_SiO2 +
Z_Pt.*tanh(gamma_SiO2.*t_SiO2(i+1)));
end
Z_reflector = Z_SiO2;

reflectivity = abs((Z_reflector - AZ_BTO).(Z_reflector + AZ_BTO));
transmittivity = 1 - reflectivity;

figure(1);
[haxes, h1, h2] = plotyy(freq_sweep_plot, reflectivity*100,
freq_sweep_plot, 10*log10(transmittivity));
title(strcat([num2str(N), ' pair Bragg Reflector Reflectivity and
Transmittivity vs Frequency for BTO']));
xlabel('Frequency (GHz)');
set(get(haxes(1),'Ylabel'),'String','Reflectivity (%)');
set(get(haxes(2),'Ylabel'),'String','Transmittivity (%)');

[max_reflectivity, max_index] = max(reflectivity);

disp(strcat(['Max reflectivity at ',
num2str(freq_sweep(max_index)/1e9), ' GHz with a value of ',
num2str(max_reflectivity)], ' with ', num2str(N), ' pairs'));

%% Acoustic Wave Transmission Line Model
*********************************

n = 1; % Number of FBARs
L_s = 0.01e-9; % [Henry] wirebond inductance

phi_BTO = -1i.*gamma_BTO.*t_BTO/2;

% Zl is defined as a load (air) seen through a transmission line
(Platinum) of length t_top_Pt and acoustic impedance of AZ_Pt
% Top electrodes Zl: Air --> Pt

% Platinum Top Electrode
Zl = AZ_Pt.*(AZ_air + AZ_Pt.*tanh(gamma_Pt.*t_top_Pt)).(AZ_Pt +
AZ_air.*tanh(gamma_Pt.*t_top_Pt));

% Aluminum Top Electrode
% Zl = AZ_Al.*(AZ_air + AZ_Al.*tanh(gamma_Al.*t_top_Al)).(AZ_Al +
AZ_air.*tanh(gamma_Al.*t_top_Al));

% Aluminum Compensation Layer On Top of Platinum Top Electrode
% Z_comp = AZ_Al.*(AZ_air + AZ_Al.*tanh(gamma_Al.*t_comp_Al)).(AZ_Al +
AZ_air.*tanh(gamma_Al.*t_comp_Al));
% Zl = AZ_Pt.*(Z_comp + AZ_Pt.*tanh(gamma_Pt.*t_top_Pt)).(AZ_Pt +
Z_comp.*tanh(gamma_Pt.*t_top_Pt));

% % Gold Compensation Layer On Top of Platinum Top Electrode
```

```
% Z_comp = AZ_Au.*(AZ_air + AZ_Au.*tanh(gamma_Au.*t_comp1_Au))./(AZ_Au
+ AZ_air.*tanh(gamma_Au.*t_comp1_Au));
% Zl = AZ_Pt.*(Z_comp + AZ_Pt.*tanh(gamma_Pt.*t_top_Pt))./(AZ_Pt +
Z_comp.*tanh(gamma_Pt.*t_top_Pt));

% % Bragg Reflector Top Electrode (Air -> Pt -> SiO2 -> (Pt -> SiO2) x
(N number of pairs - 1) - SiO2)
% % Example: If N = 4, then the stack is Air -> Pt -> SiO2 -> Pt
% Zl = Z_Pt;

% Zr is defined as a load (Sapphire Substrate) seen through a Bragg
Reflector and a transmission line (Platinum) of length t_bot_Pt and
acoustice impedance of AZ_Pt
% Bottom electrodes Zr: Sapphire --> Pt

% % SMR BOTTOM
% Zr = AZ_Pt.*(Z_reflector+ AZ_Pt.*tanh(gamma_Pt.*t_bot_Pt))./(AZ_Pt +
Z_reflector.*tanh(gamma_Pt.*t_bot_Pt));
% FBAR BOTTOM
Zr = AZ_Pt.*(AZ_air + AZ_Pt.*tanh(gamma_Pt.*t_bot_Pt))./(AZ_Pt +
AZ_air.*tanh(gamma_Pt.*t_bot_Pt));
% % FBAR BOTTOM WITH SIO2
% Z_SiO2 = AZ_SiO2.*(AZ_air +
AZ_SiO2.*tanh(gamma_SiO2.*t_bot_SiO2))./(AZ_SiO2 +
AZ_air.*tanh(gamma_SiO2.*t_bot_SiO2));
% Z_TiO2 = AZ_TiO2.*(AZ_SiO2 +
AZ_TiO2.*tanh(gamma_TiO2.*t_TiO2))./(AZ_TiO2 +
AZ_SiO2.*tanh(gamma_TiO2.*t_TiO2));
% Zin_1 = Z_SiO2;
% Zr = AZ_Pt.*(Zin_1 + AZ_Pt.*tanh(gamma_Pt.*t_bot_Pt))./(AZ_Pt +
Zin_1.*tanh(gamma_Pt.*t_bot_Pt));
% Zin_2 = Zr;
% % FBAR BOTTOM WITH Silicon-on-insulator
% Z_Si = AZ_Si.*(AZ_air + AZ_Si.*tanh(gamma_Si.*t_Si_SOI))./(AZ_Si +
AZ_air.*tanh(gamma_Si.*t_Si_SOI));
% Z_SiO2 = AZ_SiO2.*(Z_Si +
AZ_SiO2.*tanh(gamma_SiO2.*t_bot_SiO2))./(AZ_SiO2 +
Z_Si.*tanh(gamma_SiO2.*t_bot_SiO2));
% Zr = AZ_Pt.*(Z_SiO2 + AZ_Pt.*tanh(gamma_Pt.*t_bot_Pt))./(AZ_Pt +
Z_SiO2.*tanh(gamma_Pt.*t_bot_Pt));
% % FBAR BOTTOM WITH Silicon-on-insulator and residual SiO2
% t_residual_SiO2 = 0.5e-6;
% Z_residual_SiO2 = AZ_SiO2.*(AZ_air +
AZ_SiO2.*tanh(gamma_SiO2.*t_residual_SiO2))./(AZ_SiO2 +
AZ_air.*tanh(gamma_SiO2.*t_residual_SiO2));
% Z_Si = AZ_Si.*(Z_residual_SiO2 +
AZ_Si.*tanh(gamma_Si.*t_Si_SOI))./(AZ_Si +
Z_residual_SiO2.*tanh(gamma_Si.*t_Si_SOI));
% Z_SiO2 = AZ_SiO2.*(Z_Si +
AZ_SiO2.*tanh(gamma_SiO2.*t_bot_SiO2))./(AZ_SiO2 +
Z_Si.*tanh(gamma_SiO2.*t_bot_SiO2));
% Zr = AZ_Pt.*(Z_SiO2 + AZ_Pt.*tanh(gamma_Pt.*t_bot_Pt))./(AZ_Pt +
Z_SiO2.*tanh(gamma_Pt.*t_bot_Pt));


% Zin of the device
```

```
Area = 10e-6*10e-6;
% % STO
% C_E = E0*EC_STO*Area/t_STO;
% BTO
C_E_on = E0*EC_BTO_on*Area/t_BTO;
C_E_off = E0*EC_BTO_off*Area/t_BTO;

% STO
% zl = Zl./AZ_STO;
% zr = Zr./AZ_STO;
% BTO
zl = Zl./AZ_BTO;
zr = Zr./AZ_BTO;

K2= 0.075;

% STO
% Zin = 1./j./2./pi./freq_sweep./C_E.*(1 - K2.*tan(phi_STO)./phi_STO.*
((zl+zr).*cos(phi_STO).*cos(phi_STO) +
j.*sin(2.*phi_STO))./((zl+zr).*cos(2.*phi_STO) +
j.*(zl.*zr+1).*sin(2.*phi_STO)));
% BST
%Zin = 1./j./2./pi./freq_sweep./C_E.*(1 - K2.*tan(phi_BST)./phi_BST.*
((zl+zr).*cos(phi_BST).*cos(phi_BST) +
j.*sin(2.*phi_BST))./((zl+zr).*cos(2.*phi_BST) +
j.*(zl.*zr+1).*sin(2.*phi_BST)));
% BTO
Zin = 1./j./2./pi./freq_sweep./(C_E_on*(1)).*(1 -
K2.*tan(phi_BTO)./phi_BTO.* ((zl+zr).*cos(phi_BTO).*cos(phi_BTO) +
j.*sin(2.*phi_BTO))./((zl+zr).*cos(2.*phi_BTO) +
j.*(zl.*zr+1).*sin(2.*phi_BTO)));

% % FBAR BANK
% % Capacitance of off devices
% Zin = Zin + (1./(1i*2*pi*freq_sweep.*C_E_off/(n-1)));

% Contribution of metallization
Z_metallization = 1.9;

Zin = Zin + Z_metallization;

% Contribution of parasitic inductance
Z_inductance = 1i*2*pi.*freq_sweep*L_s;
Zin = Zin + Z_inductance;

Capacitance = -1./imag(Zin)./2./pi./freq_sweep;

Losstangent = -1.*real(Zin)./imag(Zin);
Zin_modulus = abs(Zin);

BE_impedance = 1;
if (BE_impedance == 1)
    figure(1);
    gamma = (Zr-AZ_BTO)./(Zr+AZ_BTO);
    s_vec(1, 1, :) = gamma;
```

```
    data = rfdata.data('Z0', 50, 'S_Parameters', ...
        s_vec, 'Freq', freq_sweep_plot);
    smith(data, 's11');
    plot(freq_sweep_plot, abs(gamma));
end

quarter_wavelength = 0;
if (quarter_wavelength == 1)
    figure(2);
    subplot(4, 1, 1);
    plot(freq_sweep_plot, (wavelength_Pt./4).*10^9);
    title('Platinum Thickness for Bragg Reflector vs Resonant
Frequency');
    xlabel(x_label);
    ylabel('Platinum Thickness (nm)');
    grid on;

    %  subplot(4, 1, 1);
    %  plot(freq_sweep_plot, (wavelength_W./4).*10^9);
    %  title('Tungsten Thickness for Bragg Reflector vs Resonant
Frequency');
    %  xlabel(x_label);
    %  ylabel('Tungsten Thickness (nm)');
    %  grid on;

    % subplot(3, 1, 1);
    % plot(freq_sweep_plot, (wavelength_ALN./4).*10^9);
    % title('Aluminum Nitride Thickness for Bragg Reflector vs Resonant
Frequency');
    % xlabel(x_label);
    % ylabel('Aluminum Nitride Thickness (nm)');
    % grid on;

    subplot(4, 1, 2);
    plot(freq_sweep_plot, (wavelength_SiO2./4).*10^9);
    title('SiO_2 Thickness for Bragg Reflector vs Resonant Frequency');
    xlabel(x_label);
    ylabel('SiO_2 Thickness (nm)');
    grid on;

    subplot(4, 1, 3);
    plot(freq_sweep_plot, (wavelength_S./4).*10^9);
    title('Sapphire Thickness for Bragg Reflector vs Resonant
Frequency');
    xlabel(x_label);
    ylabel('Sapphire Thickness (nm)');
    grid on;

    subplot(4, 1, 3);
    plot(freq_sweep_plot, (wavelength_BTO./2).*10^9);
    title('BTO for Bragg Reflector vs Resonant Frequency');
    xlabel(x_label);
    ylabel('BTO (nm)');
    grid on;
```

```
    subplot(4, 1, 4);
    plot(freq_sweep_plot, (wavelength_STO./2).*10^9);
    title('STO for Bragg Reflector vs Resonant Frequency');
    xlabel(x_label);
    ylabel('STO (nm)');
    grid on;
end

plot_1 = 1;
if (plot_1 == 1)
    figure(11);
    subplot(3,1,1);
    plot(freq_sweep_plot, Capacitance/1e-12);
    title('STO FBAR Capacitance');
    xlabel(x_label);
    ylabel('Capacitance (pF)');
    grid on;
    % axis([1.06e9 1.14e9 -4e-12 4e-12]);

    subplot(3,1,2);
    plot(freq_sweep_plot, Losstangent);
    title('STO FBAR Loss Tangent');
    xlabel(x_label);
    ylabel('Loss Tangent');
    grid on;

    subplot(3,1,3);
    semilogy(freq_sweep_plot, Zin_modulus);
    title('STO FBAR Zin Impedance');
    xlabel(x_label);

    ylabel('|Zin| (Ohms)');
    grid on;
end

plot_2 = 0;
if (plot_2 == 1)
    figure(12);
    plot(freq_sweep_plot, real(Zin), freq_sweep_plot, imag(Zin),'-');
    title('Real and Imaginary (-) Impedances vs. Frequency');
    xlabel(x_label);
    ylabel('Real and Imaginary Impedance (Ohms)');
    grid on;
end

Z0 = 50;
S11 = (Zin - Z0)./(Zin + Z0);
S11_mag = abs(S11);
% S11_phase = atan(imag(S11)./real(S11));
S11_phase = angle(S11);

plot_3 = 1;
if (plot_3 == 1)
    figure(13);
```

```
    subplot(2,1,1);
    plot(freq_sweep_plot, 20*log10(S11_mag));
    title('STO FBAR S11 Magnitude in dB');
    xlabel(x_label);
    ylabel('|S11| (dB)');
    grid on;

    subplot(2,1,2);
    plot(freq_sweep_plot, S11_phase*180/pi);
    title('STO FBAR S11 Phase');
    xlabel(x_label);
    ylabel('Phase(S11)');
    grid on;
end

plot_4 = 1;
if (plot_4 == 1)
    figure(14);
    s_vec(1, 1, :) = S11;

    data = rfdata.data('Z0', 50, 'S_Parameters', ...
    s_vec, 'Freq', freq_sweep);
    smith(data, 's11');
%     smithchart(S11);
    title('STO FBAR S11');

    [Zs,Is]=min(Zin_modulus)
    fs = freq_sweep(Is)
    [Zp,Ip]=max(Zin_modulus)
    fp = freq_sweep(Ip)
    Kt_eff = pi/2*fs/fp*tan(pi/2*(fp-fs)/fp)

    Zin_angle = angle(Zin);
    group_delay = abs(gradient(Zin_angle)./gradient(freq_sweep));
    Q = freq_sweep./2.*group_delay;
    Q2 = -
2.*pi.*freq_sweep.*gradient(unwrap(S11_phase))./gradient(2.*pi.*freq_sw
eep).*S11_mag./(1-S11_mag.*S11_mag);
    Qs = Q(Is)
    Qp = -Q(Ip)
end

plot_5 = 1;
if (plot_5 == 1)
    figure(20);
    subplot(2, 1, 1);
    plot(freq_sweep_plot, Q);%, freq_sweep, Q2);
    title('Q & Q vs. Frequency');
    xlabel(x_label);
    ylabel('Q');
    grid on;
end

bwr = (fp-fs)/fp
C = real(C_E_on)
```

```
Co = C*2/(2+bwr)
Ca = C*2*bwr
La = 1/(2*pi*fs)^2/Ca
Ra = 2*pi*fs*La/Qs

Zin_fit = 1./(j.*2.*pi.*freq_sweep.*Co + 1./(Ra +
j.*2.*pi.*freq_sweep.*La - j./2./pi./freq_sweep./Ca));
% figure(15);
% subplot(2,1,1);
% plot(freq_sweep_plot, real(Zin), freq_sweep_plot, real(Zin_fit));
% subplot(2,1,2);
% plot(freq_sweep_plot, imag(Zin), freq_sweep_plot, imag(Zin_fit));
%
% figure(16);
% semilogy(freq_sweep_plot, Zin_modulus, freq_sweep_plot,
abs(Zin_fit));
% grid on;
% [Zs_fit,Is_fit]=min(abs(Zin_fit))
% fs_fit = freq_sweep(Is_fit)
% [Zp_fit,Ip_fit]=max(abs(Zin_fit))
% fp_fit = freq_sweep(Ip_fit)

% load BSTFBARZin.txt;
% Zin_measure = BSTFBARZin(:,2)+j.*BSTFBARZin(:,3);
% figure(7);
% semilogy(f,abs(Zin+2),f,abs(Zin_measure));
%
% Zin_angle_measure = angle(Zin_measure);
% group_delay_measure = gradient(abs(Zin_angle_measure'))./gradient(f);
% Q_measure = f./2.*group_delay_measure;
% figure(8);
% plot(f,Q_measure,f,Q);

%%% Plot of Modeled vs. Measured

comparison = 1;
if (comparison == 1)
    measurement_file = '';
    Measured_Device = read(rfdata.data, measurement_file);

    Measured_Device_S11 = Measured_Device.S_Parameters(:);
    Measured_Device_Zin = 50*(1+Measured_Device_S11)./(1-
Measured_Device_S11);
    Zin_mag = abs(Measured_Device_Zin);

    figure(13);
    subplot(2, 1, 1);
    hold on;
    plot(Measured_Device.Freq()/1e9,
20*log10(abs(Measured_Device_S11)), 'color', [1 0 0]);
    hold off;

    figure(14)
    hold on;
```

```
    s_vec2(1, 1, :) = Measured_Device_S11;

    data = rfdata.data('Z0', 50, 'S_Parameters', ...
    s_vec2, 'Freq', Measured_Device.Freq());
    hsm = smith(data, 's11');
    set(hsm, 'Color', [1 0 0]);
    hold off;

    Zin_angle = angle(Measured_Device_Zin);
    group_delay =
abs(gradient(Zin_angle)./gradient(Measured_Device.Freq()));
    Q = Measured_Device.Freq()./2.*group_delay;
    figure(20);
    subplot(2, 1, 2);
    hold on;
    plot(Measured_Device.Freq()/1e9, Q, 'Color', [1 0 0]);
    length(Measured_Device.Freq()/1e9)
    length(Q)
    hold off;
end
```

# BIBLIOGRAPHY

# BIBLIOGRAPHY


[1] G. M. Rebeiz, K. Entesari, I. Reines, S. J. Park, M. A. El-Tanani, A. Grichener, *et al.*, "Tuning in to RF MEMS," *Microwave Magazine, IEEE*, vol. 10, pp. 55-72, 2009.

[2] B. Sanou, "The World in 2013: ICT Facts and Figures," *International Telecommunications Union*, 2013.

[3] J.-E. Mueller, T. Bruder, P. Herrero, N. Norholm, P. Olesen, J. Rizk, *et al.*, "Requirements for reconfigurable 4G front-ends," in *Microwave Symposium Digest (IMS), 2013 IEEE MTT-S International*, 2013, pp. 1-4.

[4] R. Vazny, H. Pretl, L. Maurer, and R. Weigel, "Front-end implications to multi-standard cellular radios: State-of-the-art and future trends," in *Ultrasonics Symposium (IUS), 2010 IEEE*, 2010, pp. 95-98.

[5] C. Chee-Yee and S. P. Kumar, "Sensor networks: evolution, opportunities, and challenges," *Proceedings of the IEEE*, vol. 91, pp. 1247-1256, 2003.

[6] V. C. Gungor and G. P. Hancke, "Industrial Wireless Sensor Networks: Challenges, Design Principles, and Technical Approaches," *Industrial Electronics, IEEE Transactions on*, vol. 56, pp. 4258-4265, 2009.

[7] Intel. (2013). *Slim Modem for LTE Smartphones, Data Cards, and M2M Apps*. Available: http://www.intel.com/content/www/us/en/wireless-products/mobile-communications/mobile-xmm-7160-1-brief.html

[8] Broadcom. (2013). *4G LTE Advanced FDD and TDD; 3G HSPA+ and TD-SCDMA; 2G-EDGE Modem with Integrated World-Band Radio*. Available: http://www.broadcom.com/products/Cellular/4G-Baseband-Processors/BCM21892

[9] Qualcomm. (2013). *Qualcomm RF360 Front End Solution Enables Single, Global LTE Design for Next-Generation Mobile Devices*. Available: http://www.qualcomm.com/media/releases/2013/02/21/qualcomm-rf360-front-end-solution-enables-single-global-lte-design-next

[10] J. R. Clark, H. Wan-Thai, M. A. Abdelmoneum, and C. T. C. Nguyen, "High-Q UHF micromechanical radial-contour mode disk resonators," *Microelectromechanical Systems, Journal of*, vol. 14, pp. 1298-1310, 2005.

[11] L. Sheng-Shian, L. Yu-Wei, R. Zeying, and C. T. C. Nguyen, "Self-switching vibrating micromechanical filter bank," in *Frequency Control Symposium and Exposition, 2005. Proceedings of the 2005 IEEE International*, 2005, p. 7 pp.

[12] H. Chandrahalim and S. A. Bhave, "Digitally-tunable mems filter using mechanically-coupled resonator array," in *Micro Electro Mechanical Systems, 2008. MEMS 2008. IEEE 21st International Conference on*, 2008, pp. 1020-1023.

[13] N. Sinha, R. Mahameed, Z. Chengjie, and G. Piazza, "Integration of AlN micromechanical contour-mode technology filters with three-finger dual beam AlN

MEMS switches," in *Frequency Control Symposium, 2009 Joint with the 22nd European Frequency and Time forum. IEEE International*, 2009, pp. 1-4.

[14] P. Wei, Z. Hao, Y. Hongyu, L. Chuang-yuan, and K. Eun-Sok, "Electrical Frequency Tuning of Film Bulk Acoustic Resonator," *Microelectromechanical Systems, Journal of*, vol. 16, pp. 1303-1313, 2007.

[15] Z. Chengjie, N. Sinha, and G. Piazza, "Novel electrode configurations in dual-layer stacked and switchable ALN contour-mode resonators for low impedance filter termination and reduced insertion loss," in *Micro Electro Mechanical Systems (MEMS), 2010 IEEE 23rd International Conference on*, 2010, pp. 719-722.

[16] J. S. Pulskamp, D. C. Judy, R. G. Polcawich, R. Kaul, H. Chandrahalim, and S. A. Bhave, "Monolithically Integrated Piezomems SP2T Switch and Contour-Mode Filters," in *Micro Electro Mechanical Systems, 2009. MEMS 2009. IEEE 22nd International Conference on*, 2009, pp. 900-903.

[17] E. R. Crespin, R. H. Olsson, K. E. Wojciechowski, D. W. Branch, P. Clews, R. Hurley, *et al.*, "Fully integrated switchable filter banks," in *Microwave Symposium Digest (MTT), 2012 IEEE MTT-S International*, 2012, pp. 1-3.

[18] R. York, "Multifunctional adaptive microwave circuits and systems," M. S. a. W. D. Palmer, Ed., ed Raleigh, NC: Scitech, 2009, pp. 159-207.

[19] S. Gevorgian, A. Vorobiev, and T. Lewin, "dc field and temperature dependent acoustic resonances in parallel-plate capacitors based on SrTiO3 and Ba0.25Sr0.75TiO3 films: Experiment and modeling," *Journal of Applied Physics*, vol. 99, pp. -, 2006.

[20] D.-Y. Chen and J. D. Phillips, "Electric field dependence of piezoelectric coefficient in ferroelectric thin films," *Journal of electroceramics*, vol. 17, pp. 613-617, 2006.

[21] S. Gevorgian, *Ferroelectrics in microwave devices, circuits and systems: physics, modelling, fabrication and measurements*: Springer, 2009.

[22] H. Budzier and G. Gerlach, *Thermal infrared sensors: theory, optimisation and practice*: Wiley. com, 2010.

[23] N. Setter, D. Damjanovic, L. Eng, G. Fox, S. Gevorgian, S. Hong, *et al.*, "Ferroelectric thin films: Review of materials, properties, and applications," *Journal of Applied Physics*, vol. 100, pp. 051606-051606-46, 2006.

[24] N. Setter, *Electroceramic based mems: fabrication-technology and applications* vol. 9: Springer, 2005.

[25] Z. Xinen, J. D. Phillips, and A. Mortazawi, "A DC Voltage Dependant Switchable Thin Film Bulk Wave Acoustic Resonator Using Ferroelectric Thin Film," in *Microwave Symposium, 2007. IEEE/MTT-S International*, 2007, pp. 671-674.

[26] K.-y. Hashimoto, *RF bulk acoustic wave filters for communications*: Artech House, 2009.

[27] H. Campanella, *Acoustic wave and electromechanical resonators: concept to key applications*: Artech House, 2010.

[28] R. Ruby, "11E-2 Review and Comparison of Bulk Acoustic Wave FBAR, SMR Technology," in *Ultrasonics Symposium, 2007. IEEE*, 2007, pp. 1029-1040.

[29] S. A. Sis, V. Lee, J. D. Phillips, and A. Mortazawi, "A DC voltage dependent switchable acoustically coupled BAW filter based on BST-on-silicon composite

structure," in *Microwave Symposium Digest (MTT), 2012 IEEE MTT-S International*, 2012, pp. 1-3.

[30] I. B. Vendik, P. A. Turalchuk, O. G. Vendik, and J. Berge, "Modeling tunable bulk acoustic resonators based on induced piezoelectric effect in BaTiO3 and Ba0.25Sr0.75TiO3 films," *Journal of Applied Physics*, vol. 103, pp. -, 2008.

[31] A. Noeth, T. Yamada, A. K. Tagantsev, and N. Setter, "Electrical tuning of dc bias induced acoustic resonances in paraelectric thin films," *Journal of Applied Physics*, vol. 104, pp. -, 2008.

[32] P. A. Turalchuk and I. B. Vendik, "Modelling of tunable bulk acoustic resonators and filters with induced piezoelectric effect in BSTO film in a wide temperature range," in *EUROCON 2009, EUROCON '09. IEEE*, 2009, pp. 64-69.

[33] J. F. Rosenbaum, *Bulk acoustic wave theory and devices* vol. 147: Artech House Boston, 1988.

[34] B. Acikel, "High performance barium strontium titanate varactor technology for low cost circuit applications," University of California, 2002.

[35] J. Berge, M. Norling, A. Vorobiev, and S. Gevorgian, "Field and temperature dependent parameters of the dc field induced resonances in BaxSr1−xTiO3-based tunable thin film bulk acoustic resonators," *Journal of Applied Physics*, vol. 103, pp. -, 2008.

[36] A. B. Kozyrev, T. B. Samoilova, A. A. Golovkov, E. K. Hollmann, D. A. Kalinikos, V. E. Loginov, *et al.*, "Nonlinear behavior of thin film SrTiO3 capacitors at microwave frequencies," *Journal of Applied Physics*, vol. 84, pp. 3326-3332, 1998.

[37] R. Aigner, H. Ngoc-Hoa, M. Handtmann, and S. Marksteiner, "Behavior of BAW devices at high power levels," in *Microwave Symposium Digest, 2005 IEEE MTT-S International*, 2005, p. 4 pp.

[38] D. S. Shim and D. A. Feld, "A general nonlinear Mason model of arbitrary nonlinearities in a piezoelectric film," in *Ultrasonics Symposium (IUS), 2010 IEEE*, 2010, pp. 295-300.

[39] T. Ming Shiahu, S. C. Sun, and T.-Y. Tseng, "Effect of bottom electrode materials on the electrical and reliability characteristics of (Ba, Sr)TiO3 capacitors," *Electron Devices, IEEE Transactions on*, vol. 46, pp. 1829-1838, 1999.

[40] V. O. Sherman, P. Czarnecki, I. De Wolf, T. Yamada, N. Setter, B. Malic, *et al.*, "Reliability study of tunable ferroelectric capacitors," *Journal of Applied Physics*, vol. 104, pp. -, 2008.

[41] H. S. Newman, J. L. Ebel, D. Judy, and J. Maciel, "Lifetime Measurements on a High-Reliability RF-MEMS Contact Switch," *Microwave and Wireless Components Letters, IEEE*, vol. 18, pp. 100-102, 2008.

[42] D. M. Pozar, *Microwave engineering*: Wiley. com, 2009.

[43] M. Norling, J. Berge, and S. Gevorgian, "Parameter extraction for tunable TFBARs based on BaxSr1-xTiO3," in *Microwave Symposium Digest, 2009. MTT '09. IEEE MTT-S International*, 2009, pp. 101-104.

[44] V. Lee, L. Seungku, S. A. Sis, and A. Mortazawi, "Large signal performance of ferroelectric FBARs," in *Microwave Symposium Digest (MTT), 2012 IEEE MTT-S International*, 2012, pp. 1-3.

[45] S. Lee, V. Lee, S. A. Sis, and A. Mortazawi, "Large-Signal Performance and Modeling of Intrinsically Switchable Ferroelectric FBARs," *Microwave Theory and Techniques, IEEE Transactions on,* vol. 61, pp. 415-422, 2013.

[46] S. Lee, V. Lee, S. A. Sis, and A. Mortazawi, "A simple nonlinear mBVD model parameter extraction method for intrinsically switchable ferroelectric FBARs," in *Microwave Integrated Circuits Conference (EuMIC), 2013 European*, 2013, pp. 384-387.

[47] A. Mikhailov, A. Prudan, S. Ptashnik, T. Samoilova, and A. Kozyrev, "Switchable FBAR based on paraelectric films," in *Microwave Conference (EuMC), 2010 European*, 2010, pp. 791-794.

[48] S. Gevorgian and A. Vorobiev, "Impedance of DC-bias-controlled composite FBARs," *Ultrasonics, Ferroelectrics and Frequency Control, IEEE Transactions on,* vol. 60, pp. 795-804, 2013.

[49] V. Lee, S. A. Sis, Z. Xinen, and A. Mortazawi, "Intrinsically switchable interdigitated barium titanate thin film contour mode resonators," in *Microwave Symposium Digest (MTT), 2010 IEEE MTT-S International*, 2010, pp. 1448-1450.

[50] T. Ray, "Avago: RF Filter Biz to Benefit from Cheap Smartphone Growth, Says Morgan Stanley," ed. Barron's, 2013.

[51] K. M. Lakin, "Coupled resonator filters," in *Ultrasonics Symposium, 2002. Proceedings. 2002 IEEE*, 2002, pp. 901-908 vol.1.

[52] J. D. Larson, III, R. C. Bradley, S. Wartenberg, and R. C. Ruby, "Modified Butterworth-Van Dyke circuit for FBAR resonators and automated measurement system," in *Ultrasonics Symposium, 2000 IEEE*, 2000, pp. 863-868 vol.1.

[53] F. Jia-Shiang, X. A. Zhu, J. D. Phillips, and A. Mortazawi, "Improving Linearity of Ferroelectric-Based Microwave Tunable Circuits," *Microwave Theory and Techniques, IEEE Transactions on,* vol. 55, pp. 354-360, 2007.

[54] G. M. Rebeiz and J. B. Muldavin, "RF MEMS switches and switch circuits," *Microwave Magazine, IEEE,* vol. 2, pp. 59-71, 2001.

[55] "Agilent, Advanced Design System," ed.

[56] X. Zhu, J. D. Phillips, and A. Mortazawi, "A DC voltage dependant switchable thin film bulk wave acoustic resonator using ferroelectric thin film," *2007 Ieee/Mtt-S International Microwave Symposium Digest, Vols 1-6,* pp. 670-673, 2007.

[57] J. Berge, A. Vorobiev, W. Steichen, and S. Gevorgian, "Tunable Solidly Mounted Thin Film Bulk Acoustic Resonators Based on BaxSr1-xTiO3 Films," *Microwave and Wireless Components Letters, IEEE,* vol. 17, pp. 655-657, 2007.

[58] G. N. Saddik, D. S. Boesch, S. Stemmer, and R. A. York, "Strontium titanate DC electric field switchable and tunable bulk acoustic wave solidly mounted resonator," in *Microwave Symposium Digest, 2008 IEEE MTT-S International,* 2008, pp. 1263-1266.

[59] A. Volatier, E. Defay, M. Aid, A. Nhari, P. Ancey, and B. Dubus, "Switchable and tunable strontium titanate electrostrictive bulk acoustic wave resonator integrated with a Bragg mirror," *Applied Physics Letters,* vol. 92, pp. 032906-032906-3, 2008.

[60] Z. Xinen, V. Lee, J. Phillips, and A. Mortazawi, "An Intrinsically Switchable FBAR Filter Based on Barium Titanate Thin Films," *Microwave and Wireless Components Letters, IEEE,* vol. 19, pp. 359-361, 2009.

[61] G. N. Saddik and R. A. York, "An L-section DC electric field switchable bulk acoustic wave solidly mounted resonator filter based on Ba0.5Sr0.5TiO3," *Ultrasonics, Ferroelectrics and Frequency Control, IEEE Transactions on,* vol. 59, pp. 2036-2041, 2012.

[62] G. Piazza, P. J. Stephanou, and A. P. Pisano, "One and two port piezoelectric higher order contour-mode MEMS resonators for mechanical signal processing," *Solid-State Electronics,* vol. 51, pp. 1596-1608, 2007.

[63] G. Piazza, P. J. Stephanou, and A. P. Pisano, "Piezoelectric Aluminum Nitride Vibrating Contour-Mode MEMS Resonators," *Microelectromechanical Systems, Journal of,* vol. 15, pp. 1406-1418, 2006.

[64] Z. Chengjie, J. Van der Spiegel, and G. Piazza, "1.05-GHz CMOS oscillator based on lateral- field-excited piezoelectric AlN contour- mode MEMS resonators," *Ultrasonics, Ferroelectrics and Frequency Control, IEEE Transactions on,* vol. 57, pp. 82-87, 2010.

[65] Z. Chengjie, J. Van der Spiegel, and G. Piazza, "1.5-GHz CMOS voltage-controlled oscillator based on thickness-field-excited piezoelectric AlN contour-mode MEMS resonators," in *Custom Integrated Circuits Conference (CICC), 2010 IEEE,* 2010, pp. 1-4.

[66] P. J. Stephanou and A. P. Pisano, "PS-4 GHZ Contour Extensional Mode Aluminum Nitride MEMS Resonators," in *Ultrasonics Symposium, 2006. IEEE,* 2006, pp. 2401-2404.

[67] T. Hirano, H. Nakano, Y. Hirachi, J. Hirokawa, and M. Ando, "De-Embedding Method Using an Electromagnetic Simulator for Characterization of Transistors in the Millimeter-Wave Band," *Microwave Theory and Techniques, IEEE Transactions on,* vol. 58, pp. 2663-2672, 2010.

[68] Z. Xinen, C. Ding-Yuan, J. Zhang, J. D. Phillips, and A. Mortazawi, "Characterization of thin film BST tunable capacitors using a simple two port measurement technique," in *Microwave Symposium Digest, 2005 IEEE MTT-S International*, 2005, p. 4 pp.

[69] A. Noeth, T. Yamada, P. Muralt, A. K. Tagantsev, and N. Setter, "Tunable thin film bulk acoustic wave resonator based on BaxSr1-xTiO3 thin film," *Ultrasonics, Ferroelectrics and Frequency Control, IEEE Transactions on,* vol. 57, pp. 379-385, 2010.

[70] F. Z. Bi and B. P. Barber, "Bulk acoustic wave RF technology," *Microwave Magazine, IEEE,* vol. 9, pp. 65-80, 2008.

[71] P. J. Stephanou and A. P. Pisano, "GHZ higher order contour mode ALN annular resonators," in *Micro Electro Mechanical Systems, 2007. MEMS. IEEE 20th International Conference on*, 2007, pp. 787-790.

[72] F. Jia-Shiang, X. A. Zhu, C. Ding-Yuan, J. D. Phillips, and A. Mortazawi, "A Linearity Improvement Technique for Thin-film Barium Strontium Titanate Capacitors," in *Microwave Symposium Digest, 2006. IEEE MTT-S International*, 2006, pp. 560-563.

[73] Y. Yong-Kyu, K. Dongsu, M. G. Allen, J. S. Kenney, and A. T. Hunt, "A reduced intermodulation distortion tunable ferroelectric capacitor-architecture and demonstration," *Microwave Theory and Techniques, IEEE Transactions on,* vol. 51, pp. 2568-2576, 2003.

[74] R. A. York, "Circuit configuration for DC-biased capacitors," ed: Google Patents, 2004.
[75] R. Abdolvand, H. M. Lavasani, G. K. Ho, and F. Ayazi, "Thin-film piezoelectric-on-silicon resonators for high-frequency reference oscillator applications," *Ultrasonics, Ferroelectrics and Frequency Control, IEEE Transactions on*, vol. 55, pp. 2596-2606, 2008.
[76] S. Lee, V. Lee, S. A. Sis, and A. Mortazawi, "Linearity analysis of intrinsically switchable ferroelectric FBAR filters," in *Microwave Symposium Digest (IMS), 2013 IEEE MTT-S International*, 2013, pp. 1-3.
[77] P. Duval, *High vacuum production in the microelectronics industry* vol. 2: Elsevier, 1988.